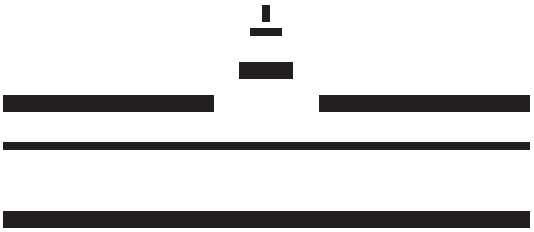

Westfälische Wilhelms-Universität Münster

Diplomarbeit in Mathematik

An adjoint FEM approach for the EEG forward problem

eingereicht von

Sven Wagner

Münster, 6. Oktober, 2011

Fachbereich 10
Mathematik und
Informatik

Gutachter:

Prof. Dr. Martin Burger

Institut für Numerische und Angewandte Mathematik

Priv.-Doz. Dr. Carsten Wolters

Institut für Biomagnetismus und Biosignalanalyse

Abstract

This thesis is concerned with an investigation of the adjoint approach for the EEG forward problem. It is deduced from the adjoint method and compared to the partial integration approach using transfer matrices for tetrahedral and hexahedral 4-layered spherical shell models. Furthermore a realistic hexahedral head model with anisotropic gray and white matter compartments is used to investigate the L_2 sensitivity distribution for a given lead positioned at the surface of the head model. This head model is used to investigate the effect on the L_2 sensitivity distribution and the orientation of the lead field if the CSF compartment within the volume conductor is neglected. The adjoint approach and the partial integration approach attain exactly the same results concerning required arithmetic operations, relative difference error and magnitude error and both approaches use a continuous source space. The adjoint approach can be further used to investigate the L_2 sensitivity for a given lead for dipoles in the source space.

Acknowledgments

I want to thank

- Carsten Wolters for introducing me into the field of bioelectromagnetism and the continuous discussions during the last two years.
- Martin Burger for giving me the chance to write this thesis in his lab and many fruitful discussions.
- Benjamin Lanfer for many helpful discussions and proofreading this thesis.
- Johannes Vorwerk for providing me many models and scirun nets.
- Felix Lucka for proofreading this thesis and for ideas presented in Chapter 6.
- Philipp Schmauck and Lars Ruthotto for making this thesis readable.
- My parents Peter and Karola for their financial and mental support.
- My girlfriend Nadine for the nice time beside writing this thesis.

Contents

Frequently used notations

$\Omega \subset \mathbb{R}^3$	Head domain
$\partial\Omega$	Boundary of head domain
$\sigma \in \mathbb{R}^{3\times 3}$	Conductivity tensor
$\mathbf{J}^p \in \mathbb{R}^3$	Primary current vector
$\mathbf{l_{ab}} \in \mathbb{R}^3$	Lead vector
$\mathbf{q} \in \mathbb{R}^3$	Dipole moment vector
$b_i,\ i = 1, \cdots, N$	Right hand side vector
E_{LE}	Reciprocal electrical field
J_{LE}	Reciprocal current density field
$K_{ij},\ i, j = 1, \cdots, N$	Stiffness matrix
$L \in \mathbb{R}^{(S-1)\times 3N}$	Lead field matrix
$L^p(\Omega)$	Space of p-integrable real-valued functions
N	Number of grid nodes
S	Number of scalp electrodes
$T \in \mathbb{R}^{(S-1)\times N}$	Transfer matrix
V	Electric potential
$V^{\infty,\mathbf{x}_0}(\mathbf{x})$	Singularity potential
$V^{corr,\mathbf{x}_0}(\mathbf{x})$	Correction potential
$W \in \mathbb{R}^{N\times(S-1)}$	Solution matrix of adjoint PDE
$W_p^k(\Omega)$	Sobolev space of real-valued functions

List of Figures

1 Introduction

Electroencephalography (EEG) is a non-invasive tool that can be used to reconstruct sources of cerebral activity generated in the human brain. The EEG is used in many different medical fields like clinical diagnosis ,e.g., Michel et al. [12] investigated the imaging of interictal epileptic activity using a 128-channel EEG recording device. Furthermore the EEG is used in the field of cognitive neuroscience, see ,e.g., the work of Baillet et al. [2].

The first human EEG was recorded in 1924 by Hans Berger, a german psychiatrist [4]. Berger studied medicine at the university of Jena, where he obtained his medical degree in 1897 [19]. Bergers work [4] was disbelieved until 1934, where Adrian and Matthews confirmed his results [1]. Detecting the generators of the recorded EEG signals located in the pyramidal cells of the human brain is called *EEG source analysis*. This localization task was the first time introduced by Brazier [6] in 1949. It requires to solve a *forward problem* and an *inverse problem*. For the forward problem the potential at the EEG scalp electrodes generated by an electrical source configuration has to be computed. This source configuration represents the active neurons in the human brain. For a measured EEG signal, the inverse problem consists of finding the corresponding electrical sources within the human brain.

Many inverse source localization algorithms use the lead field approach, which was the first time explained by Robert McFee and Franklin D. Johnston [28] in 1953. For this, the continuous current distribution within the human head is discretized into a finite number of possible dipolar sources. The partial differential equation for the EEG forward problem has to be solved three times per possible dipolar source. In the past, doing so using 3D discretization methods was considered a computationally expensive task, see Wolters et al. [52]. To circumvent this, the reciprocity principle is introduced. With it the partial differential equation for the EEG forward problem has not to be solved three times per possible dipolar source, but rather a number of times bounded by the number of EEG scalp electrodes minus one. The transfer matrix approach presented in Wolters et al. [51] and Weinstein et al. [49] is another approach

which considerably reduced the computation time. The mathematical law of associativity with respect to the matrix multiplication is used.

This thesis is concerned with an investigation of the adjoint approach presented in Vanrumste [45], Mohr [31] and Vallaghe [46], which uses both the lead field theory and the reciprocity principle. It is compared to the partial integration approach using transfer matrices presented in Lew et al. [27]. Vallaghe stated in [46] that both the adjoint approach and the transfer matrix approach change the forward problem from a dipolar source point of view to a sensor point of view. Furthermore Vallaghe stated that the difference between both approaches is that the adjoint approach uses the original continuous space whereas the transfer matrix approach uses a discretized one. Based on this statement, we compare both approaches theoretically and practically with regard to different error measures in different tetrahedral and hexahedral finite element models. Additionally, we want to calculate and compare the arithmetic operations needed to solve the EEG forward problem. The described difference with regard to continuous space and discretized space will be investigated in the summary and conclusion of this thesis.

This thesis is organized as follows:
In the first part we introduce to the field of bioelectromagnetism. Some physiological basics are given and then the partial differential equation for the EEG forward problem is derived. Furthermore, the lead field theory and the reciprocity theory are introduced. The reciprocity theorem is very important for the derivation of the adjoint approach. With it, the computation time to solve the EEG forward problem can be reduced considerably. In the next chapter, three different EEG forward approaches are presented. The adjoint approach is deduced from the adjoint method presented in Vallaghe et al. [46]. Furthermore, we describe how the adjoint method can be used to calculate the lead field matrix in a feasible calculation time. In Chapter 4 and 5 the implementation of both approaches and the calculation of the required arithmetic operations to solve the EEG forward problem are described. Furthermore, some numerical simulations for the adjoint approach and the partial integration approach are presented. The potential at a given sensor node for the adjoint approach is calculated analytically in Chapter 6. A realistic, geometry adapted hexahedral head model is presented in Chapter 7 to show the L_2 sensitivity distribution for a given EEG lead. This head model is further used to investigate if a head model without CSF compartment leads to the same L_2 sensitivity distribution within the human brain and if the orientation of the vector field differs in that case. A summary and a conclusion is presented in Chapter 8, where

the statement of Vallaghe [46] is discussed. In Chapter 9 a possible outlook is given, where some ideas are presented how the relative difference error and the magnitude error might be improved. Furthermore, we want to compare the orientation of the vector field ∇w if a head model with isotropic gray and white matter compartments is used instead of the same head model with anisotropic compartments. The thesis closes with some mathematical background in the Appendix A.1 and a derivation of the Sobolev space $W_p^k(\Omega)$ in the Appendix A.2.

2 Basic Information

In this chapter we present some neurological basics and explain how the EEG signals are generated. The so called *pyramidal cells* are introduced which are able to generate fields measurable by the EEG electrodes. Maxwell's equations and the quasi-static approximation of Maxwell's equations will be used to develop the *partial differential equation for the EEG forward problem*. We obtain the *lead field*, if the partial differential equation for the EEG forward problem is solved three times per possible dipolar source. The reciprocity principle invented by Helmholtz can be used to reduce the computational amount. Helmholtz' reciprocity theorem and a field theoretic formulation of Helmholtz' reciprocity theorem will be introduced. We will end this chapter with a comparison of the so called *reciprocal electric field* and the lead field generated due to a set of scalp electrodes. Furthermore we explain how the reciprocity principle can be used in the field of bioelectromagnetism.

In this chapter the books

- Simulation of Bioelectric Fields: The Forward and Inverse Problem of Electro-encephalographic Source Analysis by M. Mohr [31],
- Bioelectromagnetism - Principles and Applications of Bioelectric and Biomagnetic Fields by J. Malmivuo and R. Plonsey [29]

and the paper

- Review on solving the forward problem in EEG source analysis by H. Hallez et al. [21],

are used, where further information and figures can be found.

2.1 Physiological basics and the generators of the EEG signals

The main task of the EEG forward problem is to compute the potential at the scalp electrodes located at the surface of the human head. In the following part we explain which cells are able to generate fields measurable by the EEG scalp electrodes. We follow the work of Hallez et al. [21] and Mohr [31].
In the human brain are 10^{10} to 10^{11} *nerve cells* or *neurons* located. Most of them vary in size and shape, but all of them have the same anatomical structure, see Figure 2.1. A neuron can be divided, following the structure and functions, into three subparts, the *dendrites*, the cell body called *soma* and the *axon*. They handle signals generated in the human brain in the following way: Signals from other nerve cells in the brain are picked up from the dendrites and transfered to the soma, which combines them and generates if it is possible a new signal. If a new signal is generated, the axon sends it to other neurons or muscle cells.

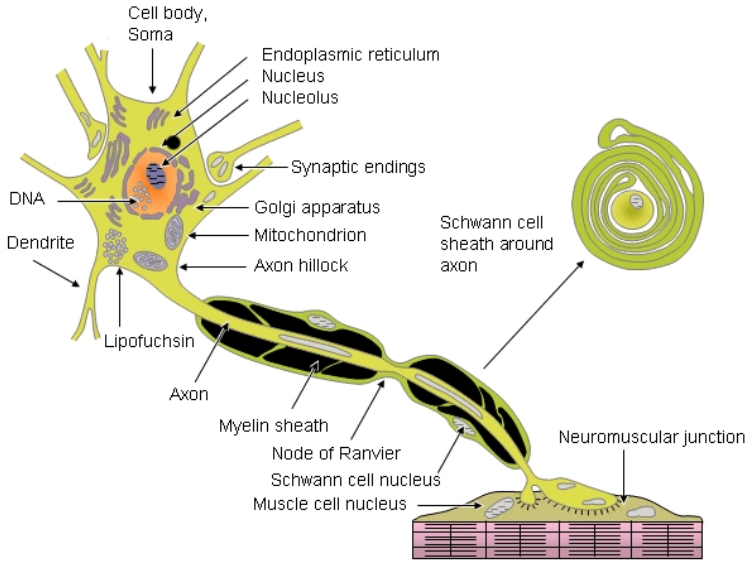

Figure 2.1: A Neuron see: [29], Figure 2.1.

When a neuron does not treat any signal, there is a potential difference between the intracellular and the extracellular domain of approximatively -60 mV, which is called *transmembrane potential*. The connection between the axon and the next cell is called the *synapse*. The synapse forwards informations, generated in the soma, to the next nerve cell. The part of the synapse on the side of

the axon is called *presynaptic terminal* and the part on the connected cell is called *postsynaptic terminal*. The signals can only cross the synapse in one direction, from the presynaptic to the postsynaptic part, due to the fact that the presynaptic cell creates a chemical transmitter. If this transmitter reaches the receptors of a postsynaptic neuron the permeability for charged ions changes. We distinguish between two sorts of chemical transmitter, the *inhibitory* and the *exhibitory* ones. On the one side, exhibitory neurotransmitters allow signals to increase. Thus, it causes an influx of positive ions. This leads to a depolarization, that is, the potential difference across the cell membrane decreases. On the other side, inhibitory neurotransmitters cause an outflow of positive ions. This leads to a hyperpolarization, that is, the potential difference across the cell membrane increases. When a certain amount of depolarization in the intracellular compartment is reached, an action potential is generated and forwarded via the axon to other neurons or nerve cells.

The action potential has a large amplitude of 70-110 mV. Due to the fact that the brain is separated from the EEG electrodes by the skull, which has a very low conductivity, a large number of neurons must be synchronously active to generate a field measurable by the EEG scalp electrodes. The action potential has only a very short time course of about 0.3 ms. It is therefore not normal that a large number of neighbouring neurons create an action potential at exactly the same time. Changes in the transmembrane potentials located in the postsynaptic parts of the neurons change the potential field measured by the EEG electrodes. This changes have a smaller amplitude of 0.1-10 mV but a time course of 10-20 ms, which is many times larger compared to the time course of the action potential.

It is not sufficient that the activity is only synchronous. The fields have to be similarly arranged so that different fields do not cancel each other. A class of neurons that being able to generate fields measurable by the EEG electrodes are the so called *pyramidal cells*. This is based on the fact that their dendrite trees are parallel to each other and orthogonal to the cortical surface, see Hallez et al. [21] for more details. Thus it is assumed that these pyramidal cells are the generators of the EEG signal.

2.2 EEG forward problem

This section will derive the partial differential equation for the EEG forward problem. It is based on Maxwell's equations which describe the connection between electric and magnetic fields. Due to the fact that we deal with frequencies that are below 100 Hz in bioelectromagnetism, the quasi-static approximation of Maxwell's equations can be applied in order to neglect the time dependency. This gives us the possibility to derive the potential equation for the EEG forward problem.

Another interesting question is the modelling of the primary current vector $\mathbf{J}^p$ in the potential equation. We introduce the so called *point sources* or *monopoles*, which are the simplest source models. Based on the fact that we have to preserve the current in the volume conductor, we are not able to use point sources to model the primary current vector $\mathbf{J}^p$. Thus another interesting source model is introduced, the so called *current dipole* model. It is given by two monopoles separated by a short distance h where the magnitudes of both monopoles have exactly the same value and the opposite sign. If the distance between both monopoles is decreased to zero, the *real mathematical* dipole model is received. The mathematical dipole is used in many applications to model the primary current vector $\mathbf{J}^p$, see [33],[34],[14] for further details.

Since the potential equation is an elliptic partial differential equation, a boundary condition at the surface of the volume conductor Ω is needed. Based on the fact that the air is a non conductive medium, a *homogeneous Neumann* boundary condition is considered. In this section the work of Mohr [31] and the work of Malmivuo and Plonsey [29] are used, where many further details could be found.

2.2.1 Maxwell's equations

Maxwell's equations are four coupled partial differential equations, which are a fundamental part of physics and electrical engineering. They were derived by James Clerk Maxwell during the years 1861 to 1864 [30].
In the next definition, Maxwell's equations are presented.

Definition 1 (Maxwell's equations [30])**.** *Let $\boldsymbol{E}$ be the electric field, $\boldsymbol{B}$ the magnetic field, ϵ_0 the electrical permittivity, μ the magnetic permeability, ρ the*

charge density and $\boldsymbol{J}$ *the current density. Then Maxwell's equations are given by*

$$\nabla \cdot \boldsymbol{E} = \frac{\rho}{\epsilon_0} \tag{2.1}$$

$$\nabla \times \boldsymbol{E} = -\frac{\partial \boldsymbol{B}}{\partial t} \tag{2.2}$$

$$\nabla \cdot \boldsymbol{B} = 0 \tag{2.3}$$

$$\nabla \times \boldsymbol{B} = \mu(\boldsymbol{J} + \epsilon_0 \frac{\partial \boldsymbol{E}}{\partial t}) \tag{2.4}$$

Maxwell's equations describe the relationship between electric and magnetic fields due to the effect of charge and current density. Additionally they describe how the magnetic field $\mathbf{B}$ and the electric field $\mathbf{E}$ change in time.

Brandt and Dahmen [7] explained that the *continuity equation* can be used in bioelectromagnetism

$$\nabla \cdot \mathbf{J} = -\frac{\partial \rho}{\partial t}. \tag{2.5}$$

It says that the divergence of the current density is given by the temporal change of the charge density.

The current density $\mathbf{J}$ can be divided in a passive non-magnetic medium into the Ohmic current and the polarization current [47]

$$\mathbf{J} = \sigma \mathbf{E} + \frac{\partial \mathbf{P}}{\partial t} \tag{2.6}$$

with σ being the conductivity and $\mathbf{P} = (\epsilon - \epsilon_0)\mathbf{E}$ being the polarization of the volume with the permittivity of the medium ϵ.

2.2.2 Potential equation

The quasi-static approximation presented in Faugeras et al. [17] holds for frequencies we are dealing with. This allows us to neglect the time derivative of the magnetic field $\mathbf{B}$ and the electric field $\mathbf{E}$ in Maxwell's equations. Temporal changes of both fields are nearly the same in the whole volume conductor. This means that we are able to investigate both fields for different time points completely independent.

Neglecting the time derivative in (2.2) leads to $\nabla \times \mathbf{E} = 0$, so that the electric field $\mathbf{E}$ can be expressed by a scalar potential V

$$\mathbf{E} = -\nabla V. \tag{2.7}$$

Due to the fact that we are able to neglect the time derivative of the electric field $\mathbf{E}$, the expression $\frac{\partial \mathbf{P}}{\partial t} = (\epsilon - \epsilon_0)\frac{\partial \mathbf{E}}{\partial t}$ is zero. This leads to

$$\mathbf{J} \overset{(2.6)}{=} \sigma \mathbf{E} \overset{(2.7)}{=} -\sigma \nabla V \tag{2.8}$$

Since the brain is an active medium, we add a primary current vector $\mathbf{J}^p$ for the active sources within the human brain

$$\mathbf{J} \overset{(2.8)}{=} \mathbf{J}^p - \sigma \nabla V. \tag{2.9}$$

Furthermore, we are able to neglect the time derivative in the continuity equation (2.5). This gives us the possibility to describe the potential equation for the EEG forward problem

$$0 \overset{(2.5)}{=} \nabla \cdot \mathbf{J} \overset{(2.9)}{=} \nabla \cdot \mathbf{J}^p - \nabla \cdot \sigma \nabla V. \tag{2.10}$$

Definition 2. *The potential equation for the EEG forward problem is given by*

$$\nabla \cdot \sigma \nabla V = \nabla \cdot \boldsymbol{J}^p. \tag{2.11}$$

The EEG forward problem describes the distribution of the electric potential V in the human head due to the primary current $\mathbf{J}^p$ caused by brain activity. The conductivity σ can be described for an arbitrary point within the volume conductor Ω by a 3×3 matrix. Based on the fact that the conductivity at an arbitrary point is exactly the same for currents flowing to or away from that point, the conductivity σ will be symmetric. This fact gives us the possibility to transform σ into the basis of eigenvectors, which leads to a matrix with eigenvalues on the diagonal axis. All diagonal entries are positive, since the conductivity into one direction is positive. It follows that the conductivity σ is positive definite.

Since the divergence of $\mathbf{J}^p$ is scalar we define according to Malmivuo and Plonsey [29]

$$I_F = -\nabla \cdot \mathbf{J}^p,$$

where I_F is the so called *flow current density*. Thus we are able to rewrite the potential equation (2.11) as

$$-\nabla \cdot \sigma \nabla V = I_F. \tag{2.12}$$

As described above, the conductivity σ is symmetric and positive definite. Thus equation (2.12) is an elliptic partial differential equation, see Braess [5] for further details on that topic. Additionally, it is easy to show that the potential equation (2.11) is also an elliptic partial differential equation that requires a boundary condition at the boundary $\partial\Omega$ of the domain Ω, see Section 2.2.5 for further details on that issue.

2.2.3 Mathematical monopole, dipole and dipole moment

In bioelectromagnetism, the easiest source configuration we are able to deal with are the so called *monopoles* or *point sources*. Due to the fact that we have to preserve the current in the volume conductor, we are not able to use single point sources to model the current density vector $\mathbf{J}^p$. Another interesting source configuration are the so called *dipoles*. We distinguish between two sorts of dipoles, the *current dipole* and the *mathematical dipole*.
For the definition of a current dipole, we need a current source and a corresponding current sink. Both should have the same magnitude I and have to be separated by a short and finite distance h. The current dipole is directed from the current sink to the current source.
A mathematical dipole, also called *real dipole*, can be obtained if we decrease the distance h between the current source and the current sink to zero. If we decrease the distance h to zero and let the magnitude I stay constant, the dipole moment hI goes to zero. To receive a constant dipole moment hI, the limit $I \to \infty$ has to be considered. This leads to the following setting

$$h \to 0 \quad \textit{and} \quad I \to \infty.$$

An important point to mention is that the *dipole moment* $q = hI$ has to be finite in the limit. Let $\mathbf{e}_d$ be the unit vector oriented from the current sink to the current source. The *dipole moment vector* $\mathbf{q}$ can then be defined by

$$\mathbf{q} := q\mathbf{e}_d = hI\mathbf{e}_d. \tag{2.13}$$

If the distance h in the current dipole case is sufficiently small, the field generated by a current dipole and the field generated by a mathematical dipole will be nearly the same and we are able to approximate a real dipole by means of a current dipole.

2.2.4 Characterization of current density function

The formerly discussed facts can be used to describe a feasible characterization of the right-hand side vector $\mathbf{J}^p$. As mentioned before, the primary currents occur due to movements of ions within the dendrites of the pyramidal cells in the active regions of the human brain. Following Wolters [52], stimulus-introduced activation of many excitatory synapses of a whole pattern of neurons leads to negative current monopoles under the brain surface and to positive monopoles quite closely underneath, see the work of Nunez [33] for more details. DeMunck stated in his work [14] that the mathematical dipole is usually accepted in the field of bioelectromagnetism.
Thus, the current density function $\mathbf{J}^p$ for a mathematical dipole at position $\mathbf{x}_0$ with moment $\mathbf{q}$ can be characterized by

$$\mathbf{J}^p = \mathbf{q}\delta(\mathbf{x} - \mathbf{x}_0),$$

where δ is the so called *Dirac delta distribution* defined in Chapter 4.
This notation can be used to rewrite the right-hand side of equation (2.11)

$$\nabla \cdot \mathbf{J}^p = \nabla \cdot (\mathbf{q}\delta(\mathbf{x} - \mathbf{x}_0)). \tag{2.14}$$

This expression is very helpful in many cases. For example, it is used to derive the partial integration approach presented in Section 3.2.

2.2.5 Boundary condition and EEG forward equation

To obtain a complete model for the EEG forward problem, a boundary condition on the surface $\partial\Omega$ of the volume conductor Ω is needed. This is based on the fact that the potential equation for the EEG forward problem is an elliptic partial differential equation, see Section 2.2.3 for details.
In bioelectromagnetism we deal with head models which consists of different compartments, for example, the scalp, the skull, the CSF and the brain tissue with different conductivity values. Thus, the conductivity σ could have jumps at interfaces between two compartments. Let us assume that the conductivity is constant and isotropic within each compartment. Consequently the potential V is not differentiable between two compartments with different conductivity values. But the following continuity condition is fulfilled

$$\lim_{\Omega_l \ni \mathbf{p} \to \mathbf{p}^*} V_l(\mathbf{p}) = \lim_{\Omega_k \ni \mathbf{p} \to \mathbf{p}^*} V_k(\mathbf{p}), \tag{2.15}$$

where Ω_l is the l-th compartment of Ω and $\mathbf{p}^*$ an arbitrary point on the interface between the l-th and k-th compartment. This is a physical requirement, since

the potential V is continuous in the volume conductor and the values at an arbitrary interface between two compartments of both sides have to be equal. Another important fact is that the flow of currents $\sigma \nabla V$ is continuous in the volume conductor and along the interfaces, lying in it. This can be represented by the following formula

$$\lim_{\Omega_l \ni \mathbf{p} \to \mathbf{p}^*} < \sigma_l(\mathbf{p}) \nabla V_l(\mathbf{p}), \mathbf{n} > = \lim_{\Omega_k \ni \mathbf{p} \to \mathbf{p}^*} < \sigma_k(\mathbf{p}) \nabla V_k(\mathbf{p}), \mathbf{n} > . \tag{2.16}$$

We are now able to introduce the boundary condition to complete the model for the EEG forward problem. If the interface is the surface of the volume conductor Ω, equation (2.16) leads to

$$\lim_{\Omega \ni \mathbf{p} \to \mathbf{p}^*} < \sigma(\mathbf{p}) \nabla V(\mathbf{p}), \mathbf{n} > = 0. \tag{2.17}$$

This is due to the fact that the air surrounding the human head is non conductive which leads to a zero conductivity σ on the right-hand side. Since the term $\sigma \nabla V$ describes a flow of currents, equation (2.17) explains in the physical sense that no current can flow out of the head into the air and vice versa.
Boundary conditions like (2.17) are called *homogeneous Neumann boundary conditions*.
With the potential equation (Definition 2) and the boundary condition (2.17) we are now able to introduce the EEG forward problem.

Definition 3 (Partial differential equation for the EEG forward problem)**.** *The EEG forward problem is defined by the following partial differential equation*

$$\nabla \cdot \sigma \nabla V = \nabla \cdot \boldsymbol{J}^p \qquad \text{in } \Omega \tag{2.18}$$

$$< \sigma \nabla V, \boldsymbol{n} > = 0 \qquad \text{on } \partial\Omega \tag{2.19}$$

The EEG forward problem does not have a solution in the classical sense, due to the fact that a classical solution V of equation (2.18)-(2.19) has to be in the space $\mathcal{C}^2(\Omega) \cap \mathcal{C}^0(\overline{\Omega})$. Since we use multi-layered volume conductors with different conductivities, the conductivity σ is discontinuous at the interface between different compartments. In order to obtain a classical solution V of the EEG forward problem, the expression $\sigma \nabla V$ has to be continuous through the different compartments of the volume conductor Ω. It is therefore necessary that ∇V has also jumps at the interface between different compartments, which exactly cancel out the jumps of σ. The gradient of V is not defined in the sense of classical calculus along such interfaces, see Mohr [31]. If we use a volume

conductor Ω with Lipschitz continuous boundary and interfaces and assume that $\nabla \cdot \mathbf{J}^p \in L^2(\Omega)$ the potential V will be in the Sobolev space $W^1(\Omega)$. A definition of $L^2(\Omega)$ and $W^1(\Omega)$ can be found in Appendix A.2. Since we use dipolar sources to model the current density $\mathbf{J}^p$, the condition $\nabla \cdot \mathbf{J}^p \in L^2(\Omega)$ does not hold. In this thesis, we discuss those singularities and present different forward approaches.

2.3 Lead vector and lead field

A very important point for many inverse source localization algorithms is the lead field theory. If the so called *lead field matrix* is once calculated, the inverse problem can be reformulated as a finite dimensional linear problem. In this section we follow the basic ideas presented in Mohr [31] and Malmivuo and Plonsey [29].
In the first subsection we introduce the concept of a *lead vector*. It describes how the three dipoles with unit strength in the three Cartesian directions at a fixed location within a volume conductor influence the potential within or at the surface for a given pair of EEG electrodes. This concept can be expanded further. If we calculate the lead vector for each possible dipolar source location within the volume conductor, a vector field is generated, the so called *lead field*. Calculating the lead field for each sensor node pair results in the so called *lead field matrix*. The lead field matrix for different synchronously activated dipoles and a set of S scalp electrodes will be derived at the end of this section.

2.3.1 Lead vector

Let $\mathbf{i}_x$, $\mathbf{i}_y$ and $\mathbf{i}_z$ be three dipoles with unit strength at position $\mathbf{x}_0$ oriented parallel to the x-,y- and z-axis, respectively. In the first part of this section we investigate the potential field U at a certain position $\mathbf{p}$ generated by the dipole $\mathbf{i}_x$ with unit strength oriented parallel to the x-axis. Note that this potential must be evaluated with respect to another point or a reference point. A zero potential reference point is used in the following.
Let c_x be the corresponding potential U at position $\mathbf{p}$ caused by the dipole $\mathbf{i}_x$ and let $\mathbf{d}_x$ be the dipole $\mathbf{i}_x$ scaled with an arbitrary strength r_x, that is, $\mathbf{d}_x = \mathbf{i}_x r_x$. The potential U at position $\mathbf{p}$ caused by the dipole $\mathbf{d}_x$ can be calculated using the so called *linearity assumption* presented in Malmivuo and

Plonsey [29]

$$U_{\mathbf{p}}(\mathbf{d}_x) = c_x r_x.$$

Analogous formulations hold for the dipoles $\mathbf{d}_y$ and $\mathbf{d}_z$ scaled with strength r_y and r_z, oriented parallel to the y- and z-axis. Due to the assumed linearity assumption, the principle of *superposition* can be applied. Each dipole $\mathbf{d}$ at position $\mathbf{x}_0$ with arbitrary strength or orientation can thus be decomposed into the three orthogonal components $\mathbf{d}_x$, $\mathbf{d}_y$ and $\mathbf{d}_z$ and the potential U at position $\mathbf{p}$ caused by the dipole $\mathbf{d}$ can be calculated via

$$U_{\mathbf{p}}(\mathbf{d}) = c_x r_x + c_y r_y + c_z r_z,$$

where the terms c_x,c_y and c_z are the potentials U at position $\mathbf{p}$ caused by the three unit dipoles $\mathbf{i}_x$, $\mathbf{i}_y$ and $\mathbf{i}_z$, respectively.
If we denote $\mathbf{c} := (c_x, c_y, c_z)^T$ and $\mathbf{r} := (r_x, r_y, r_z)^T$ we can use them to calculate the potential U at position $\mathbf{p}$

$$U_{\mathbf{p}}(\mathbf{d}) = < \mathbf{c}, \mathbf{r} > .$$

The expression $\mathbf{r}$ is called the **dipole orientation vector** [31], which can be used to calculate the dipole moment $\mathbf{q}$ via $\mathbf{q} = ||\mathbf{r}||_2$.

In the next part of this section two points $\mathbf{a}$ and $\mathbf{b}$ within or at the surface of a volume conductor are assumed. For both points $\mathbf{a}$ and $\mathbf{b}$ we are able to calculate the vectors $\mathbf{c}_a$ and $\mathbf{c}_b$ caused by the three dipoles $\mathbf{i}_x$, $\mathbf{i}_y$ and $\mathbf{i}_z$ located at $\mathbf{x}_0$. Following the procedure above, we receive for a dipole $\mathbf{d}$ with arbitrary strength located at position $\mathbf{x}_0$

$$U_{\mathbf{a}}(\mathbf{d}) = < \mathbf{c}_a, \mathbf{r} > \quad U_{\mathbf{b}}(\mathbf{d}) = < \mathbf{c}_b, \mathbf{r} > .$$

The potential difference $U_{\mathbf{ab}}(\mathbf{d})$ between $\mathbf{a}$ and $\mathbf{b}$ can be obtained by

$$U_{\mathbf{ab}}(\mathbf{d}) := U_{\mathbf{a}}(\mathbf{d}) - U_{\mathbf{b}}(\mathbf{d}). \tag{2.20}$$

If we denote

$$\mathbf{I}_{\mathbf{ab}} := \mathbf{c}_{\mathbf{a}} - \mathbf{c}_{\mathbf{b}}, \tag{2.21}$$

$\mathbf{I}_{\mathbf{ab}}$ describes the potential difference of U between $\mathbf{a}$ and $\mathbf{b}$ caused by the three dipoles $\mathbf{i}_x$, $\mathbf{i}_y$ and $\mathbf{i}_z$, respectively.
We finally receive

$$U_{\mathbf{ab}}(\mathbf{d}) \overset{(2.20)}{=} U_{\mathbf{a}}(\mathbf{d}) - U_{\mathbf{b}}(\mathbf{d}) = < \mathbf{c}_a, \mathbf{r} > - < \mathbf{c}_b, \mathbf{r} > \overset{(2.21)}{=} < \mathbf{I}_{\mathbf{ab}}, \mathbf{r} > \tag{2.22}$$

A pair of surface electrodes is called a *lead* and the vector $\mathbf{I_{ab}}$ is called a *lead vector* for the lead positioned at **a** and **b**. The name originates from the fact that the lead vector can be used to calculate the potential difference between the lead for each dipole **d** with arbitrary strength or orientation located at position $\mathbf{x}_0$.

Burger and van Milan introduced the concept of a lead vector in 1946 in [9]. Malmivuo and Plonsey explained in [29] that the lead vector concept was for the first time employed in *electrocardiographic* (ECG) source analysis. They deeply described the Einthoven, Frank and Burger triangles in their work.

2.3.2 Lead field and lead field matrix

In this section we introduce the lead field and the lead field matrix. As described above, the potential difference between two points **a** and **b** depends on the location $\mathbf{x}_0$ where the dipole **d** is located. If the dipole position is changed, the lead vector $\mathbf{I_{ab}}$ will also change. But if the orientation or strength of the dipole is changed, the lead vector will not change. A change in the orientation or strength of the dipole will only cause a change of the dipole orientation vector **r** in equation (2.22), which is a very powerful property. Based on that fact, we calculate the corresponding lead vector $\mathbf{I_{ab}}(\mathbf{x}_0)$ for each possible point $\mathbf{x}_0$ within the volume conductor by evaluating the potential difference between **a** and **b** for the three dipoles $\mathbf{i}_x, \mathbf{i}_y$ and $\mathbf{i}_z$ positioned at $\mathbf{x}_0$. This creates a vector field, which is called *lead field*. The lead field theory was first explained by Robert McFee and Franklin D. Johnston in 1953 [28].

In Figure 2.2, a lead field is shown. We fixed two electrodes A and B forming a lead and investigate the variation of the lead vector $\mathbf{I_{AB}}$ at different source locations within the volume conductor. The resulting field of lead vectors is the lead field. This concept can be used to investigate the L_2 *sensitivity distribution for a given lead* presented in Chapter 7. The arrows are oriented from the EEG scalp electrode at position A to the reference electrode at position B.

In the next part the case where we have a set of S scalp electrodes will be explained. Fixing one electrode as reference, we are able to choose (S-1) leads and calculate for a dipole **d** with arbitrary strength or orientation positioned at $\mathbf{x}_0$ within Ω and for each lead the corresponding lead vector $\mathbf{I}_i(\mathbf{x}_0)$, $i =$

$1, \cdots, S-1$ by evaluating the potential difference between the lead for the three dipoles $\mathbf{i}_x, \mathbf{i}_y$ and $\mathbf{i}_z$ positioned at $\mathbf{x}_0$. The dipole orientation vector $\mathbf{r}$ can be calculated using the linearity assumption. Let us denote the vector of potential differences between the leads by $\mathbf{U}(\mathbf{d})$. This leads to

$$\mathbf{U}(\mathbf{d}) = \begin{pmatrix} < \mathbf{I}_1(\mathbf{x}_0), \mathbf{r} > \\ \vdots \\ < \mathbf{I}_{S-1}(\mathbf{x}_0), \mathbf{r} > \end{pmatrix} = L(\mathbf{x}_0)\mathbf{r}. \tag{2.23}$$

The matrix $L(\mathbf{x}_0) \in \mathbb{R}^{(S-1)\times 3}$ is called the *lead field matrix*.

This concept can be extended further. Mohr presented in [31] the lead field matrix for different dipoles that are simultaneously active. For m simultaneously activated dipoles at position $\mathbf{x}_1, \cdots, \mathbf{x}_m$ and S different scalp electrodes, this leads to a lead field matrix

$$L(\mathbf{x}_1, \cdots, \mathbf{x}_m) \in \mathbb{R}^{(S-1)\times 3m}.$$

The potential difference between the lead depends on the angle between the lead vector $\mathbf{I_{ab}}$ and the dipole orientation vector $\mathbf{r}$. If $\mathbf{I_{ab}}$ and $\mathbf{r}$ are oriented parallel to each other, the potential difference between the lead will be high. But if the lead vector and the dipole orientation vector are nearly orthogonal, the potential difference will be small.

2.4 Helmholtz reciprocity

In the second section of this chapter, we discussed the EEG forward problem. The lead field theory, presented in Section 2.3, is used by many methods that solve the inverse problem. Those methods discretize the lead field by many dipoles with unitary moments. For each dipole and orientation we have to solve the partial differential equation (2.18)-(2.19). Since this is a very time consuming part, we introduce the reciprocity principle. Instead of solving the EEG forward problem three times per dipolar source, the lead field matrix is calculated from a sensor point of view. This will reduce the computation time considerably since we have to solve the forward problem only $S-1$ times with S the number of sensors. We follow the work of Mohr [31] and the work of Malmivuo and Plonsey [29] in this section, where further details could be found.

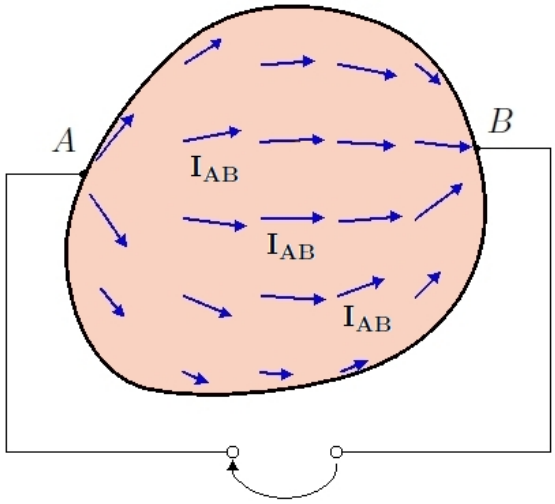

Figure 2.2: Lead field, see: [29], Figure 11.19.

The reciprocity principle was introduced into the area of biophysical research by Hermann von Helmholtz [24] in 1853. Over 100 years later, in 1969, Rush and Driscoll [38] applied the reciprocity principle to EEG source simulation.

The transfer matrix approach, described in Wolters et al. [51] and Weinstein et al. [49], is another approach which transfers the calculation of the lead field matrix from a source point of view to a sensor point of view. The transfer matrix approach will be introduced in Section 4.2.

2.4.1 The basic idea of reciprocity

According to Malmivuo and Plonsey [29] Helmholtz presented the following example in [24]. It distinguishes between two cases:

- A galvanometer G is connected at the surface of a volume conductor Ω. A double layer source element with voltage V_d is placed within the volume conductor. This double layer source element causes a current I_L in the galvanometer circuit.
- The galvanometer is replaced by an electromotive force with the same

magnitude V_d as the source element in the former case, which will be removed in this case. This setting produce a reciprocal current i_r at the position where the double layer source element was placed in the first case.

Both cases can be seen in Figure 2.3.

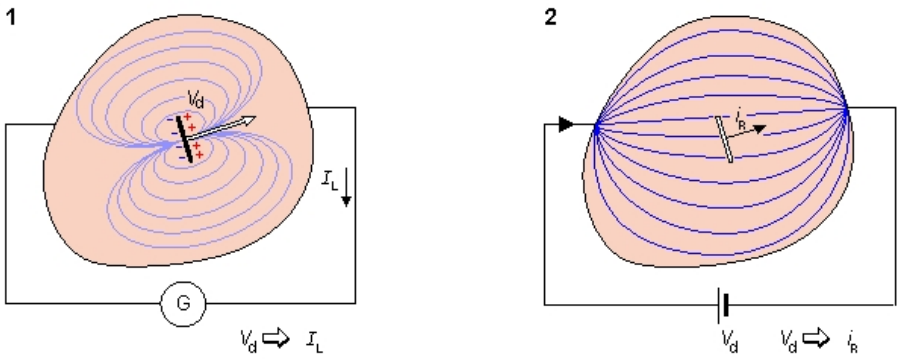

Figure 2.3: Volume conductor for reciprocity principle, see: [29], Figure 11.20.

Helmholtz' reciprocity principle leads to

$$\frac{I_L}{V_d} = \frac{i_r}{V_d}.$$

This means that the current I_L in the first case measured in the galvanometer circuit is equal to the current i_r which can be measured at the position of the removed double layer source element.
In this example a double layer source element was used to measure the corresponding current. In our case, current dipoles are used which create signals in voltage.

Malmivuo and Plonsey [29] demonstrated that the reciprocity principle does not depend on the location where the double layer source element is positioned. They increased the area of the double layer source element in the first case by a factor of f. Due to the linearity assumption this leads to an increasement of the current I_L measured in the galvanometer circuit by a factor of f. Due to the fact that the voltage over the double layer source element stays equal in the first case, the electromotive force V_d in the second case remains the same and it produces the same amount of current density. This causes an increasement of the reciprocal current i_r by a factor of f since the area of the double layer

element is now f times larger. This finally leads to

$$\frac{fI_L}{V_d} = \frac{fi_r}{V_d},$$

which can be divided by the factor f to receive the above form.

2.4.2 Mathematical theory

In this section, the reciprocity theorem introduced by Helmholtz is presented. As a further point, a field theoretic formulation of the reciprocity theorem is presented.

Theorem 1 (Helmholtz' reciprocity theorem, see: [31], page 20, Theorem 1)**.** *Let us consider the following two settings:*
First we assume that in a volume conductor a source I consisting of a point source and a point sink located at positions $\boldsymbol{p}_{source}$ and $\boldsymbol{p}_{sink}$ is present

$$I = I_*\delta(\boldsymbol{p}_{source} - r) - I_*\delta(\boldsymbol{p}_{sink} - r). \tag{2.24}$$

In the next setting, we assume that the scalar current density K on the surface of the volume conductor consists of a point source and a point sink located at $\boldsymbol{p}_{in}$ and $\boldsymbol{p}_{out}$

$$K = K_*\delta(\boldsymbol{p}_{in} - r) - K_*\delta(\boldsymbol{p}_{out} - r). \tag{2.25}$$

Then the relationship between both settings is given by

$$I_*[V_2(\boldsymbol{p}_{source}) - V_2(\boldsymbol{p}_{sink})] = K_*[V_1(\boldsymbol{p}_{in}) - V_1(\boldsymbol{p}_{out})], \tag{2.26}$$

where V_1 is given by the potential field generated by a source I and V_2 is given by the potential field generated by K.

Equation (2.26) states that the ratio between the potential difference between two points $\mathbf{p}_{source}$ and $\mathbf{p}_{sink}$ caused by a current K_* between points $\mathbf{p}_{in}$ and $\mathbf{p}_{out}$ and the potential difference between two surface points $\mathbf{p}_{in}$ and $\mathbf{p}_{out}$ generated by a current I_* flowing from $\mathbf{p}_{source}$ to $\mathbf{p}_{sink}$ is exactly given by the ratio $\frac{K_*}{I_*}$ between the currents.

A field theoretic formulation of Helmholtz' reciprocity theorem was first published by Rush and Driscoll [38]. It is presented in the following

Theorem 2 (Field theoretic formulation, see: [31], page 21, Theorem 2)**.** *Let Ω be a volume conductor consisting of $k = 1, \cdots, n$ compartments Ω_k in which the conductivity tensor σ is continuously differentiable and may be anisotropic. Let I_1 and I_2 be two different volume current sources, $\boldsymbol{K}_1$ and $\boldsymbol{K}_2$ be two current densities on the surface $\partial\Omega$ and let V_1 and V_2 be the potential fields resulting from I_1,$\boldsymbol{K}_1$ and I_2,$\boldsymbol{K}_2$.*
We now assume, that the interfaces separating the compartments and the boundary $\partial\Omega$ of the domain Ω are sufficient smooth. Furthermore, we assume

$$V_1, V_2 \in C^1(\overline{\Omega_k}), \quad (\sigma\nabla V_1), (\sigma\nabla V_2) \in C^1(\overline{\Omega_k}), \tag{2.27}$$

then it holds that

$$\int_\Omega V_1 I_2 \, dx - \int_\Omega V_2 I_1 \, dx = \int_{\partial\Omega} V_1 < \boldsymbol{K}_2, \boldsymbol{n} > \, ds - \int_{\partial\Omega} V_2 < \boldsymbol{K}_1, \boldsymbol{n} > \, ds \tag{2.28}$$

with $\boldsymbol{n}$ the outward normal vector to $\partial\Omega$.

Proof. We will only show a proof for a single compartment Ω_k. Due to (2.27) the functions V_i and $(\sigma\nabla V_i)$ are sufficient smooth and therefore, we are able to write

$$\begin{aligned}
\nabla \cdot V_1(\sigma\nabla V_2) &= V_1\nabla \cdot (\sigma\nabla V_2) + \nabla V_1(\sigma\nabla V_2) \\
\nabla \cdot V_2(\sigma\nabla V_1) &= V_2\nabla \cdot (\sigma\nabla V_1) + \nabla V_2(\sigma\nabla V_1)
\end{aligned}$$

Subtracting the second term from the first term yields

$$\begin{aligned}
\nabla \cdot V_1(\sigma\nabla V_2) - \nabla \cdot V_2(\sigma\nabla V_1) = {} & V_1\nabla \cdot (\sigma\nabla V_2) + \nabla V_1(\sigma\nabla V_2) \\
& - V_2\nabla \cdot (\sigma\nabla V_1) - \nabla V_2(\sigma\nabla V_1)
\end{aligned}$$

Since the conductivity σ is symmetric, we are able to write

$$\begin{aligned}
\nabla V_1(\sigma\nabla V_2) &= \sigma^T \nabla V_1 \nabla V_2 \\
&= \sigma\nabla V_1 \nabla V_2 \\
&= \nabla V_2(\sigma\nabla V_1)
\end{aligned}$$

Thus, the above equation reduces to

$$\nabla \cdot V_1(\sigma\nabla V_2) - \nabla \cdot V_2(\sigma\nabla V_1) = V_1\nabla \cdot (\sigma\nabla V_2) - V_2\nabla \cdot (\sigma\nabla V_1)$$

The following condition is fulfilled

$$\nabla \cdot V_1(\sigma\nabla V_2) - \nabla \cdot V_2(\sigma\nabla V_1) = \nabla \cdot (\sigma\nabla V_2)V_1 - \nabla \cdot (\sigma\nabla V_1)V_2$$

Rewriting the above term and integrating over the compartment Ω_k yields

$$\int_{\Omega_k} \nabla \cdot (\sigma \nabla V_2) V_1 \, dx - \int_{\Omega_k} \nabla \cdot (\sigma \nabla V_1) V_2 \, dx = \int_{\Omega_k} [V_1 \nabla \cdot (\sigma \nabla V_2) - V_2 \nabla \cdot (\sigma \nabla V_1)] \, dx$$

Both terms on the left-hand side can be circumscribed using the divergence theorem

$$\int_{\Omega_k} \nabla \cdot (\sigma \nabla V_2) V_1 \, dx = \int_{\partial\Omega_k} < V_1 (\sigma \nabla V_2), \mathbf{n} > \, ds - \int_{\Omega_k} (\nabla V_1)(\sigma \nabla V_2) \, dx$$
$$\int_{\Omega_k} \nabla \cdot (\sigma \nabla V_1) V_2 \, dx = \int_{\partial\Omega_k} < V_2 (\sigma \nabla V_1), \mathbf{n} > \, ds - \int_{\Omega_k} (\nabla V_2)(\sigma \nabla V_1) \, dx$$

Following the notations above, we have

$$\int_{\Omega_k} (\nabla V_1)(\sigma \nabla V_2) \, dx = \int_{\Omega_k} (\nabla V_2)(\sigma \nabla V_1) \, dx$$

Thus, we finally receive

$$\int_{\partial\Omega_k} < V_1 (\sigma \nabla V_2), \mathbf{n} > ds - \int_{\partial\Omega_k} < V_2 (\sigma \nabla V_1), \mathbf{n} > ds = \int_{\Omega_k} [V_1 \nabla \cdot (\sigma \nabla V_2) - V_2 \nabla \cdot (\sigma \nabla V_1)] dx$$

Rearranging this equation and summing up over all compartments leads to

$$\int_{\Omega} V_1 \nabla \cdot (\sigma \nabla V_2) - V_2 \nabla \cdot (\sigma \nabla V_1) dx = \sum_{k=1}^{n} \int_{\partial\Omega_k} < V_1 (\sigma \nabla V_2) - V_2 (\sigma \nabla V_1), \mathbf{n} > \, ds \tag{2.29}$$

We now define $\Omega_{jk} = \Omega_j \cap \Omega_k$ as the shared interface of the compartments Ω_j and Ω_k. Equation (2.29) contains Ω_{jk} two times. The first time in the surface integral over Ω_j and the second time in the surface integral over Ω_k. But the outward normal vectors at both surfaces have the opposite sign, that is, $\mathbf{n}_j = -\mathbf{n}_k$. Therefore, the sum of both integrals is zero and equation (2.29) reduces to

$$\int_{\Omega} [V_1 \nabla \cdot (\sigma \nabla V_2) - V_2 \nabla \cdot (\sigma \nabla V_1)] dx = \int_{\partial\Omega} < V_1 (\sigma \nabla V_2) - V_2 (\sigma \nabla V_1), \mathbf{n} > \, ds \tag{2.30}$$

We have $\nabla \cdot (\sigma \nabla V_i) =$ -I_i and $(\sigma \nabla V_i) = -\mathbf{K}_i$ and the theorem is established. □

Equation (2.30) is a well-known formula in the area of physical sciences. It is a version of Green's second formula. For more information about Green's formula see O. Forster [18].

2.4.3 Reciprocal lead field computation

The reciprocity theorem gives us the possibility to calculate the lead field in an alternative way. In the following part we describe how this can be done.
A volume conductor with a fixed lead is investigated. A reciprocal unit current is introduced at electrode position $\mathbf{p}_{in}$ and removed at electrode position $\mathbf{p}_{out}$. This introduced current creates a potential field V_{LE} within the volume conductor. This potential field is called the *reciprocal potential field*, see the right volume conductor in Figure 2.3.
The *reciprocal electrical field* E_{LE} is given by

$$E_{LE} = -\nabla V_{LE}$$

and the corresponding *reciprocal current density field* is given by

$$J_{LE} = \sigma E_{LE} = -\sigma \nabla V_{LE}.$$

Let us furthermore consider a current dipole given by a current source located at $\mathbf{p}_{source}$ and a current sink located at $\mathbf{p}_{sink}$ with exactly the same magnitude and the opposite sign, see Section 2.2.3 for further details. For a current I_* flowing between $\mathbf{p}_{source}$ and $\mathbf{p}_{sink}$, the dipole orientation vector $\mathbf{r}$ can be defined by

$$\mathbf{r} = I_*(\mathbf{p}_{source} - \mathbf{p}_{sink}). \tag{2.31}$$

Based on the fact that the reciprocal potential field V_{LE} is created by currents introduced at the surface of a volume conductor, which is assumed to be source-free in the interior, we are able to calculate a *Taylor series expansion* of V_{LE}

$$V_{LE}(\mathbf{p}_{source}) = V_{LE}(\mathbf{p}_{sink}) + < \nabla V_{LE}(\mathbf{p}_{source}), (\mathbf{p}_{source} - \mathbf{p}_{sink}) > + \cdots \tag{2.32}$$

Note that we are not able to calculate such an expansion between conductivity jumps.
We now decrease the distance between $\mathbf{p}_{sink}$ and $\mathbf{p}_{source}$ and keep the dipole orientation vector $\mathbf{r}$ constant by increasing the current I_* between $\mathbf{p}_{source}$ and $\mathbf{p}_{sink}$. If the distance between $\mathbf{p}_{sink}$ and $\mathbf{p}_{source}$ is sufficiently small, the second order terms and the higher terms in equation (2.32) can be neglected. This leads to

$$\begin{aligned} I_*(V_{LE}(\mathbf{p}_{source}) - V_{LE}(\mathbf{p}_{sink})) &\overset{(2.32)}{=} I_*(< \nabla V_{LE}(\mathbf{p}_{source}), (\mathbf{p}_{source} - \mathbf{p}_{sink}) >) \\ &\overset{(2.31)}{=} < \nabla V_{LE}(\mathbf{p}_{source}), \mathbf{r} > . \end{aligned}$$

Let us denote the potential field generated by a dipolar source within the volume conductor with V_{dip}. In addition, we denote the potential difference caused by

the dipolar source between two electrodes $\mathbf{p}_{in}$ and $\mathbf{p}_{out}$ located at the surface of the volume conductor by

$$U_{LE} := V_{dip}(\mathbf{p}_{out}) - V_{dip}(\mathbf{p}_{in}). \tag{2.33}$$

Using Theorem 1 with $K_* = 1$, $V_{LE} = V_2$, $V_{dip} = V_1$ yields

$$\begin{aligned} U_{LE} &\overset{(2.33)}{=} V_{dip}(\mathbf{p}_{out}) - V_{dip}(\mathbf{p}_{in}) \\ &= -(V_{dip}(\mathbf{p}_{in}) - V_{dip}(\mathbf{p}_{out})) \\ &\overset{Theorem\ 1}{=} -I_*(V_{LE}(\mathbf{p}_{source}) - V_{LE}(\mathbf{p}_{sink})) \\ &\overset{Taylor}{=} < -\nabla V_{LE}(\mathbf{p}_{source}), \mathbf{r} > \end{aligned}$$

Comparing this result with the lead field computation (2.22) yields

$$\mathbf{l}_{\mathbf{p}_{in}\mathbf{p}_{out}}(\mathbf{p}_{source}) = -\nabla V_{LE}(\mathbf{p}_{source}). \tag{2.34}$$

This is a very powerful result. The lead field at an arbitrary point $\mathbf{p}^*$ can be obtained by the negative gradient of the corresponding reciprocal potential field at the same position. Thus we can see that the lead field is exactly equal to the reciprocal electrical field

$$\mathbf{l}_{\mathbf{p}_{in}\mathbf{p}_{out}} = E_{LE}, \tag{2.35}$$

which is generated if a unit current is introduced to the lead. The lead is called *reciprocally energized* in that case. The lead field concept combined with the reciprocity principle is very powerful. It can be used in the following way:

- It can be used to visualize and evaluate the sensitivity distribution for a given lead, see Chapter 7 for an example.
- The lead field matrix can be calculated very fast and easily using reciprocity, see Section 2.5 for more details.
- We are able to calculate the sensitivity distribution in the measurement of electric impedance of the tissue, see Kauppinen et al. [26].
- Both, the lead field concept and the principle of reciprocity are also available for magnetic methods.

This description holds for arbitrarily shaped, inhomogeneous volume conductors since no assumptions have been made with respect to the volume conductor [29].

2.5 Using reciprocity for the EEG source simulation

The reciprocity principle can be used to calculate the lead field for a given lead in an alternative way. For many inverse source simulation approaches one needs to build the lead field matrix for many different dipole positions and orientations, see Section 2.3. For each column of the lead field matrix, the partial differential equation (2.18)-(2.19) for the EEG forward problem has to be solved. This is a very time consuming procedure.

To overcome this problem, the reciprocity principle can be applied. It is used to build the lead field matrix in a reciprocal way, which will considerably reduce the computation time. Instead of solving the partial differential equation for the EEG forward problem for each dipolar source, we set a unit current source and sink at each lead and calculate the resulting reciprocal potential field within the volume conductor. This has to be done for each lead and the resulting potential fields have to be stored. After the computation of the reciprocal potential field for each lead, we can easily calculate the lead field with equation (2.34). The lead field is given by the gradient of the reciprocal potential field, which can be calculated very fast and easily. The most time consuming part is the calculation of the reciprocal potential fields.

The reciprocal procedure has a big advantage: If the dipole position $\mathbf{p}$ is changed, we do not have to repeat solving the partial differential equation for the EEG forward problem again. Instead of this, only the gradient of the reciprocal potential field has to be calculated at the new dipole position.
If the lead field matrix is calculated in the standard way, the partial differential equation for the forward problem has to be solved new for each different dipolar position. If many different dipole positions are investigated, the reciprocal procedure will reduce the computation time drastically.

3 EEG forward approaches

In this chapter we introduce three different approaches that can be used to solve the EEG forward problem. The first one is the full subtraction approach, which is mathematically well-understood, see Wolters et al. [55]. The second approach we introduce is a direct potential approach called partial integration approach in Lew et al. [27]. The partial integration approach has the disadvantage that we do not have a well-understood mathematical theory. The last approach discussed in this chapter is the adjoint approach presented in Vallaghe et al. [46]. A derivation of the adjoint partial differential equation is presented in Section 3.3. Each approach is able to deal with arbitrary geometries and allows to treat tissue inhomogeneities as well as tissue anisotropies.

The solution of the EEG forward problem for an unbounded volume conductor with constant homogeneous conductivity can be calculated analytically as shown in the following example.

Example 1 (See Drechsler et al. [15])**.** *Let Ω be an unbounded volume conductor and let the conductivity σ be constant and homogeneous for all elements in the volume conductor Ω. Furthermore let Y be the source space and $\boldsymbol{x}_0 \in Y$ the position where the dipole is located. The solution $V^{\infty,\boldsymbol{x}_0}$ of the EEG forward problem can be calculated analytically via*

$$V^{\infty,\boldsymbol{x}_0}(\boldsymbol{x}) = \frac{1}{4\pi\sqrt{det\ \sigma(\boldsymbol{x}_0)}} \frac{< \boldsymbol{q}(\boldsymbol{x}_0), \sigma(\boldsymbol{x}_0)^{-1}(\boldsymbol{x}-\boldsymbol{x}_0) >}{< \sigma(\boldsymbol{x}_0)^{-1}(\boldsymbol{x}-\boldsymbol{x}_0), (\boldsymbol{x}-\boldsymbol{x}_0) >^{\frac{3}{2}}} \tag{3.1}$$

and the gradient of $V^{\infty,\boldsymbol{x}_0}$ can be easily obtained

$$\nabla V^{\infty,\boldsymbol{x}_0}(\boldsymbol{x}) = \frac{1}{4\pi\sqrt{det\ \sigma(\boldsymbol{x}_0)}} \frac{\sigma(\boldsymbol{x}_0)^{-1}\boldsymbol{q}(\boldsymbol{x}_0)}{< \sigma(\boldsymbol{x}_0)^{-1}(\boldsymbol{x}-\boldsymbol{x}_0), (\boldsymbol{x}-\boldsymbol{x}_0) >^{\frac{3}{2}}} \tag{3.2}$$

$$- \frac{1}{4\pi\sqrt{det\ \sigma(\boldsymbol{x}_0)}} \frac{3 < \boldsymbol{q}(\boldsymbol{x}_0), \sigma(\boldsymbol{x}_0)^{-1}(\boldsymbol{x}-\boldsymbol{x}_0) > \sigma(\boldsymbol{x}_0)^{-1}(\boldsymbol{x}-\boldsymbol{x}_0)}{< \sigma(\boldsymbol{x}_0)^{-1}(\boldsymbol{x}-\boldsymbol{x}_0), (\boldsymbol{x}-\boldsymbol{x}_0) >^{\frac{5}{2}}} \tag{3.3}$$

Since the denominator at position $\mathbf{x} = \mathbf{x}_0$ is zero, we can see that $V^{\infty,\mathbf{x}_0}(\mathbf{x})$ has a singularity at position $\mathbf{x} = \mathbf{x}_0$, which is of second order. It follows that $V^{\infty,\mathbf{x}_0}$

does not belong to the Sobolov space $W^1(\Omega)$ and to the Lebesque space $L^2(\Omega)$. In the following part of this chapter, we present different forward approaches and investigate if and how they treat the singularity at $\mathbf{x} = \mathbf{x}_0$.

3.1 Full subtraction approach

In this section, we briefly discuss some basics of the full subtraction approach presented in Wolters et al. [55] and Drechsler et al. [15].
Let Y be the gray matter compartment in which the dipolar sources are located and let Ω be the head domain. For the full subtraction approach let us assume that for each $y \in Y$ we are able to find a small subarea Ω_ϵ in which the conductivity σ is homogeneous for each $\mathbf{x} \in \Omega_\epsilon$, the so called *homogeneity assumption*.
In order to get rid of the singularity presented in Example 1, we split the total potential $V(\mathbf{x})$ into the singularity potential $V^{\infty,\mathbf{x}_0}(\mathbf{x})$ and the correction potential $V^{corr,\mathbf{x}_0}(\mathbf{x})$

$$V(\mathbf{x}) = V^{\infty,\mathbf{x}_0}(\mathbf{x}) + V^{corr,\mathbf{x}_0}(\mathbf{x}), \tag{3.4}$$

where $V^{\infty,\mathbf{x}_0}(\mathbf{x})$ is the solution for the unbounded volume conductor Ω with constant homogeneous conductivity σ presented in Example 1. For a complete solution of the EEG forward problem, the full subtraction approach calculates the solution for the correction potential $V^{corr,\mathbf{x}_0}(\mathbf{x})$ such that

$$\nabla \cdot \sigma(\mathbf{x}) \nabla (V^{\infty,\mathbf{x}_0}(\mathbf{x}) + V^{corr,\mathbf{x}_0}(\mathbf{x})) = \nabla \cdot \mathbf{J}^p(\mathbf{x}) \quad \mathbf{x}\ in\ \Omega \tag{3.5}$$

$$< \sigma(\mathbf{x}) \nabla (V^{\infty,\mathbf{x}_0}(\mathbf{x}) + V^{corr,\mathbf{x}_0}(\mathbf{x})), \mathbf{n}(\mathbf{x}) > = 0 \quad \mathbf{x}\ on\ \partial\Omega \tag{3.6}$$

$$\int_\Omega (V^{\infty,\mathbf{x}_0}(\mathbf{x}) + V^{corr,\mathbf{x}_0}(\mathbf{x}))\ dx = 0 \tag{3.7}$$

This equation system is called the *subtraction forward problem*.
The subtraction forward problem can be reorganized to

$$\nabla \cdot \sigma(\mathbf{x}) \nabla V^{corr,\mathbf{x}_0}(\mathbf{x}) = f(\mathbf{x}) \quad \mathbf{x}\ in\ \Omega \tag{3.8}$$

$$< \sigma(\mathbf{x}) \nabla V^{corr,\mathbf{x}_0}(\mathbf{x}), \mathbf{n}(\mathbf{x}) > = g(\mathbf{x}) \quad \mathbf{x}\ on\ \partial\Omega \tag{3.9}$$

$$\int_\Omega V^{\infty,\mathbf{x}_0}(\mathbf{x}) = -\int_\Omega V^{corr,\mathbf{x}_0}(\mathbf{x})\ dx \tag{3.10}$$

where the right-hand sides $f(\mathbf{x})$ and $g(\mathbf{x})$ are given by

$$f(\mathbf{x}) = \nabla \cdot (\sigma(\mathbf{x}_0) - \sigma(\mathbf{x})) \nabla V^{\infty,\mathbf{x}_0}(\mathbf{x}) \quad \mathbf{x}\ in\ \Omega$$

$$g(\mathbf{x}) = - < \sigma(\mathbf{x}) \nabla V^{\infty,\mathbf{x}_0}(\mathbf{x}), \mathbf{n}(\mathbf{x}) > \quad \mathbf{x}\ on\ \partial\Omega$$

For a numerical computation of $V^{corr,\mathbf{x}_0}(\mathbf{x})$ we need $V^{\infty,\mathbf{x}_0}(\mathbf{x})$ and $\nabla V^{\infty,\mathbf{x}_0}(\mathbf{x})$, which can be solved analytically following Example 1.
Solving $V^{corr,\mathbf{x}_0}(\mathbf{x})$ numerically leads to the following linear system

$$KV = b,$$

where the stiffness matrix is given by

$$K_{ij} = \int_\Omega < \sigma(\mathbf{x})\nabla\phi_i, \nabla\phi_j > \; dx, \qquad i,j = 1,\cdots,N$$

and the right-hand side vector b is given by

$$\begin{aligned} b_i = &\int_\Omega < (\sigma(\mathbf{x}_0) - \sigma(\mathbf{x}))\nabla V^{\infty,\mathbf{x}_0}(\mathbf{x}), \nabla\phi_i(\mathbf{x}) > \; dx \\ &- \int_{\partial\Omega} \phi_i(\mathbf{x}) < \sigma(\mathbf{x}_0)\nabla V^{\infty,\mathbf{x}_0}(\mathbf{x}), \mathbf{n}(\mathbf{x}) > \; ds, \qquad i = 1,\cdots,N. \end{aligned}$$

After solving this system, the potential $V(\mathbf{x})$ is the sum of $V^{\infty,\mathbf{x}_0}(\mathbf{x})$ and $V^{corr,\mathbf{x}_0}(\mathbf{x})$. The existence and uniqueness of a solution of the subtraction forward problem is presented in Wolters et al. [55].
Solving the full subtraction approach yields the question:

- What happened to the singularity in the volume conductor Ω? Is the singularity eliminated?

Since we have assumed that we are able to find a non empty subset Ω_ϵ where the homogeneity assumption holds, we have

$$\sigma(\mathbf{x}) - \sigma(\mathbf{x}_0) = 0 \quad \forall\, \mathbf{x} \in \Omega_\epsilon$$

where the function $V^{\infty,\mathbf{x}_0}(\mathbf{x})$ is singular. And therefore, the right-hand side $f(\mathbf{x})$ in equation (3.8) equally to zero. The full subtraction approach can thus be used to eliminate the singularity on the right-hand side $\nabla \cdot \mathbf{J}^p$. Furthermore, the right-hand side $f(\mathbf{x})$ in equation (3.8) is now square integrable over Ω.

3.2 Partial integration approach

Instead of building a singularity function as done in the subtraction approach, the partial integration approach, presented in Lew et al. [27], calculates the solution of the EEG forward problem in a direct way. The singularity in the domain Ω is neglected. Thus, we multiply the potential equation (2.18) with a linear finite element basis function ϕ_i and integrate over the head domain Ω

$$\int_\Omega \nabla \cdot (\sigma\nabla V)\phi_i \; dx = \int_\Omega \nabla \cdot \mathbf{J}^p \phi_i \; dx. \tag{3.11}$$

Now, we integrate both sides by parts

$$-\int_\Omega < \sigma \nabla V, \nabla \phi_i > \, dx + \int_{\partial\Omega} < \sigma \nabla V, \mathbf{n} > \phi_i \, ds = -\int_\Omega < \mathbf{J}^p, \nabla \phi_i > \, dx + \int_{\partial\Omega} < \mathbf{J}^p, \mathbf{n} > \phi_i \, ds.$$

The second term on the left-hand side vanishes due to the homogeneous Neumann boundary condition (2.19) and the second term on the right-hand side due to the fact that we do not have a current $\mathbf{J}^p$ on the surface of the volume conductor.
As mentioned in Section 2.2.4, the current density $\mathbf{J}^p$ on the right-hand side can be represented by

$$\mathbf{J}^p = \mathbf{q}\delta(\mathbf{x} - \mathbf{x}_0).$$

This leads to the following representation

$$\int_\Omega < \sigma \nabla V, \nabla \phi_i > \, dx = \int_\Omega < \mathbf{q}\delta(\mathbf{x} - \mathbf{x}_0), \nabla \phi_i > \, dx \; = < \mathbf{q}, \nabla \phi_i(\mathbf{x}_0) > . \tag{3.12}$$

In order to solve this equation with the finite element method, the function V is projected into the finite element space by

$$V(\mathbf{x}) \approx V_h(\mathbf{x}) = \sum_{j=1}^{N} \phi_j(\mathbf{x}) V_j, \quad V_j = V(\mathbf{x}_j).$$

This leads to the following system of linear equations

$$KV = b$$

with the stiffness matrix

$$K_{i,j} = \int_\Omega < \sigma \nabla \phi_j, \nabla \phi_i > \, dx, \qquad i, j = 1, \cdots, N.$$

Following equation (3.12) the right-hand side vector can be obtained by

$$b_i = \begin{cases} < \mathbf{q}, \nabla \phi_i(\mathbf{x}_0) >, & \text{if } i \in NodesOfEle(\mathbf{x}_0) \\ 0, & \text{otherwise} \end{cases} \tag{3.13}$$

the function $NodesOfEle(\mathbf{x}_0)$ calculates the corner nodes of the element, in which the dipole is located.

When we investigate the deduction of the partial integration approach, we obtain the following question:

- Is the derivation of the partial integration approach mathematically correct?

Integration by parts of the right-hand side is used in equation (3.11). In this case, it is assumed that the current source $\mathbf{J}^p$ is differentiable. In the partial integration approach, we used a dipole source as current source, modelled as a Dirac-delta distribution, which is not differentiable. Thus, another question appears:

- Does the partial integration approach lead to correct results for the EEG forward problem?

In [27], Lew et al. investigated different forward approaches for EEG source analysis. They compared the full subtraction approach to the Venant approach and the partial integration approach. In Table 3, they describe the maximal relative error and the maximal magnitude error for 6 different tetrahedral meshes. We can see that the partial integration approach leads to acceptable results. Lew et al. concluded that the full subtraction approach performs better as long as the homogeneity assumption is sufficiently fulfilled. In addition, they mentioned an oscillatory behavior of the partial integration approach. In that work, Lew at al. used tetrahedral meshes with linear finite element shape functions for the partial integration approach. Thus, to compute the right-hand side vector b via equation (3.13), the gradient of linear finite element shape functions has to be calculated. This leads to constant values within the complete element.

3.3 The adjoint approach

The adjoint approach for the EEG forward problem is presented in this section. In the first part, the adjoint partial differential equation is deduced from the adjoint method presented in Vallaghe et al. [46]. In the last part of this section we will explain how the adjoint method can be used to calculate the lead field for a given sensor configuration. The notations presented in Vallaghe et al. [46] are used.

In the further steps, the function $g(\mathbf{J}^p)$ describes the difference between the electric potential V measured at the positon $\mathbf{r}_i$ of the EEG electrode and the reference electrode located at $\mathbf{r}_0$.
The following parameters are used [46]:

- We assume $E = L^2(\Omega)$, the head domain $\Omega \subset \mathbb{R}^3$ and the inner product

$< u, v > = \int_\Omega u(\mathbf{x})v(\mathbf{x})\ dx$ ($L^2(\Omega)$ is a Hilbert space, following Theorem 6 in the Appendix A.2)

- The parameter p is the primary current vector field $\mathbf{J}^p(\mathbf{x}) \in E^3 = (L^2(\Omega))^3$.
- The parameter v is the electric potential $V(\mathbf{x}) \in \mathcal{C}^0(\Omega) \cap E = \mathcal{C}^0(\Omega) \cap L^2(\Omega)$.
- We have $g(\mathbf{J}^p) = f(V(\mathbf{J}^p)) = V(\mathbf{r}_i) - V(\mathbf{r}_0) = \int_{\partial\Omega} V(\delta_{\mathbf{r}_i} - \delta_{\mathbf{r}_0})$ ds.
- V is solution of the EEG forward problem (2.18)-(2.19)

$$\begin{aligned} \nabla \cdot (\sigma \nabla V) &= \nabla \cdot \mathbf{J}^p \qquad && in\ \Omega \\ < \sigma \nabla V, \mathbf{n} > &= 0 && on\ \partial\Omega \end{aligned}$$

- The Lagrangian L is given by

$$L(\mathbf{J}^p, V, w) = \int_{\partial\Omega} V(\delta_{\mathbf{r}_i} - \delta_{\mathbf{r}_0})\ ds + \int_\Omega (\nabla \cdot (\sigma \nabla V) - \nabla \cdot \mathbf{J}^p) w\ dx.$$

In order to obtain the adjoint partial differential equation the Lagrangian L has to be rewritten. This has to be done, since we have to calculate the differential of L with respect to the electric potential V. According to Section 2.2.5, the electric potential V and $\sigma\nabla V$ are continuous within the volume conductor and along the interfaces lying in it, which gives the possibility to use the divergence theorem

$$\int_\Omega (\nabla \cdot (\sigma \nabla V)) w\ dx = \int_{\partial\Omega} w < \sigma \nabla V, \mathbf{n} >\ ds - \int_\Omega < \sigma \nabla V, \nabla w >\ dx \quad (3.14)$$

The first term on the right-hand side is zero, since a homogeneous Neumann boundary conditions is considered. Next, we have

$$\int_\Omega (\nabla \cdot (\sigma \nabla w)) V\ dx = \int_{\partial\Omega} V < \sigma \nabla w, \mathbf{n} >\ ds - \int_\Omega < \sigma \nabla w, \nabla V >\ dx \quad (3.15)$$

The conductivity σ is symmetric, therefore $\sigma = \sigma^T$ and we can write

$$\int_\Omega < \sigma \nabla w, \nabla V >\ dx\ = \int_\Omega < \sigma^T \nabla w, \nabla V >\ dx$$

We can now combine the steps above to obtain

$$\begin{aligned} \int_\Omega (\nabla \cdot (\sigma \nabla V)) w\ dx &= -\int_\Omega < \sigma \nabla V, \nabla w >\ dx \\ &= -\int_\Omega < \nabla w, \sigma \nabla V >\ dx \\ &= -\int_\Omega < \sigma^T \nabla w, \nabla V >\ dx \\ &= -\int_\Omega < \sigma \nabla w, \nabla V >\ dx \\ &\overset{(3.15)}{=} \int_\Omega (\nabla \cdot (\sigma \nabla w)) V\ dx - \int_{\partial\Omega} V < \sigma \nabla w, \mathbf{n} >\ ds \end{aligned}$$

The corresponding term in the Lagrangian can be replaced

$$L(\mathbf{J}^p, V, w) = \int_{\partial\Omega} V(\delta_{\mathbf{r}_i} - \delta_{\mathbf{r}_0})\, ds + \int_\Omega (\nabla \cdot (\sigma \nabla w))V\, dx$$
$$- \int_{\partial\Omega} V < \sigma \nabla w, \mathbf{n} >\, ds - \int_\Omega (\nabla \cdot \mathbf{J}^p) w\, dx$$

We are now able to calculate the differential of $L(\mathbf{J}^p, V, w)$ with respect to V. We have

$$\frac{\partial L}{\partial V}(\mathbf{J}^p, V, w) = \int_{\partial\Omega} (\delta_{\mathbf{r}_i} - \delta_{\mathbf{r}_0})\, ds + \int_\Omega \nabla \cdot (\sigma \nabla w)\, dx - \int_{\partial\Omega} < \sigma \nabla w, \mathbf{n} >\, ds$$

Thus, the condition $\frac{\partial L}{\partial V}(\mathbf{J}^p, V, w) = 0$ is fulfilled, if w is the solution of

$$\nabla \cdot (\sigma \nabla w) = 0 \qquad in\ \Omega \tag{3.16}$$
$$< \sigma \nabla w, \mathbf{n} > = \delta_{\mathbf{r}_i} - \delta_{\mathbf{r}_0} \qquad on\ \partial\Omega \tag{3.17}$$

This equation system is called the *adjoint partial differential equation.*

In the next part of this section we describe, how the adjoint method can be used to calculate the lead field for a given lead at position $\mathbf{r}_i$ and $\mathbf{r}_0$. We have the following relationship between the derivative of the functional g and the derivative of the Lagrangian L with respect to $\mathbf{J}^p$

$$\frac{\partial g}{\partial \mathbf{J}^p} = \frac{\partial L}{\partial \mathbf{J}^p}.$$

Thus the lead field for a given sensor configuration can be calculated with the derivative of the Lagrangian L with respect to $\mathbf{J}^p$.
The Lagrangian L only depends on $\mathbf{J}^p$ via the expression

$$- \int_\Omega (\nabla \cdot \mathbf{J}^p) w\, dx$$

which can be rewritten as

$$- \int_\Omega (\nabla \cdot \mathbf{J}^p) w\, dx = \int_\Omega < \nabla w, \mathbf{J}^p >\, dx - \int_{\partial\Omega} < \mathbf{J}^p, \mathbf{n} > w\, dx.$$

The last term is zero due to the known fact, that the primary current vector $\mathbf{J}^p$ is zero on the boundary $\partial\Omega$. We finally obtain

$$\frac{\partial g}{\partial \mathbf{J}^p} = \frac{\partial L}{\partial \mathbf{J}^p} = \nabla w. \tag{3.18}$$

The lead field is given by the expression $\frac{\partial g}{\partial \mathbf{J}^p}$, see Vallaghe et al. [46], which can be calculated using equation (3.18). Summing up, to be able to calculate the lead field for a given lead at position $\mathbf{r}_i$ and $\mathbf{r}_0$, the adjoint partial differential equation (3.16)-(3.17) has to be solved for a finite number N of grid nodes.

Then, equation (3.18) has to be used to calculate the gradient of the solution w of (3.16)-(3.17) at the corresponding grid nodes. Since the calculation of the solution w of the adjoint partial differential equation is the major time consuming part and it has to be solved only sensor nodes minus one times, this procedure will speed up the calculation of the lead field matrix. The adjoint method gives us the possibility to calculate the lead field matrix for a big number N of discrete sources in a feasible calculation time. This is based on the fact, that the calculation of ∇w is very fast and easy.

To summarize, the partial differential equation for the EEG forward problem is given by

$$\begin{aligned} \nabla \cdot \sigma \nabla V &= \nabla \cdot \mathbf{J}^p \qquad in \quad \Omega \\ < \sigma \nabla V, \mathbf{n} > &= 0 \qquad on \quad \partial\Omega \end{aligned}$$

and the adjoint partial differential equation is given by

$$\begin{aligned} \nabla \cdot \sigma \nabla w &= 0 \qquad in \quad \Omega \\ < \sigma \nabla w, \mathbf{n} > &= \delta_{\mathbf{r}_i} - \delta_{\mathbf{r}_0} \qquad on \quad \partial\Omega \end{aligned}$$

The adjoint partial differential equation is a *Laplace equation* with *inhomogeneous Neumann boundary* condition, see Braess [5] for further details. Related to Helmholtz' reciprocity principle, the expression $\delta_{\mathbf{r}_i} - \delta_{\mathbf{r}_0}$ stands for the lead, where the current source and sink is placed.

After solving the adjoint partial differential equation, there are some questions:

- 1. How do we obtain the desired potential V at each electrode position?

- 2. What happened to the singularity in the partial differential equation for the EEG forward problem. Is the singularity alleviated?

To the first question:
Solving (3.16)-(3.17) leads to a solution w at each grid point within the volume conductor Ω. In this case, only the resulting potential at the electrode positions, given by the adjoint solution w is obtained. But we want to obtain the potential difference between a given lead of the electric potential V. It is thus the goal to combine the solution V of the EEG forward problem and the solution w of the adjoint partial differential equation. If dipolar sources are used, this can be

done in the following way:
The lead field for a given measurement between a lead is exactly given by ∇w. If a dipolar source positioned at $\mathbf{x}_0$ with dipole moment $\mathbf{q}$ is used, we have according to Section 2.2.4 $\mathbf{J}^p = \mathbf{q}\delta(\mathbf{x} - \mathbf{x}_0)$. Using Example 2 in the Appendix A.1 with $L_{i0}(\mathbf{x}) = \nabla w$ yields

$$V(\mathbf{r}_i) - V(\mathbf{r}_0) = \int_\Omega < \nabla w, \mathbf{J}^p > = < \mathbf{q}, \nabla w(\mathbf{x}_0) > .$$

Thus, the potential difference between the i-th scalp electrode and the reference electrode located at $\mathbf{r}_0$ can be obtained by calculating the gradient of the adjoint solution w and evaluating the calculated gradient of w at the dipole position, multiplied with the dipole moment $\mathbf{q}$.

This step is very problematic. We considered the primary current vector $\mathbf{J}^p$ to be an element in the space $L^2(\Omega)$. But a dipole is not an element of the space $L^2(\Omega)$. The following condition is fulfilled

$$\delta_p(\mathbf{x}) \in W^{-\frac{3}{2}-\epsilon}(\Omega) \quad \forall \epsilon > 0.$$

This point has to be investigated, but is not part of this thesis.

To the second question:
The singularity in the volume conductor Ω is eliminated. But due to the boundary condition in the adjoint partial differential equation, we have a singularity on the boundary. This singularity is caused by the missing divergence operator in the boundary condition, of one order lower, that is, a singularity of first order, than the singularity in the volume for the partial integration approach. Therefore, we have to check the following questions:

- Which singularity can be handled better?
- Do we receive significant differences with regard to numerical errors?

In the numerical simulation part, we are going to present the resulting error curves for the partial integration approach and the adjoint approach for different tetrahedral and hexahedral meshes, where we deeply discuss this questions.

4 Implementation

Since we want to solve the partial differential equation for the EEG forward problem, the volume conductor has to be modelled. The human head consists of different compartments, for example, scalp, skull, CSF, gray matter and white matter with different conductivities. Additionally, Wolters explained in [52] that the white matter compartment is anisotropic and Dannhauer [13] recommended that the skull should be modelled three-layered with spongiosa and compacta. To be able to reconstruct the EEG sources precisely, the exact modeling of the tissue inhomogeneity and anisotropy is needed, see, for example, Wolters [52] and Haueisen et al. [23].
There are different numerical approaches which can be used to solve the EEG forward problem, like the *boundary element method* (BEM), the *finite differences method* (FDM) and the finite element method (FEM). Only the FEM and the FDM are able to deal with both, realistic head models and inhomogeneous and anisotropic compartments. According to Wolters [52] the FEM is used in this thesis due to the fact that a big advantage of the FEM is that the Galerkin discretization and the weak formulation of the forward problem (2.18)-(2.19) gives on the one hand the chance to model the physics appropriately and accurately and on the other hand it gives a clear mathematical treatment of low regularity cases. The EEG source analysis task with discontinuous conductivity values is an example for those low regularity cases, see Section 2.2.5 for more details on that topic.

4.1 Finite element method

In 1852 Karl Schellenbach [42] described the solution of minimal surface problems. In his work, Schellenbach used methods, that can be seen as early forms of the finite element method used today. His approach could be compared to the finite element method with linear triangle elements on a regular grid. Over 50 years later, Ritz [37] and Galerkin invented their Ritz and Galerkin approach. The finite element method is a special form of a Ritz and Galerkin approach.

For more details on that topic, see, for example, Braess [5].
In the work *The finite element method in plane stress analysis* by R. W. Clough in the [11], Clough introduced the notation finite element method.
In the following, we briefly explain some basics of the finite element method:

We will follow the basic ideas of Burger [10]. The finite element method decomposes the domain Ω into a *finite* number of subareas, which are called *elements*. Examples are triangles or rectangles in 2D and tetrahedras or cubes in 3D. The next point is the definition of finite element shape functions on every element, which can, for example, be linear, quadratic or cubic. Another interesting point to explain is how the domain Ω can be decomposed into subdomains. We will restrict the following topic to the twodimensional case. Note that an analogous procedure is also available for higher dimensions.

A *feasible* decomposition is explained in the following

Sentence 1. *(Feasible division, see: [5]) A decomposition $\tau = T_1, \cdots, T_m$ of a domain Ω is called feasible if the following conditions are fulfilled*

1. $\overline{\Omega} = \bigcup_{i=1}^{M} T_i$
2. *If $T_i \cap T_j$ has exactly one point, this point is a corner node of T_i and T_j*
3. *If $T_i \cap T_j$ has more than one point, $T_i \cap T_j$ is an edge of T_i and T_j*

It is thus important that the complete domain Ω is overlapped by elements. Furthermore we can see that $T_i \cap T_j$ is empty or exactly one point or exactly an edge.
The neighborhood of a node P_i is defined by

$$N(P_i) = \bigcup_{P_i \in \partial T_j} T_j.$$

The neighborhood is therefore given by the neighboring elements of the grid node. For each grid point a finite element shape function with the following properties is defined:

$$\begin{aligned}
&\phi \in C(\overline{\Omega}) \\
&\phi_i|_{\mathbf{x}_l} = \delta_{il} \\
&\phi_i(\mathbf{x}) = 0 \qquad\quad \mathbf{x} \notin N(P_i) \\
&\phi_i|_{T_j} \in \mathcal{P}_k(T_j) \quad T_j \subset N(P_i)
\end{aligned}$$

The expression $\mathcal{P}_k(T_j)$ describes the set of polynomials, with a degree smaller or equal to k. For the adjoint approach and the partial integration approach, linear finite element shape functions are used, that is, $k = 1$.

We are now able to use the finite element method for a discretization of the adjoint partial differential equation presented in (3.16)-(3.17). In order to solve the adjoint partial differential equation with the FEM, we multiply equation (3.16) with a finite element basis function $\phi \in C^\infty(\Omega)$ and integrate over the domain Ω

$$\int_\Omega \nabla \cdot (\sigma \nabla w)\phi \, dx = 0. \tag{4.1}$$

The divergence theorem yields

$$-\int_\Omega < \sigma \nabla w, \nabla \phi > \, dx + \int_{\partial\Omega} < \sigma \nabla w, \mathbf{n} > \phi \, ds = 0.$$

We use the boundary condition (3.17) to reformulate the second term on the left-hand side

$$\int_\Omega < \sigma \nabla w, \nabla \phi > \, dx = \int_{\partial\Omega} (\delta_{\mathbf{r}_i} - \delta_{\mathbf{r}_0})\phi \, ds. \tag{4.2}$$

Once again the function w is projected into the finite element space by

$$w(\mathbf{x}) \approx w_N(\mathbf{x}) = \sum_{j=1}^{N} \phi_j(\mathbf{x}) w_j, \quad w_j = w(\mathbf{x}_j), \tag{4.3}$$

where N is the number of grid nodes and $w(\mathbf{x}_j)$ is given by the value of the solution of the adjoint partial differential equation w at the j-th grid node. In addition, the following stiffness matrix K is used

$$K_{ij} = \int_\Omega < \sigma \nabla \phi_i, \nabla \phi_j > \, dx, \qquad i, j = 1, \cdots, N$$

and the following right-hand side vector b

$$b_j = \int_{\partial\Omega} (\delta_{\mathbf{r}_i} - \delta_{\mathbf{r}_0})\phi_j \, ds, \qquad j = 1, \cdots, N, \tag{4.4}$$

to be able to rewrite equation (4.2) in the following form

$$Kw = b. \tag{4.5}$$

The same proceeding for the EEG forward problem (2.18) leads to a linear system with another right-hand side vector b

$$KV = b. \tag{4.6}$$

4.2 Transfer matrix approach

To solve the linear system (4.6) is the major time consuming part within the source localization process. Many inverse solution approaches need to solve the system (4.6) for many different right-hand sides. In Section 2.4 we discussed the reciprocity principle invented by Helmholtz. In the reciprocal case, the system (4.6) has to be solved only sensor nodes less one time.
In this section we introduce the *transfer matrix approach* presented in Wolters et al [51] and Weinstein et al. [49]. It is another approach that considerably reduces the computation time. Instead of solving the forward problem for each possible dipolar source and orientation, a restriction matrix $R \in \mathbb{R}^{(S-1)\times N}$ is introduced. An important point is that each of the S EEG electrodes exactly correspond to a finite element node at the surface of the volume conductor Ω. The matrix R has only one non zero entry per row. To map the potential vector V to the (S-1) non-reference electrodes, the value 1 is placed at the corresponding grid node of R and we receive

$$V_{EEG} := RV. \tag{4.7}$$

Following Wolters et al. [51], we define the *transfer matrix* T as follows

$$T := RK^{-1} \in \mathbb{R}^{(S-1)\times N}. \tag{4.8}$$

Then, we multiply equation (4.6) with the transfer matrix T from the left-hand side

$$Tb \overset{(4.6)}{=} TKV \overset{(4.8)}{=} RK^{-1}KV = RV \overset{(4.7)}{=} V_{EEG}. \tag{4.9}$$

If the transfer matrix is once calculated, the potential at the EEG electrodes can be calculated using the product of the transfer matrix T with the right-hand side vector b.

An interesting question is how the transfer matrix T could be calculated. The calculation of T will be very difficult, due to the fact that the sparsity of the stiffness matrix K will be lost when inverting it. Thus, another approach to calculate the transfer matrix T is introduced. The stiffness matrix K will be multiplied from the right-hand side to equation (4.8). This leads to

$$TK = RK^{-1}K = R. \tag{4.10}$$

Using the fact that K is symmetric and transposing both sides of equation (4.10) yields

$$KT^T = K^T T^T = R^T. \tag{4.11}$$

Thus, to calculate the transfer matrix T, we have to solve (S-1) sparse finite element linear equation systems. If the source location is changed, we do not have to solve the linear system (4.6) completely new with another right-hand side vector b. The transfer matrix is valid for each possible source location within the volume conductor Ω. Once the transfer matrix T is calculated, the forward computation for an arbitrary source location is reduced to a single matrix multiplication with T. The transfer matrix approach can be applied to inverse reconstruction algorithms in the continuous and the discrete source parameter space for EEG and MEG, see Wolters et al. [51].

4.3 Implementation of the adjoint approach

A possible realization of the adjoint approach for the EEG forward problem is presented in this section. A major work of this thesis was the development and the implementation of the presented algorithms. The algorithms were realized and implemented into the SimBio software package, see [44] for further details.

We divided the calculation of the potential difference $V(\mathbf{r}_i) - V(\mathbf{r}_0)$ between each lead positioned at $\mathbf{r}_i$ and $\mathbf{r}_0$ into three subparts:

1. Solve the partial differential equation (3.16)-(3.17) for each sensor configuration and save the calculated values of the adjoint solution w.
2. Calculate $\nabla\phi_j(\mathbf{x}_0)$ at the corresponding dipole element nodes.
3. Calculate potential difference $V(\mathbf{r}_i) - V(\mathbf{r}_0)$ for each sensor configuration.

For each of the three subparts we developed algorithms which will be presented and explained in the following part of this section.

Algorithm 1 Solve the adjoint partial differential equation for each lead

```
for i = 1 to SensorNodes.length() do
  b(SensorNodes[0]) = -1;
  b(SensorNodes[i]) = 1;
  Solve: Kw = b;
  b(SensorNodes[i]) = 0;
  for j = 0 to NumberOfGridNodes do
    W(j + (i-1)*NumberOfGridNodes) = w(j);
  end for
end for
```

In the first algorithm, a $N \times (S-1)$ matrix W is calculated. Here N stands for the number of grid nodes and S is given by the number of sensors. The i-th column of W contains the solution of the adjoint partial differential equation (3.16)-(3.17) at each grid node within the volume conductor Ω, corresponding to the i-th lead. When the first algorithm is finished, the matrix W contains the solution w of the adjoint partial differential equation for each grid point and each lead.
In order to be able to solve the linear system (4.5), the stiffness matrix K has to be created, see Section 4.1 for further details. It is a $N \times N$ matrix with coefficients

$$K_{ij} = \int_{\Omega} < \sigma \nabla \phi_i, \nabla \phi_j > \, dx, \qquad i,j \; = \; 1, \cdots, N.$$

This is done in a former step. The computation of the matrix W starts with a loop over all EEG leads. This has to be done since we have to solve the system (4.5) for each different right-hand side vector b, that is, for each different EEG lead. Since we set a reference electrode at the first scalp electrode position, we have exactly sensor nodes less one scalp electrode pairs. This leads to (S-1) loop steps. Let us denote in the following the i-th loop step with an index i. In order to solve the adjoint partial differential equation, the right-hand side vector b has to be built. Following equation (4.4), b has only two non zero entries. The grid node corresponding to the first electrode, that is, the reference electrode has the value -1 and the grid node corresponding to the i-th EEG scalp electrode has a value of 1.
After that step, we are able to solve the linear system (4.5). We use an algebraic multigrid - conjugate gradient solver (AMG-CG) [51] to solve $Kw = b$. Based on the fact that the right-hand side vector b changes in the next loop step, we have to set, after solving $Kw = b$, the i-th grid node value of the right-hand side vector b to zero. Since the first electrode is used as reference, we do not have to set the grid node corresponding to the first scalp electrode to zero. As a last step the results have to be stored in the matrix W. The calculation of W could be seen as a *preparatory step*. This notation is based on the fact that the calculation of the solution matrix W has to be finished until the second and third algorithm could be started. If the solution matrix W is once calculated, the potential difference $V(\mathbf{r}_i) - V(\mathbf{r}_0)$ for each lead can be calculated very fast and easily.

In the second algorithm we calculate $\nabla \phi_i(\mathbf{x}_0)$ at the dipole position $\mathbf{x}_0$. Since

Algorithm 2 Calculate $\nabla\phi_j(\mathbf{x}_0)$ for the element, which contains the dipole

```
Find DipolElement;
for i = 0 to nodespelem do
  locnode[i] = i-th NodeOfDipoleElement;
  coords[i*3 + 0] = x-coordinate;
  coords[i*3 + 1] = y-coordinate;
  coords[i*3 + 2] = z-coordinate;
end for
Find DipolPosition;
fofagn(DipolElement, DipolPosition, locnode, coords, phi-grad);
```

we have

$$\nabla w(\mathbf{x}) \approx \sum_{j=1}^{N} \nabla\phi_j(\mathbf{x}) w_j,$$

and the definition of finite element shape functions

$$\phi_i(\mathbf{x}_j) = \begin{cases} 1, & \text{if } i = j \\ 0, & \text{otherwise} \end{cases} \tag{4.12}$$

only the values of $\nabla\phi_i(\mathbf{x}_0)$ have to be calculated for the element, which contains the dipole. Therefore, we have to find the dipole element. This can be done very easily in SimBio, since there is a function called find-dipole-ele. Then, we have to find the corner nodes and the corresponding coordinates (x,y,z) for the element, in which the dipole is located. This has to be done, since we use a Fortran routine called *fofagn*, which gives us the values of the derivative of finite element shape functions within elements. Naturally, the function fofagn needs the exact position of the examination point, that is, the exact dipole position. If tetrahedral models with linear finite element shape functions are used, the corresponding derivative is constant and therefore, we do not have a resolution in the element. We receive exactly the same values for the derivative of the finite element shape functions for each dipole position within the element. For second or third order shape functions, the exact position of the dipole within the element is needed, see Chapter 9 for further details. For hexahedral models we have a slightly different situation. The derivative of the finite element shape functions is not exactly constant. This is due to the transformation of the cube, in which the dipole is located into a unit cube located at the point of origin.
Due to the fact that the dipole element does not change for a modification of the lead, $\nabla\phi_i(\mathbf{x}_0)$ has to be calculated only once per dipole. The function fofagn provides us the values of $\nabla\phi_i(\mathbf{x}_0)$ at each corner node in direction of the x,y

and z-axis and the solution is stored in phi-grad.

Algorithm 3 Calculate potential difference $V(\mathbf{r}_i) - V(\mathbf{r}_0)$ for each lead

```
for i = 1 to SensorNodes.length() do
  ∇w = 0;
  for j = 1 to nodespelem(DipolElement) do
    ∇w(x_0) = ∇w(x_0) + ∇φ_j(x_0) w_j;
  end for
  V(r_i) − V(r_0) = < q, ∇w(x_0) >;
end for
```

In the third algorithm, the potential difference $V(\mathbf{r}_i) - V(\mathbf{r}_0)$ for each lead is calculated. To calculate the potential difference for all leads, the algorithm starts with a loop over all sensor node pairs. Then, we have to set ∇w to zero, so that the previously calculated values are eliminated. As mentioned in the discussion for the second algorithm, we do not have to sum over all grid nodes. We only have to sum over the corner nodes of the dipole element. Thus, we have to find out, how many nodes the element, in which the dipole is located has, for example, for tetrahedral meshes, we have 4 nodes, for cubic grids, the dipole element has 8 nodes. To sum up ∇w at each grid node, we have to build a loop over the former calculated number of corner nodes of the dipole element. Then, we calculate $\nabla w(\mathbf{x}_0)$ at each corner node of the corresponding dipole element. Here we use the former calculated values of w_i at the i-th grid node and the values of $\nabla \phi_i(\mathbf{x}_0)$ at each corner node of the dipole element. As mentioned before, the function fofagn calculates the values of finite element shape functions at the corresponding element corner nodes with regard to the examination point within the element. Since this is done in direction of the x- ,y- and z-axis, we have to sum up $\nabla \phi_j(\mathbf{x}_0) w_j$ in all three coordinate directions. This will lead to the required 3×1 vector ∇w, which is needed for the inner product with the 3×1 dipole moment vector $\mathbf{q}$. The potential difference between the lead positioned at $\mathbf{r}_i$ and $\mathbf{r}_0$ is then given by

$$V(\mathbf{r}_i) - V(\mathbf{r}_0) = < \mathbf{q}, \nabla w(\mathbf{x}_0) > .$$

4.4 Implementation of the partial integration approach

In this section we give some information about the implementation of the partial integration approach.

Following Section 3.2 a possible realization of the partial integration approach is presented in Algorithm 4.

Algorithm 4 Algorithm: Partial integration approach

```
Find DipolElement;
for i = 0 to nodespelem do
  locnode[i] = i-th NodeOfDipoleElement;
  coords[i*3 + 0] = x-coordinate;
  coords[i*3 + 1] = y-coordinate;
  coords[i*3 + 2] = z-coordinate;
end for
Find DipolPosition;
fofagn(DipolElement, DipolPosition, locnode, coords, phi-grad);
for i = 0 to nodespelem do
  b(locnode[i]) = < q, ∇φ_i(x_0) >;
end for
Solve KV = b;
for i = 0 to SensorNodes.length() do
  V(r_i) = V(SensorNodes[i]);
end for
```

The first point is to find the element that contains the dipole. To be able to use the Fortran routine fofagn, we have to find the corresponding corner nodes and the coordinates of that element. Since we use finite element shape functions, the same argumentation for the derivative of the shape function holds as in the adjoint approach. For tetrahedral meshes the derivative is constant and for hexahedral meshes the derivative is not completely constant. After that step, we set up the right-hand side vector b in the following way

$$b_i = \begin{cases} < \mathbf{q}, \nabla\phi_i(\mathbf{x}_0) >, & \text{if } i \in NodesOfEle(\mathbf{x}_0) \\ 0, & \text{otherwise} \end{cases}$$

The AMG-CG solver is then used to solve the following linear system

$$KV = b.$$

This leads to a solution V at each grid node. The resulting potential at the sensor nodes can then be evaluated by

$$V(\mathbf{r}_i) = V(SensorNodes(i)).$$

The partial integration approach was implemented in SimBio using the FEM Software library COLSAMM, see [54]. Due to the fact that we want to compare the arithmetic operations of the adjoint approach with the arithmetic operations of the partial integration approach, we implemented the calculation of the right-hand side vector b without COLSAMM. We used Fortran routines implemented in SimBio to calculate the right-hand side vector b. This will speed up the forward calculation with the partial integration approach since those routines are fast compared to the old COLSAMM routines.

Instead of comparing the adjoint approach with the partial integration approach presented in this chapter, we present a comparison to the partial integration approach with transfer matrices presented in Wolters et al. [51] and Section 4.2.

4.5 Comparison of arithmetic operations

In order to make a clear statement about the speed of the partial integration approach with respect to the speed of the adjoint approach, the aim of this section is the calculation of arithmetic operations needed to solve the EEG forward problem. A time dependent comparison of both approaches would strongly depend on the implementation.

We are going to present the results for three tetrahedral models with a different number of grid nodes, to show that the result does not depend on the number of grid nodes. The results for different hexahedral models are traced back to the results of the tetrahedral models at the end of this section.

The AMG-CG solver is needed in both approaches to solve the linear system $Kw = b$ and $KV = b$, respectively. Thus an estimate of the complexity of the AMG-CG solver is the starting point for this section. Wolters et al. [51] presented the complexity of the AMG-CG solver, where further details could be found.
To solve the linear system with the AMG-CG solver, we need $i \cdot k \cdot N$ operations with:

- i the number of iterations, we set $i = 20$ in the following,
- N the number of grid nodes,
- $k = \frac{8}{7}(2C_s + C_d + 2 + \frac{Cp+7}{c_{nz}}) \cdot c_{nz}$

and the values

- c_{nz} being the sparsity of the stiffness matrix, for example, for tetrahedral meshes 27.
- C_s the smoother costs, in the AMG-CG case, we have a Gauss-Seidel smoother with $C_s = 2 - \frac{2}{c_{nz}}$.
- C_p and C_d depends on the chosen prolongation operator.

This gives us the possibility to estimate the complexity of both approaches. We begin with the adjoint approach.
The calculation of the desired potential difference for all leads can be divided following Section 4.3 into three subtasks. To create the $N \times (S-1)$ matrix W, where the solution of the adjoint partial differential equation for each lead are stored

$$(S \text{ - } 1) \cdot (3 + i \cdot k \cdot N + N)$$

arithmetic operations are needed. This task requires 2 operations to build the right-hand side vector b and one operation to erase the i-th value of b after solving the linear system $Kw = b$. The solution of the linear system $Kw = b$ with the AMG-CG solver requires $i \cdot k \cdot N$ operations and the storage of the calculated values N arithmetic operations.
For the second and the third part of the calculation of the solution $V(\mathbf{r}_i)$ - $V(\mathbf{r}_0)$

$$\text{dip} \cdot (4 \cdot (1 + 3) + 207 + ((S \text{ - } 1) \cdot (3 + 4 \cdot 3 + 2 \cdot 3)))$$

arithmetic operations are needed. Here dip is given by the number of calculated dipoles. To save and calculate the nodes and the corresponding coordinates of the element, in which the dipole is located, $4 \cdot (1 + 3)$ arithmetic operations are needed. Furthermore, the Fortran routine fofagn, see Section 4.3, needs 207 arithmetic operations to calculate and save the gradient of the finite element shape function. Algorithm 3 combines the values computed before to create the solution $V(\mathbf{r}_i) - V(\mathbf{r}_0)$. This requires $((S \text{ - } 1) \cdot (3 + 4 \cdot 3 + 2 \cdot 3))$ arithmetic operations. First, ∇w has to be erased, this needs 3 operations. Then, $4 \cdot 3$ operations are needed to calculate ∇w and $2 \cdot 3$ operations to calculate the inner product with the dipole moment $\mathbf{q}$.
To summarize, to solve the forward problem with the adjoint approach

$$(S \text{ - } 1) \cdot (3 + i \cdot k \cdot N + N) + \text{dip} \cdot (4 \cdot (1 + 3) + 207 + ((S \text{ - } 1) \cdot (3 + 4 \cdot 3 + 2 \cdot 3)))$$

Method	71,896 nodes	360,056 nodes	503,180 nodes
Adjoint	$2{,}7135 \cdot 10^{11}$	$1{,}3589 \cdot 10^{12}$	$1{,}8991 \cdot 10^{12}$
Partial integration	$2{,}7140 \cdot 10^{11}$	$1{,}3592 \cdot 10^{12}$	$1{,}8995 \cdot 10^{12}$

Table 4.1: Arithmetic operations needed for tetrahedral meshes

operations are needed.

The complexity for the partial integration approach with transfer matrices can be calculated in the following way: To compute the transfer matrix T,

$$(S\text{ - }1) \cdot (N + i \cdot k \cdot N + N)$$

operations are needed. The calculation requires N operations to set up the right-hand side vector b. A value of 1 is set to the grid node, corresponding to the i-th sensor electrode. All other grid nodes were set to zero. Then, the solution V of $KV = b$ can be calculated with the AMG-CG solver. This requires $i \cdot k \cdot N$ arithmetic operations and the storage of the calculated values requires N operations.
To calculate the potential with the partial integration approach

$$\text{dip} \cdot (4 \cdot (1 + 3) + 207 + 4 + (S\text{ - }1) \cdot (1 + 4 + 1))$$

operations are needed. The term $4 \cdot (1 + 3) + 207 + 4$ is given by the calculation of the nodes and the coordinates of the dipole element and the calculation of the gradient of the finite element shape function ϕ at each corner node of the element, in which the dipole is located. Furthermore the partial integration approach requires $(S\text{ - }1) \cdot (1 + 4 + 1)$ arithmetic operations to calculate the resulting potential of V at the corresponding sensor nodes. In comparison, for a solution of the EEG forward problem with the partial integration approach with transfer matrices

$$(S\text{ - }1) \cdot (N + i \cdot k \cdot N + N) + \text{dip} \cdot (4 \cdot (1 + 3) + 207 + 4 + (S\text{ - }1) \cdot (1 + 4 + 1))$$

arithmetic operations are needed.

The resulting arithmetic operations for three different tetrahedral models are presented in Table 4.1. We can see that both approaches require the same

amount of arithmetic operations. The major time consuming part is the calculation of the $N \times (S-1)$ matrix W and the transfer matrix T, respectively. Since the required arithmetic operations for the calculation of both matrices are the same for hexahedral and tetrahedral models, we receive exactly the same results for hexahedral models. The small difference between both approaches is negligible.

We showed in this chapter, that the calculation of the partial integration approach calculated with transfer matrices is as fast as the adjoint approach presented in Vallaghe et al. [46]. Another important point is which approach will lead to better results with regard to relative difference error and magnitude error. This point will be discussed in the next chapter, where we present different tetrahedral meshes as well as hexahedral meshes to show the resulting error curves.

5 Numerical simulation

To make a clear statement which approach leads to better results, we are now going to show error curves for different tetrahedral and hexahedral meshes for both approaches. The following two error criteria are investigated in the following part of this section.
The first error criteria is the *relative difference error* (RDM). The RDM can be calculated via:

$$RDM \;=\; ||\frac{1}{||V_{ana}||_2}V_{ana} - \frac{1}{||V_{num}||_2}V_{num}||_2$$

with the numerically computed potential V_{num}, the analytically computed potential V_{ana} and the L_2 norm $||.||_2$, presented in Appendix A.2. The lower the difference between the calculated potential V_{num} and the analytical potential V_{ana} is, the better is the presented approach. The best result, we are able to obtain is given by $V_{num} = V_{ana}$. This means, the numerically calculated potential is exactly the same as the analytically computed potential. It is thus the goal, to receive a RDM as close to zero as possible.
The next error criteria is the so called *magnitude error* (MAG). The magnitude error can be calculated as follows:

$$MAG \;=\; \frac{||V_{num}||_2}{||V_{ana}||_2}.$$

Thus, the best MAG we are able to obtain is a MAG of 1.
Since the error curves of both approaches are very similar, we present the results in a special way:
For each of the different meshes we present a figure for the relative difference error and for the magnitude error. Each figure is divided into three subfigures. The top figure shows the results for the adjoint approach, the middle figure the results for the partial integration approach and the bottom figure shows the difference between both approaches. The difference is presented in the following way:

$$Err_{diff} = Err_{adjoint} - Err_{partial}.$$

If we consider the relative difference error, a negative sign of Err_{diff} means, that the error of the adjoint approach is lower than the error of the partial integration approach and vice versa. Since the best MAG we are able to obtain is 1, we are not able to argue in the same way, for example, if the MAG of both approaches is below 1, a negative sign of Err_{diff} would mean, that the MAG of the partial integration approach is nearer to one and if the MAG of both approaches is above 1, a negative sign would mean that the MAG of the adjoint approach is nearer to one.

In the following we distinguish between two grid types. We show results for tetrahedral as well as for hexahedral meshes. In the tetrahedral case we are going to present three models with a different number of grid nodes to show, that the result does not depend on the number of grid nodes. In the hexahedral case we present a regular grid as well as a geometry adapted hexahedral grid model.

5.1 Tetrahedral meshes

In this section, we present three tetrahedral spherical shell models with a different number of grid nodes, radii of 92, 86, 80 and 78mm and anisotropic conductivities. We equally distribute 748 EEG sensors at the surface of the model. In the volume conductor, we place 77 dipoles as a series from the middle of the sphere to the right, starting from coordinates 127-128-127 to 127-204-127, thus the distance between two dipoles is 1mm. On the x-axis the source eccentricities are presented from 0 to 1. The eccentricity has the value zero in the middle of the sphere and increases for each step until the dipole at coordinate 127-204-127. In other words, the eccentricity is given by the percentage of the difference between the source location and the sphere midpoint divided by the radius of the inner shell. The tangential sources are oriented in the $+z$ axis and the radial sources in the $+y$ axis. We set the dipole amplitudes to 1 nAm. In Section 7.2 we use a regular hexahedral head model and a geometry adapted hexahedral head model with the same setting.

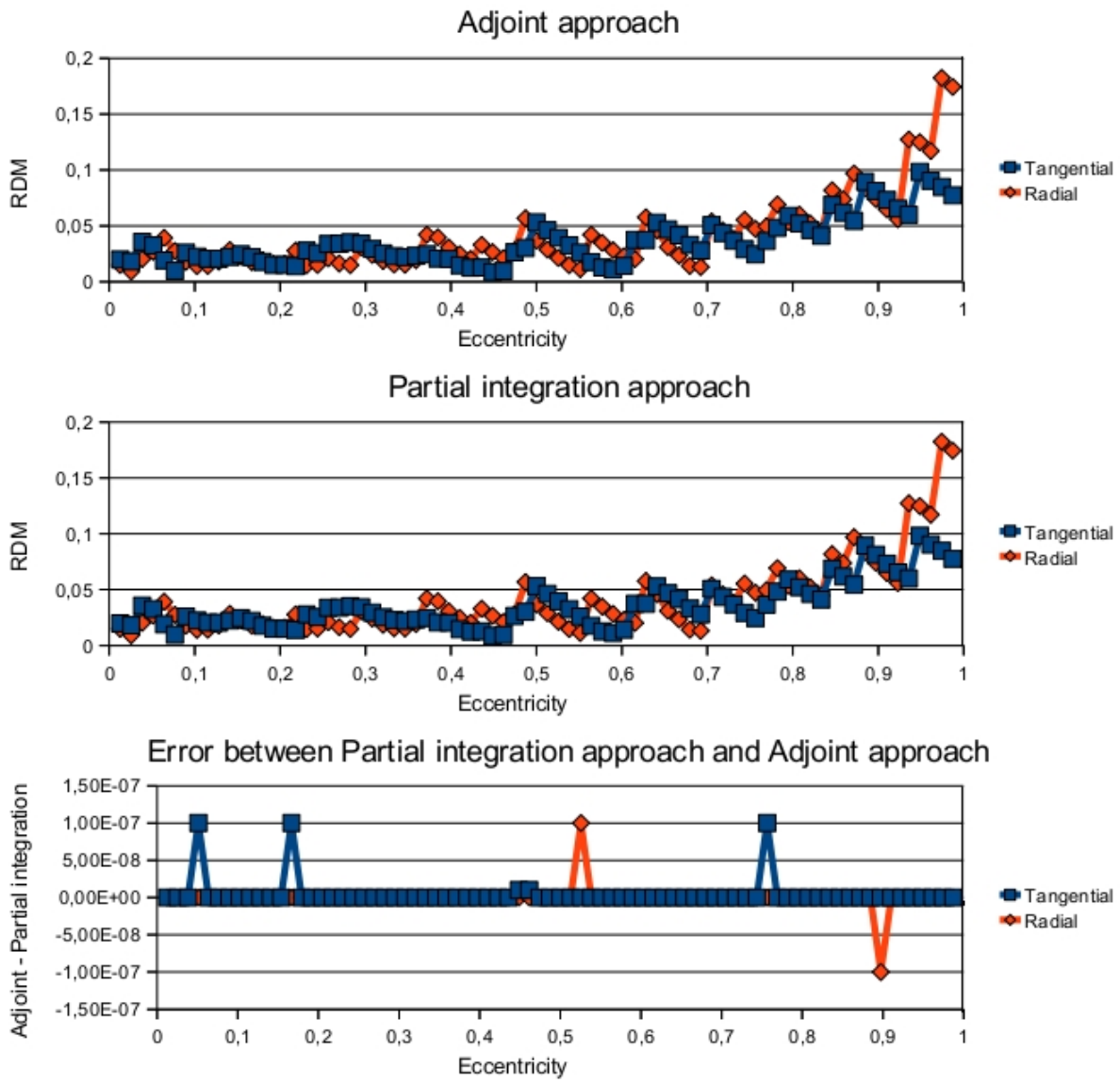

Figure 5.1: RDM for a tetrahedral model with 72k nodes.

The first tetrahedral model we are going to present is a model with 71,896 nodes and 438,013 elements. Figure 5.1 shows the results for the RDM. We can see, that the tendency between both approaches is always the same. The error difference Err_{diff} between the partial integration approach and the adjoint approach is of magnitude 10^{-7} and therefore negligible. There are only 7 eccentricities where we have a difference of 10^{-7}.

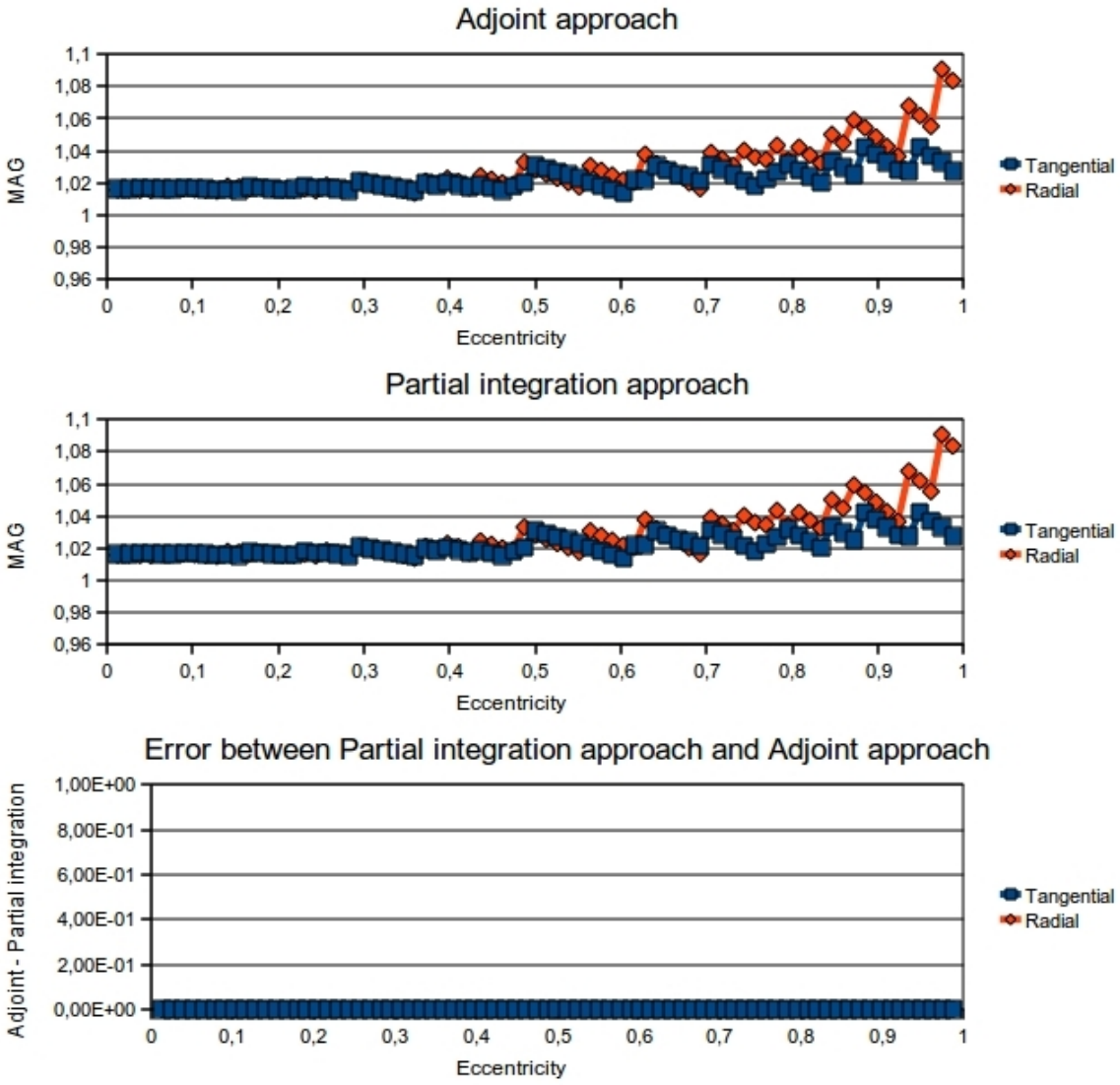

Figure 5.2: MAG for a tetrahedral model with 72k nodes.

In Figure 5.2 the results for the MAG are shown. We can see that the error difference Err_{diff} is zero for each source eccentricity. Thus both approaches attain exactly the same result concerning magnitude error.

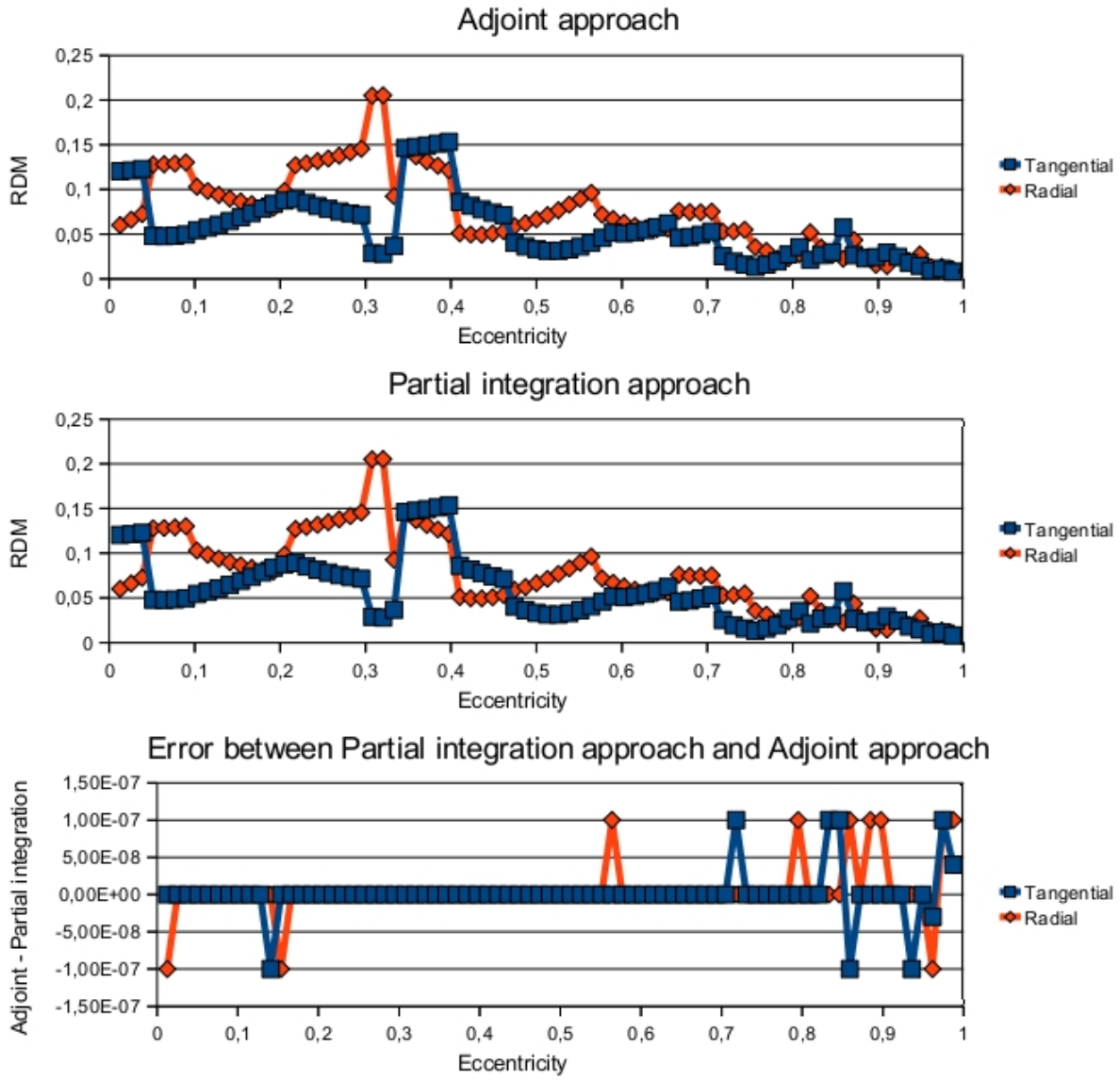

Figure 5.3: RDM for a tetrahedral model with 360k nodes.

As a next model, a tetrahedral model with 360,056 nodes and 2,165,281 elements is used. In Figure 5.3 the results for the RDM are presented. Both approaches attain nearly the same results and the maximal difference Err_{diff} between both approaches is exactly of magnitude 10^{-7}.

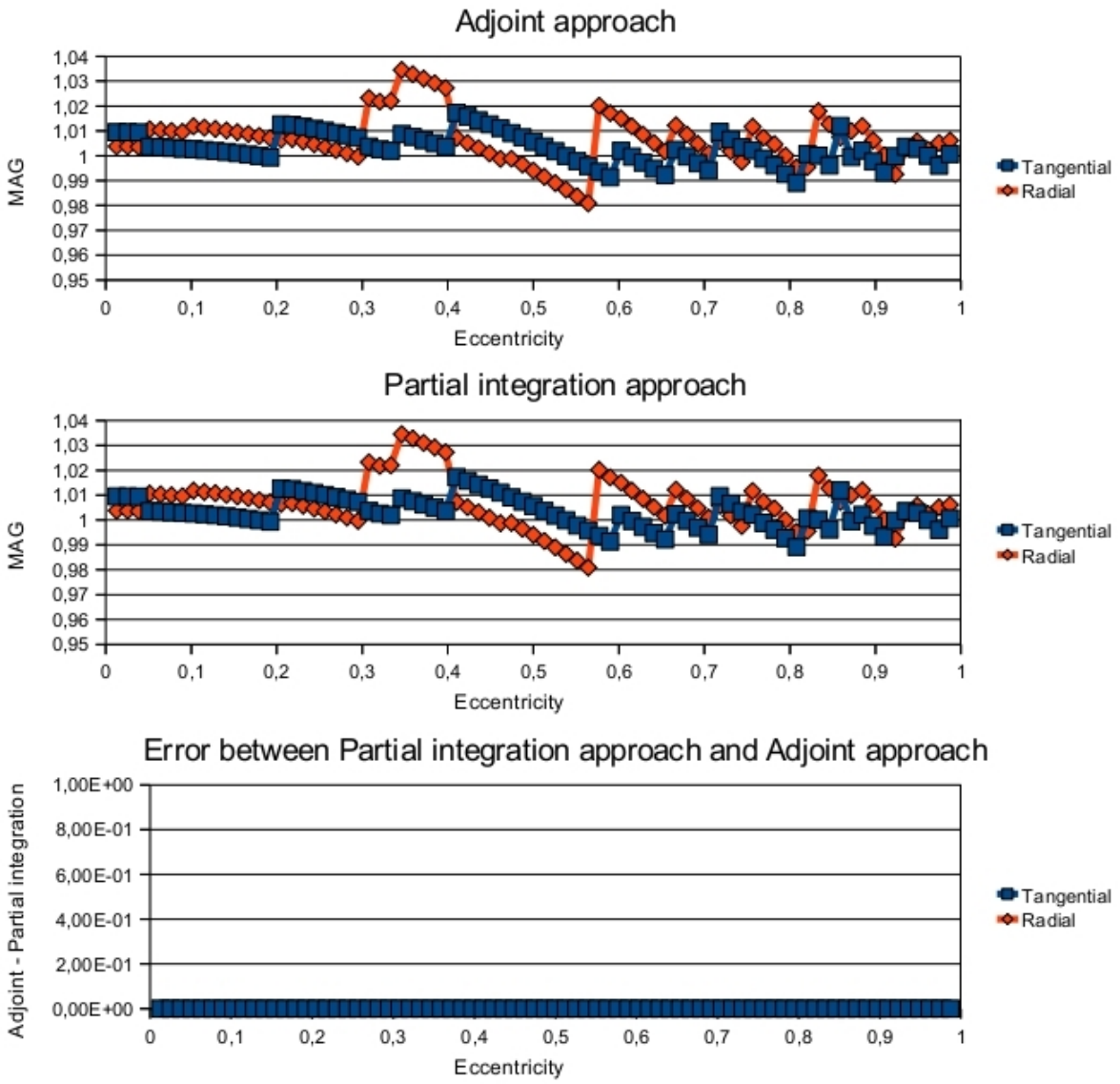

Figure 5.4: MAG for a tetrahedral model with 360k nodes.

The results for the MAG are presented in Figure 5.4. We have $Err_{diff} = 0$ for all source eccentricities.

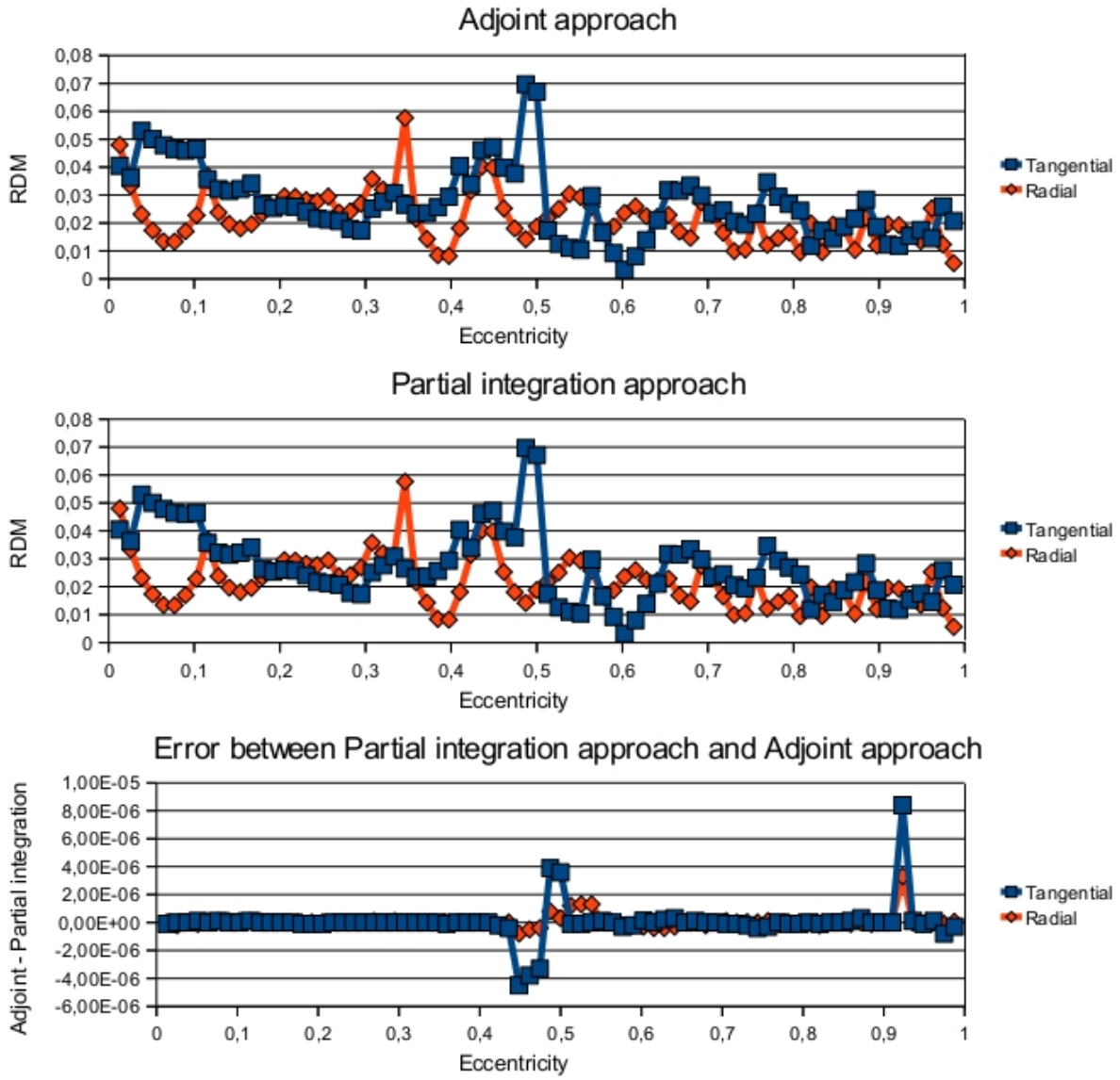

Figure 5.5: RDM for a tetrahedral model with 503k nodes.

The model we are going to use now is the last tetrahedral model in this section for the dipole series from the middle to the right. It has 503,180 nodes and 3,068,958 elements. For source eccentricities between 0.4 and 0.6 there is a small difference in the RDM between both approaches, see Figure 5.5. But the difference is below 10^{-5}. For source eccentricities between 0.4 and 0.5, the difference has a negative sign and between 0.5 and 0.6 is has a positive sign. We are thus not able to make a clear statement, which of the approaches performs better. Additionally, Err_{diff} is not zero near eccentricity 0.9. But the magnitude of the difference is of order 10^{-5}.

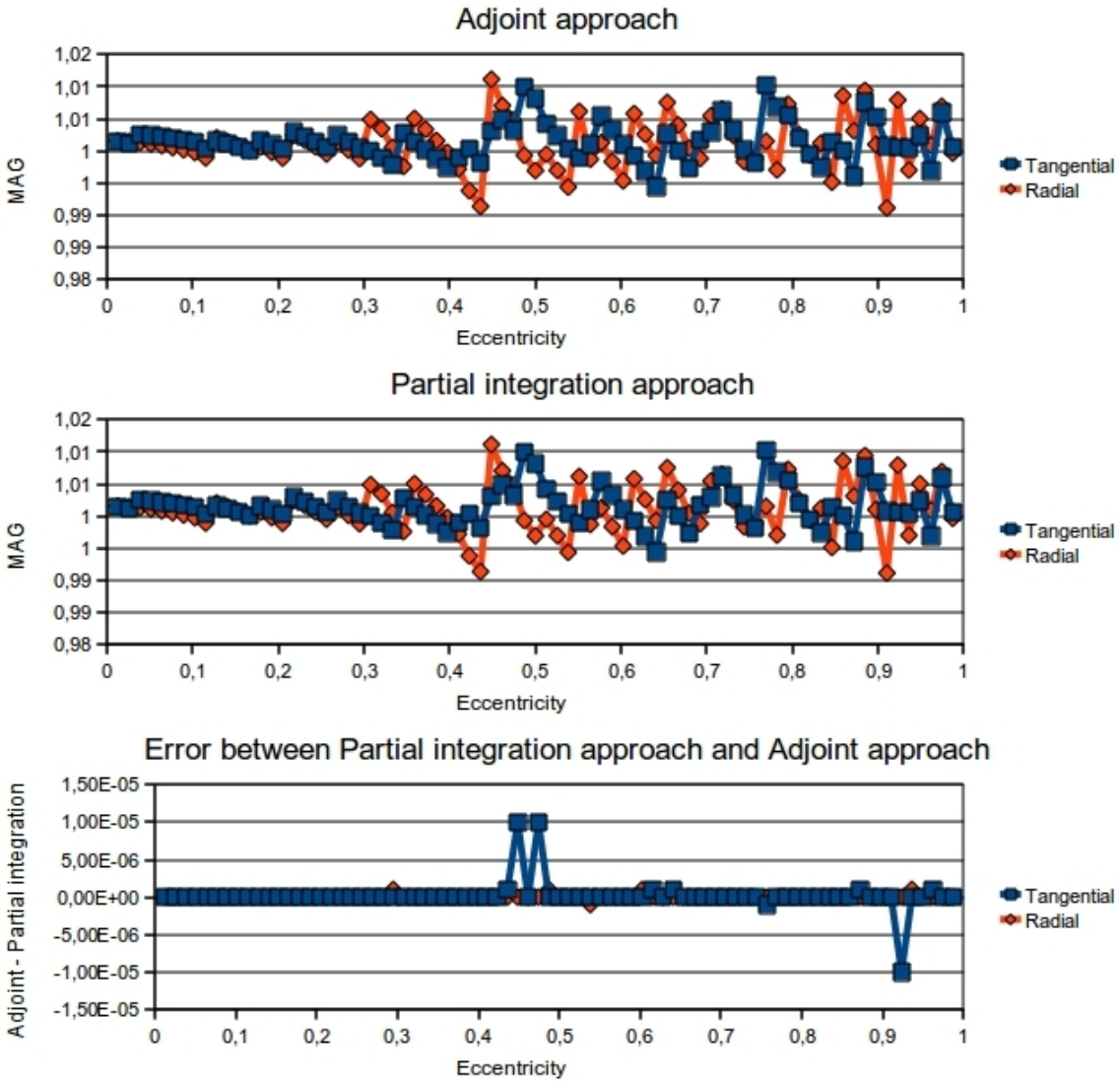

Figure 5.6: MAG for a tetrahedral model with 503k nodes.

For the 503k model, the MAG has the same tendency as the presented RDM. Between source eccentricities 0.4 and 0.6 we have a small difference between the adjoint approach and the partial integration approach of magnitude 10^{-5}, which can be seen in Figure 5.6.
To conclude, for tetrahedral meshes both approaches attain exactly the same results concerning RDM and MAG, independent on the number of grid nodes.

5.2 Hexahedral meshes

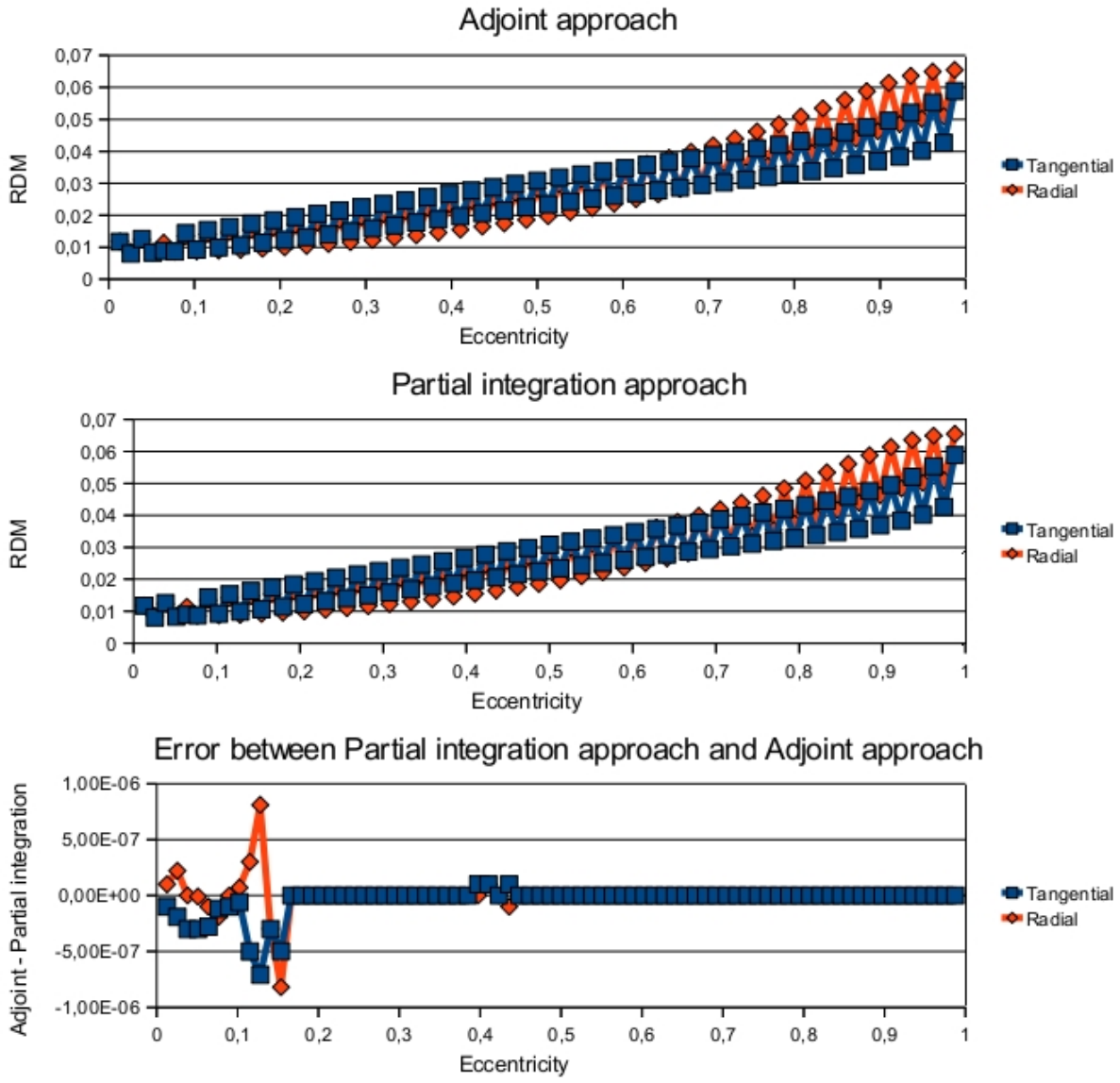

Figure 5.7: RDM for a hexahedral grid model with 425k nodes.

The first model, we are going to use is a regular hexahedral grid model with a side length of 2 mm. This model has 425,631 nodes and 405,545 elements. The RDM of both approaches is nearly the same, see Figure 5.7. The difference between both approaches is of magnitude 10^{-6} and therefore negligible.

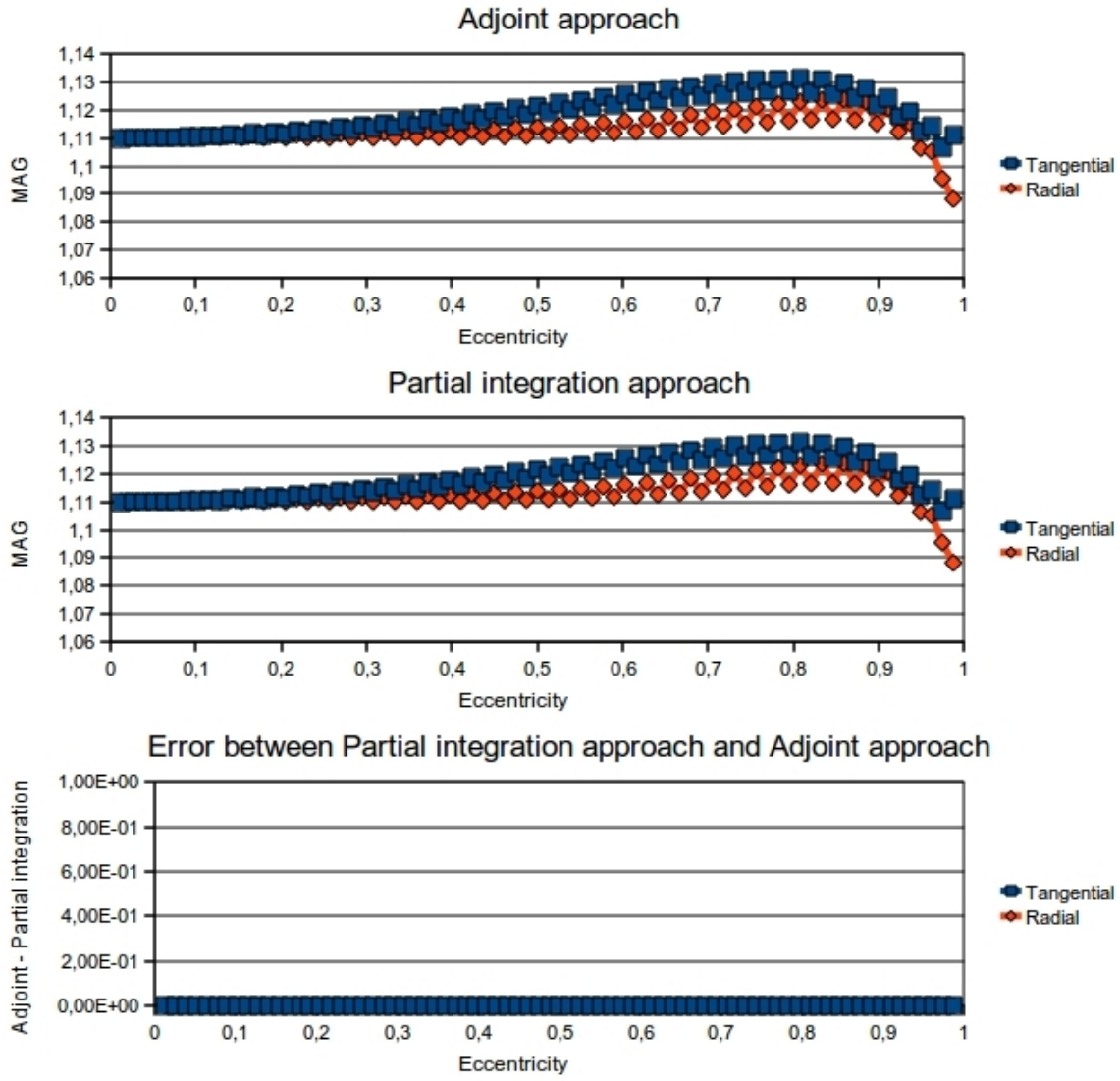

Figure 5.8: MAG for a hexahedral grid model with 425k nodes.

The MAG is exactly the same for each source eccentricity, that is, $Err_{diff} = 0$, see Figure 5.8.

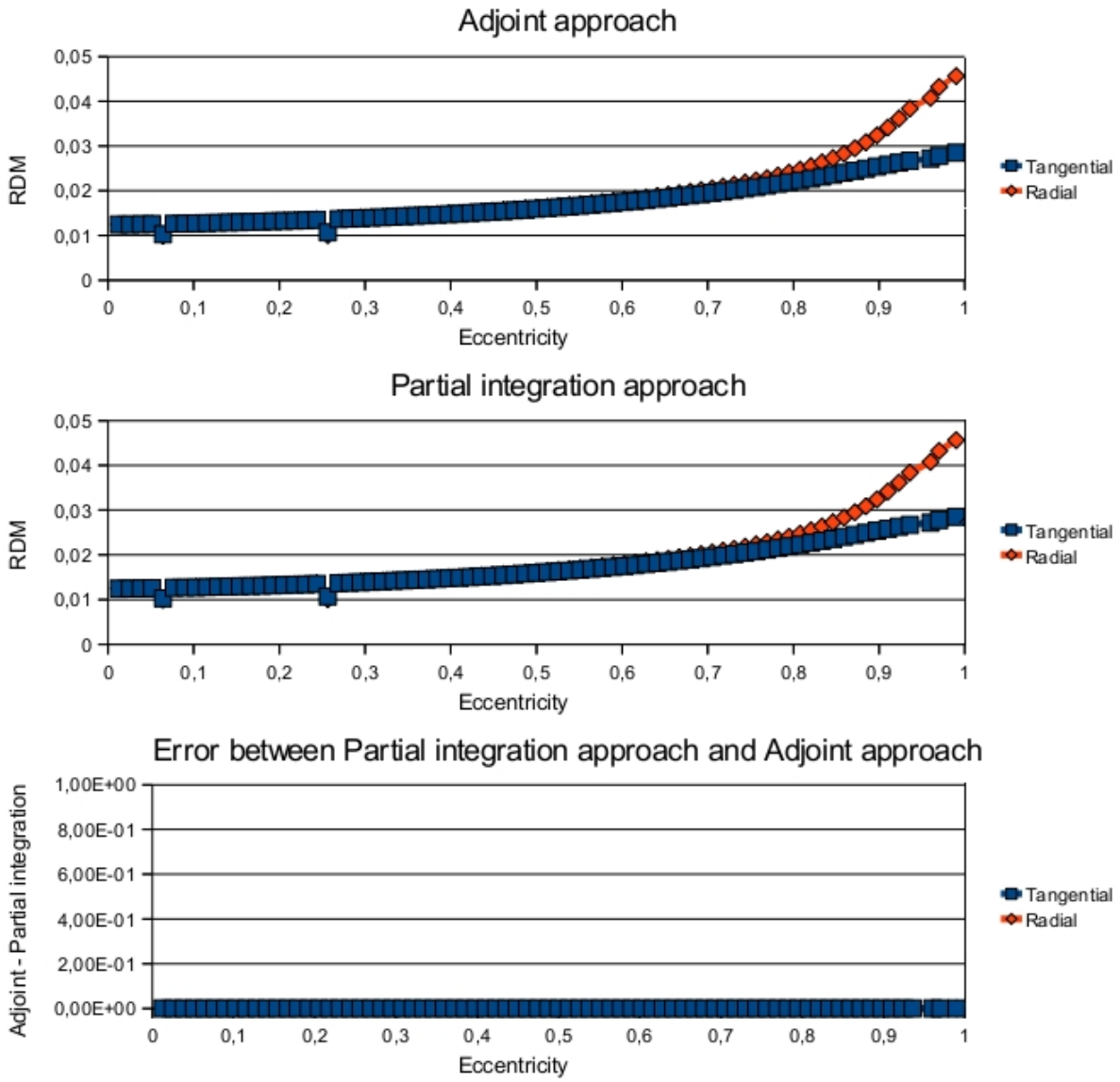

Figure 5.9: RDM for a geometry adapted hexahedral grid model with 3,300k nodes.

The last model, we use in this section is a geometry adapted hexahedral grid model with 3,200k nodes and 3,240k elements.
We do not have a difference between the partial integration approach and the adjoint approach, see Figure 5.9. We have $Err_{diff} = 0$ for all source eccentricities.

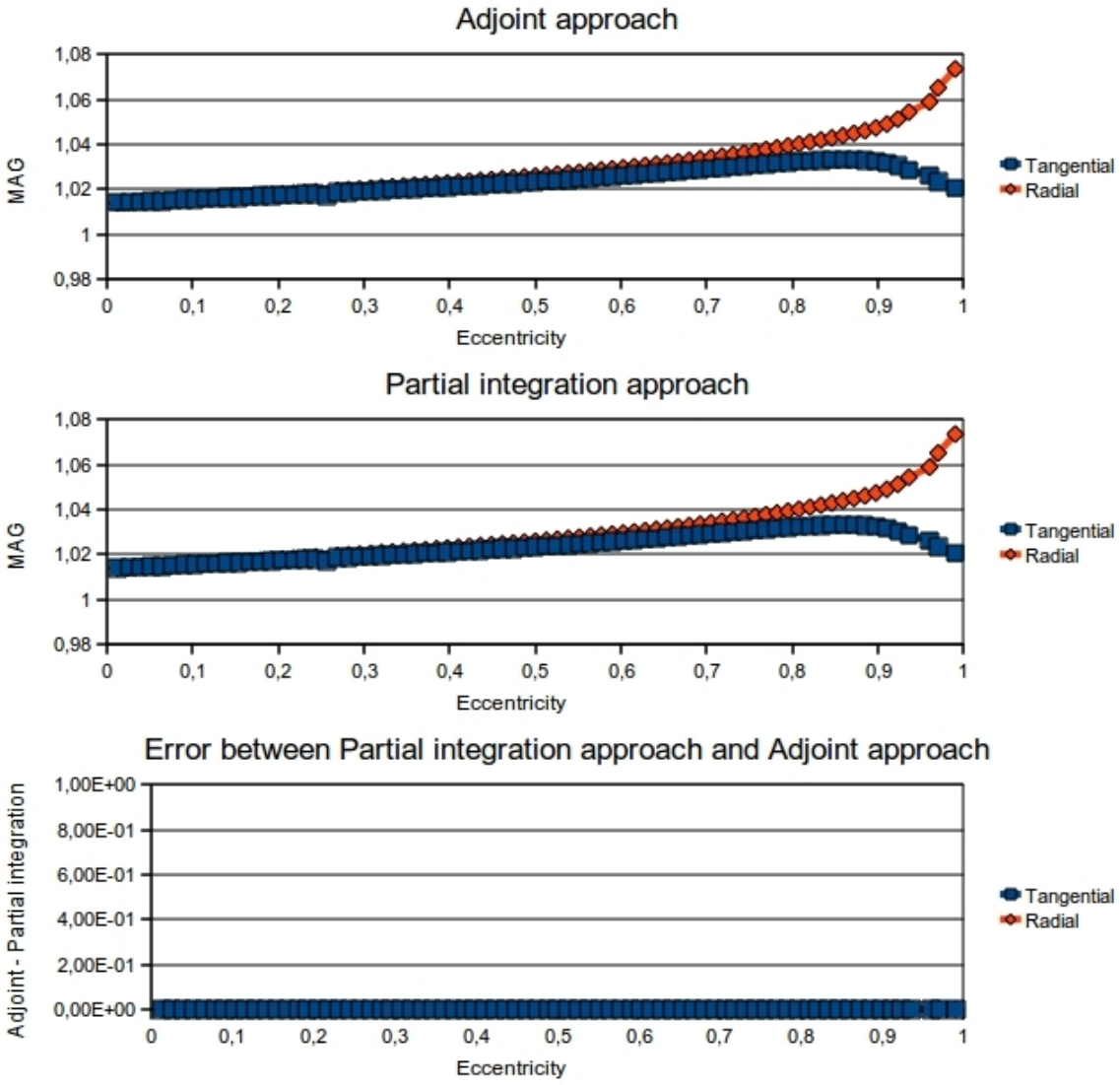

Figure 5.10: MAG for a geometry adapted hexahedral grid model with 3,300k nodes.

The MAG has exactly the same tendency as the RDM, see Figure 5.10. We do not have a difference between both approaches.
Both approaches attain exactly the same results with respect to RDM and MAG. This holds for tetrahedral meshes with a different number of grid nodes as well as for regular and geometry adapted hexahedral meshes.

6 Adjoint approach analytically

Since the RDM and the MAG are nearly identical for both approaches, we compare what the adjoint approach and the partial integration approach calculate analytical.
The adjoint approach calculates analytical:
According to Algorithm 1 let B be the $N \times (S-1)$ matrix summing up the different right-hand sides presented in equation (4.4)

$$B = (b_i)_{i=1,\cdots,N} = \begin{pmatrix} 0 & 0 & 0 & \dots \\ \vdots & \vdots & \vdots & \dots \\ 0 & 0 & 0 & \dots \\ -1 & -1 & -1 & \dots \\ 0 & 0 & 0 & \dots \\ \vdots & \vdots & \vdots & \dots \\ 0 & 0 & 0 & \dots \\ 1 & 0 & 0 & \dots \\ 0 & 0 & 0 & \dots \\ \vdots & \vdots & \vdots & \dots \\ 0 & 0 & 0 & \dots \\ 0 & 1 & 0 & \dots \\ 0 & 0 & 0 & \dots \\ \vdots & \vdots & \vdots & \ddots \end{pmatrix}$$

and i_{ref} the row of B, where the value -1 of the reference electrode is positioned. Let furthermore W be the $N \times (S-1)$ matrix presented in Section 4.3, containing the solutions w of the adjoint partial differential equation. Let us denote $w^i := W_{(\cdot,i)}$ the solution of equation (4.5) for the i-th column of B, that is, the solution of $KW_{(\cdot,i)} = B_{(\cdot,i)}$.
In Algorithm 2 the gradient of the finite element shape functions ϕ_i are calculated. Since the support of ϕ_i is very small, only the gradient of ϕ_i is calculated for the element, which contains the dipole. The gradient of ϕ_i is zero for all other grid nodes. Thus we are able to define a $3 \times N$ matrix $\nabla\Phi(\mathbf{x})$ as

$$\nabla\Phi(\mathbf{x}) = [\nabla\phi_1(\mathbf{x}), \cdots, \nabla\phi_N(\mathbf{x})].$$

The third algorithm is used to calculate the potential difference between each lead. According to equation (4.3) the solution w^i is projected into the finite element space and we obtain

$$\nabla w^i(\mathbf{x}) \approx \sum_{j=1}^{N} \nabla \phi_j(\mathbf{x}) w_j^i = \nabla \Phi(\mathbf{x}) w^i.$$

Following Section 3.3 the potential can be calculated via

$$\begin{aligned}
\tilde{V}_i &= <\mathbf{q}, \sum_{j=1}^{N} \nabla \phi_j(\mathbf{x}_0) w_j^i> = <\mathbf{q}, \nabla \Phi(\mathbf{x}_0) w^i> = <\mathbf{q}, \nabla \Phi(\mathbf{x}_0) K^{-1} B_{(\cdot,i)}> \\
&= (\nabla \Phi(\mathbf{x}_0) K^{-1} B_{(\cdot,i)})^T \mathbf{q} \\
&= (B_{(\cdot,i)})^T (K^{-1})^T (\nabla \Phi(\mathbf{x}_0))^T \mathbf{q} \\
&= (B^T)_{(i,\cdot)} K^{-1} (\nabla \Phi(\mathbf{x}_0))^T \mathbf{q} \\
&:= \tilde{R}_{(i,\cdot)} K^{-1} (\nabla \Phi(\mathbf{x}_0))^T \mathbf{q}
\end{aligned}$$

and the complete potential $\tilde{V}$ is given by

$$\tilde{V} = \tilde{R} \underbrace{K^{-1} (\nabla \Phi(\mathbf{x}_0))^T \mathbf{q}}_{=:U \in \mathbb{R}^n} = \tilde{R} U \tag{6.1}$$

The partial integration approach with transfer matrices is described in Section 4.2 and Section 3.2. The potential V for a dipole at position $\mathbf{x}_0$ with dipole moment $\mathbf{q}$ can be calculated analytically in the following way:

$$V \overset{(4.9)}{=} R K^{-1} b \overset{(3.13)}{=} R K^{-1} \begin{pmatrix} \langle \mathbf{q}, \nabla \phi_1(\mathbf{x}_0) \rangle \\ \vdots \\ \langle \mathbf{q}, \nabla \phi_N(\mathbf{x}_0) \rangle \end{pmatrix} = R K^{-1} \left(\mathbf{q}^T \nabla \Phi(\mathbf{x}_0) \right)^T$$

with the restriction matrix $R \in \mathbb{R}^{(S-1) \times N}$ and the right-hand side vector b presented in equation (3.13). Note that only some entries of b are not zero. To summarize, the partial integration approach with transfer matrices can be calculated analytically:

$$V = R \underbrace{K^{-1} (\nabla \Phi(\mathbf{x}_0))^T \mathbf{q}}_{=:\tilde{U} \in \mathbb{R}^n} = \tilde{R} \tilde{U} = \tilde{R} U + U_{i_{ref}} Id \tag{6.2}$$

The analytical calculation of the adjoint approach and the analytical calculation of the partial integration approach only vary in the $(S-1) \times N$ restriction matrix R and the $(S-1) \times N$ matrix $\tilde{R}$, which is given by the transpose of the right-hand side matrix B. Furthermore, R and $\tilde{R}$ only vary in one column, that is, the column, representing the reference electrode has in the adjoint case

a value of -1 and in the partial integration case a value of zero. Thus the only difference between both approaches is given by the type of referencing, that is, $\tilde{V} = V - U_{i_{ref}} Id$. The small difference in the numerical simulation section originates by the fact that we solve the linear system (4.5) and (4.6) iteratively with a finite precision. Since we have in both cases different right-hand sides, we have slightly different results for the RDM and the MAG.

In Section 3.3 we asked ourselves the question, if a singularity of higher order in the volume conductor or a singularity of lower order on the boundary leads to different results. We showed in Chapter 4 and 5 that both approaches leads to exactly the same results with regard to RDM and MAG and both approaches require the same amount of arithmetic operations. In this chapter we derived closed formulas for the potential computed by both approaches and showed that the formulas are identical.

7 Realistic head model

In this chapter we present the sensitivity distribution for a given lead. According to Malmivuo and Plonsey [29], the lead field describes the sensitivity distribution for a given lead. The notation lead field is used in [29] for the reciprocal current density field J_{LE}, see Section 2.4.3, which can be calculated with the adjoint approach presented in Section 3.3. As discussed in equation (3.18), the lead field for a given lead is exactly given by the gradient of the solution w of the adjoint partial differential equation. Following Section 2.3 the potential difference $\mathbf{U_{ab}}$ caused by a dipole $\mathbf{d}$ between a given lead can be calculated as follows

$$\mathbf{U_{ab}}(\mathbf{d}) = < \mathbf{I_{ab}}, \mathbf{r} >$$

with the lead field $\mathbf{I_{ab}}$ and the dipole orientation vector $\mathbf{r}$. The arrows presented in the following figures show the lead field. If the dipole is oriented parallel to the presented arrows, the potential difference $\mathbf{U_{ab}}(\mathbf{d})$ will be very high. Thus, the figures show how dipoles should be oriented to maximize the potential difference measured between the lead.
We present a realistic head model of a young male patient who suffers from epilepsy due to a brain tumor, for details see Rullmann et al. [39]. A geometry adapted hexahedral head model with 3,020k nodes and 3,098k elements and the conductivities presented in Table 7.1 is used. According to Baumann et

Head compartment	Conductivity
Skin	0.43 S/m
Skull	0.0042 S/m
CSF	1.79 S/m
Gray matter	0.33 S/m anisotropic
White matter	0.142 S/m anisotropic
Lesion	0.33 S/m

Table 7.1: Conductivity values, see Rullmann et al. [39]

al. [3] the conductivity of the CSF is set to 1.79 S/m. A sensor cap with 24 electrode positions is used to investigate the sensitivity distribution for a given lead. Fixing one electrode as reference, this results in 23 leads that can be used to investigate different sensitivity distribution scenarios.

7.1 Sensitivity distribution

The L_2 sensitivity distribution for a given lead is calculated as presented in Algorithm 5.

Algorithm 5 Sensitivity distribution for a given lead

```
for i = 1 to SensorNodes.length() do
  b(SensorNodes[0]) = -1;
  b(SensorNodes[i]) = 1;
  Solve: Kw = b;
  b(SensorNodes[i]) = 0;
  for j = 0 to NumberOfGridElements do
    Find j-th Element;
    for i = 0 to nodespelem do
      locnode[i] = i-th NodeOfDipoleElement;
      coords[i*3 + 0] = x-coordinate;
      coords[i*3 + 1] = y-coordinate;
      coords[i*3 + 2] = z-coordinate;
    end for
    fofagn(Element, Barycentre, locnode, coords, phi-grad);
    for k = 0 to nodespelem do
      sens_x[j] += phi-grad[3*k + 0] * w(locnode[k]);
      sens_y[j] += phi-grad[3*k + 1] * w(locnode[k]);
      sens_z[j] += phi-grad[3*k + 2] * w(locnode[k]);
    end for
  end for
  for j = 0 to NumberOfGridElements do
    sens_l2[j] = (sens_x[j]^2 + sens_y[j]^2 + sens_z[j]^2)^(1/2);
  end for
end for
```

In the adjoint approach the solution matrix W was created as a preparatory

step. This step is not necessary for the calculation of the sensitivity distribution. In each iteration the solution w of the adjoint partial differential equation is calculated, that is, for each given lead. To obtain the L_2 sensitivity for each element, we need a loop over the number of grid elements. In order to use the Fortran routine fofagn, we calculate for each element the corner nodes and the corner coordinates. Vorwerk showed in his diploma thesis [48] that the minimal error is reached in the barycentre of a cube. Thus we choose the barycentre of each element as the evaluation point of fofagn, which gives us the derivative of the finite element shape functions at each corner node with respect to the evaluation point. As a next step each component of $\nabla\phi_i$ is multiplied with the solution w_i of the adjoint partial differential equation. This provides us with the required ∇w at each grid node of that element. To obtain the sensitivity distribution into all three coordinate directions for that element, we have to sum up ∇w at each corner node. This gives us the sensitivity distribution into the direction of the x-,y- and z-axis. The L_2 sensitivity distribution is then given by

$$\tilde{S} = ||\nabla w||_2 = \sqrt{(\nabla w_1)^2 + (\nabla w_2)^2 + (\nabla w_3)^2}$$

with w_i the i-th component of ∇w.

The figures in Section 7.1 and 7.2 are presented in the following way:
Each figure is divided into four subfigures. In Figure 7.1 and 7.2 both subfigures on the left-hand side present the L_2 sensitivity distribution and the two subfigures on the right-hand side present ∇w as a vector field with a distance of 4mm between each vector. The top figures present the L_2 sensitivity and ∇w as a vector field for the same lead and the bottom figures show them for another given lead. To be able to show the vector field, each subfigure shows a plane on which both electrodes are located. The color on the figures on the left-hand side indicate the L_2 sensitivity which is higher for red colored areas and lower for blue colored areas. The bigger the arrows on the right-hand side are the bigger is the sensitivity. In Figure 7.3 and 7.4 the L_2 sensitivity for a head model with CSF compartment on the left-hand side is compared to the L_2 sensitivity for the same head model without CSF compartment on the right-hand side. Again, both top figures and both bottom figures present the results for the same lead. In order to see any difference between both cases, the scale of the L_2 sensitivity is fixed from 0 to 1. In Figure 7.5 and 7.6 the orientation of the vector field ∇w is presented for a head model with CSF compartment on the left-hand side and for the same head model without CSF compartment on the right-hand side. The positions of the EEG electrodes are marked by two gray balls in each figure.

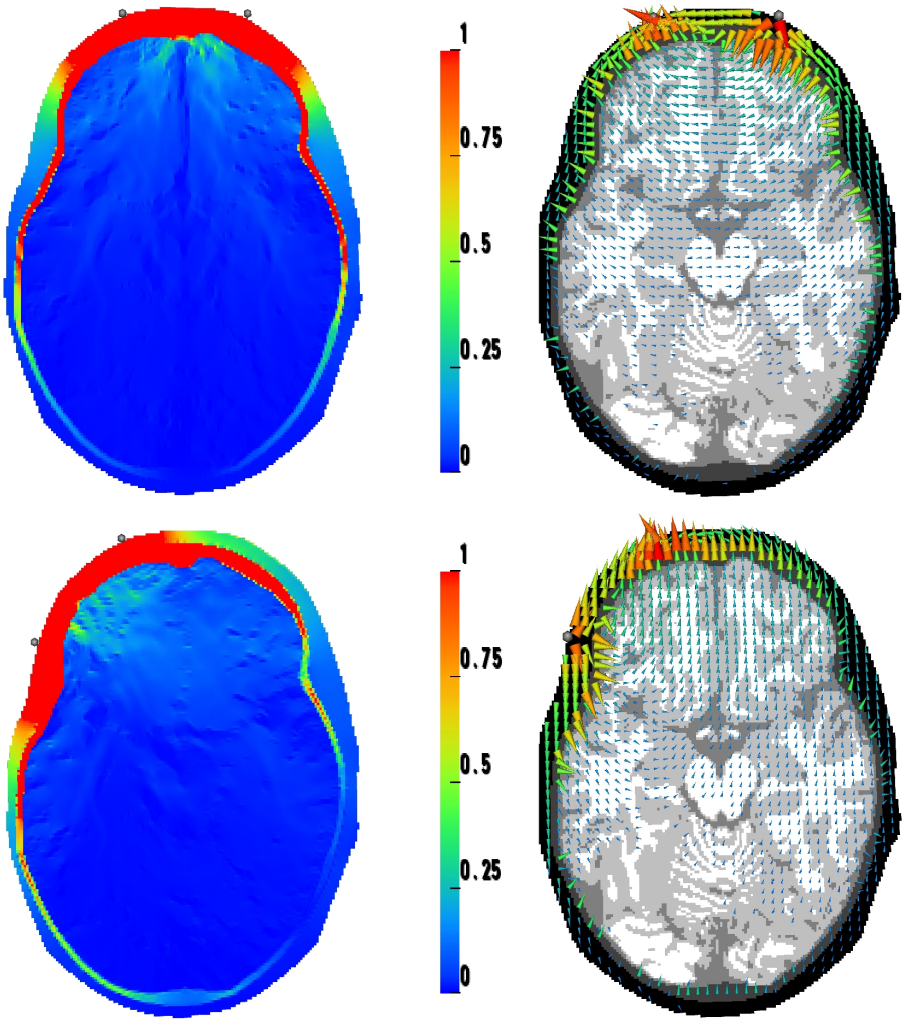

Figure 7.1: L_2 sensitivity distribution (left) and orientation of ∇w (right)

Figure 7.1 shows the sensitivity distribution for two different leads. The L_2 sensitivity is for both leads very high in the scalp compartment and the skull compartment nearby the EEG electrodes. Additionally, the L_2 sensitivity is higher in the brain compartment nearby both electrodes and decreases for areas which are located far away from the electrodes. The L_2 sensitivity in the scalp compartment nearby the EEG electrodes is around 30 compared to a value below 1 in the brain compartment. In order to see any variation of the L_2 sensitivity within the brain compartment, we choose a color scale between 0 and 1. The figures on the right-hand side show the corresponding vector field

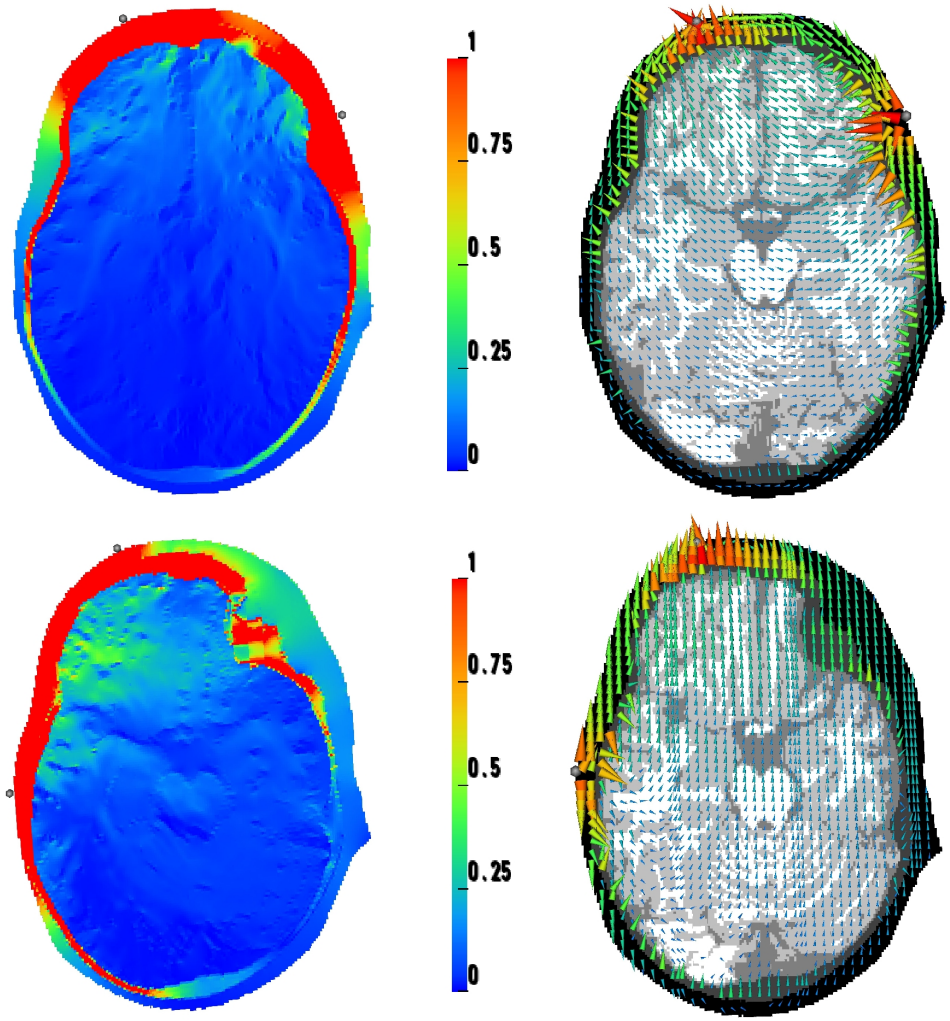

Figure 7.2: L_2 sensitivity distribution (left) and orientation of ∇w (right)

∇w. A unit current is introduced at the scalp electrode and removed at the reference electrode. The arrows are oriented inwards at the scalp electrode and outwards at the reference electrode and flow from the current source to the current sink. Since the gray matter and white matter compartments are modelled anisotropic, some arrows located in that compartments are not exactly flowing from the current source to the current sink. Due to the high conductivity of the CSF compartment, some vectors located in the CSF are also not flowing from the source to the sink.

Another interesting point to mention is the orientation of the vectors located in the skull compartment. Vectors which are located in the skull compartment are radially oriented. It is thus important to choose a radial skull conductivity

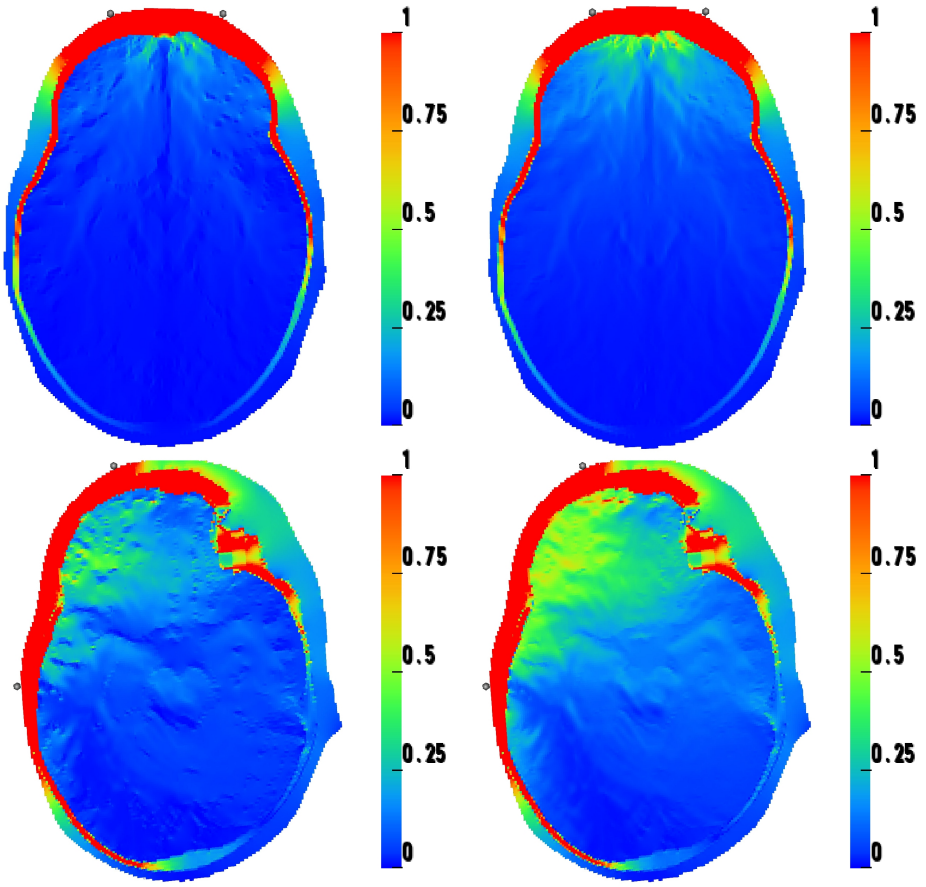

Figure 7.3: L_2 sensitivity distribution with (left) and without (right) CSF compartment

which is as realistic as possible. The tangential conductivity is not so important due to the fact that the vectors are radially oriented. In Figure 7.2 two other leads are presented. We can see that the L_2 sensitivity is also higher in the area nearby both electrodes and decreases for areas which are located far away from the electrodes. Additionally, the sensitivity is higher in the scalp and skull compartments and most vectors are oriented from the source to the sink.

7.2 Sensitivity without CSF compartment

In this section we investigate if the sensitivity distributions change for head models where the CSF compartment is neglected. In that case, we explain how and especially where the sensitivity distributions differ. To be able to investi-

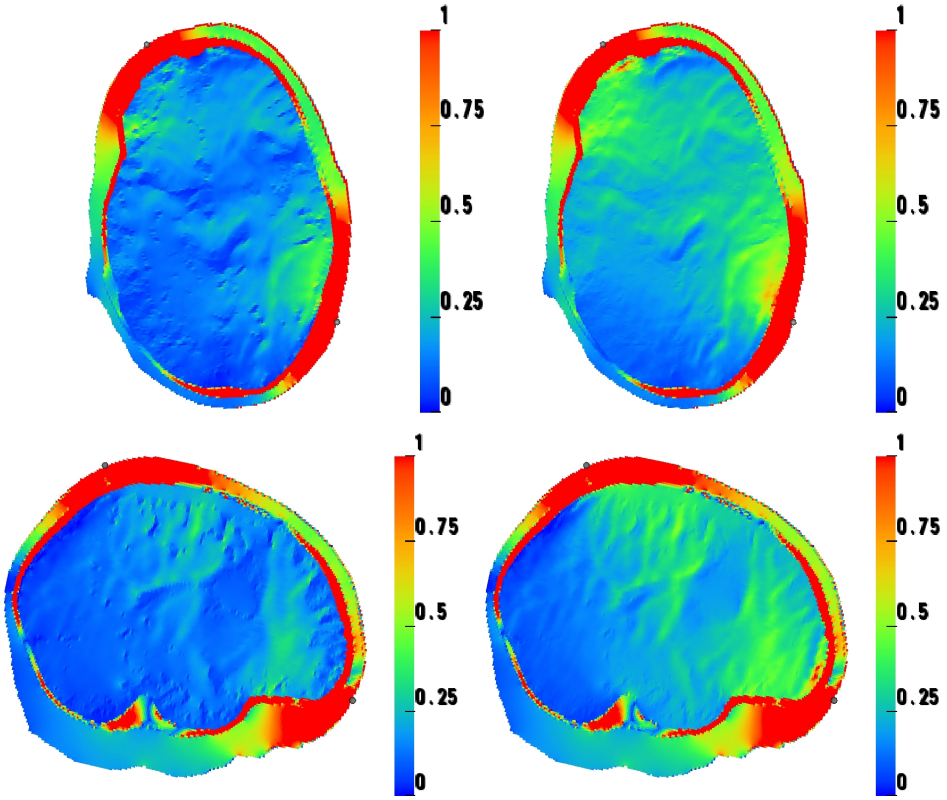

Figure 7.4: L_2 sensitivity distribution with (left) and without (right) CSF compartment

gate that topic a head model with CSF compartment is compared to the same head model without CSF compartment. For the head model without CSF, the conductivity of the CSF compartment is set to 0.33 S/m. For the head model with CSF compartment, the CSF has a conductivity of 1.79 S/m.

If the CSF compartment is neglected, the values of the L_2 sensitivity change. This setting causes an increase of the L_2 sensitivity in the complete brain tissues, see Figure 7.3 and 7.4. This is due to a lower conductivity of the CSF compartment. Thus, the potential caused by a dipole which is located at an arbitrary position within the volume conductor is overestimated compared to the potential caused by a dipole at the same position for the head model separating the CSF and gray matter compartment.

The minimal and maximal values of the L_2 sensitivity within the brain com-

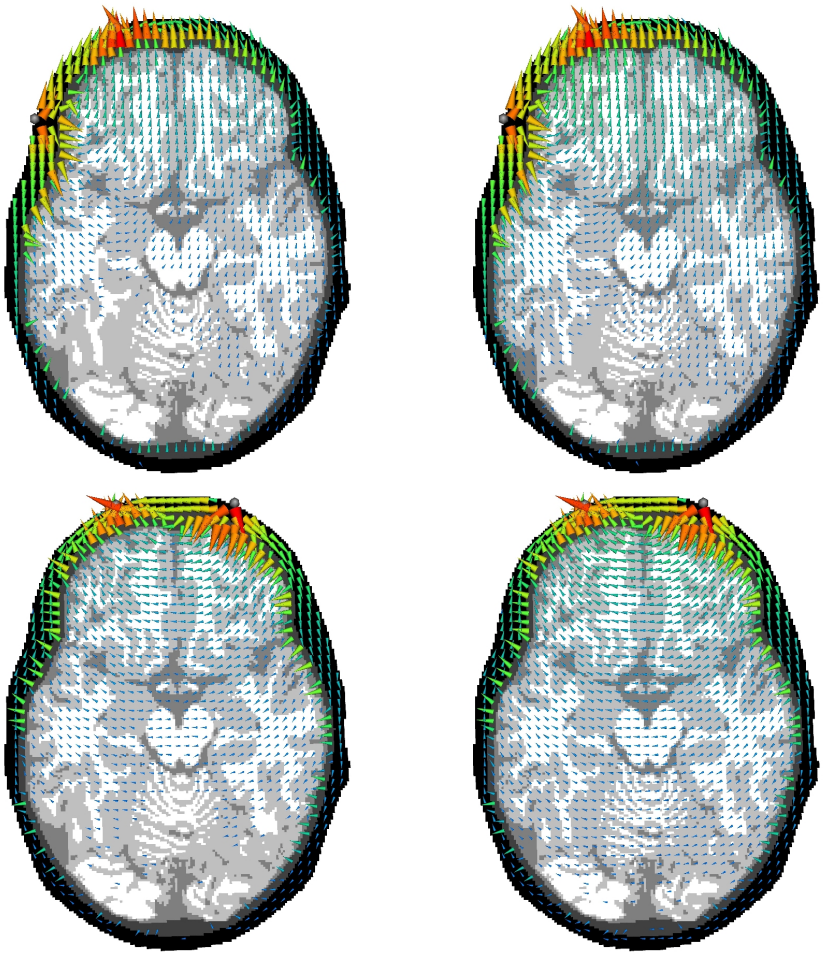

Figure 7.5: Orientation of ∇w with (left) and without (right) CSF compartment

partments are presented in Table 7.2. If the CSF compartment is neglected, the values of the L_2 sensitivity within the brain compartments are higher as compared to the values of the head model, separating the CSF and gray matter compartments. The minimal L_2 value increases between a factor of 2.5 in the third case and a factor of 4.9 in the first case. Furthermore, the maximal L_2 value increases between a factor of 1.4 in the last case and a factor of 2.5 in the third case. Neglecting the CSF compartment cause a higher potential measured at the EEG scalp electrodes due to a higher sensitivity within the complete brain compartments, where the dipolar sources are located.
This is in agreement with Ramon et al. [35]. They showed that the CSF tissue affects the potential measured at the scalp electrodes. Using more realistic head models in EEG forward simulations improves the accuracy of the EEG source localization process and we advice to use head models which are as realistic

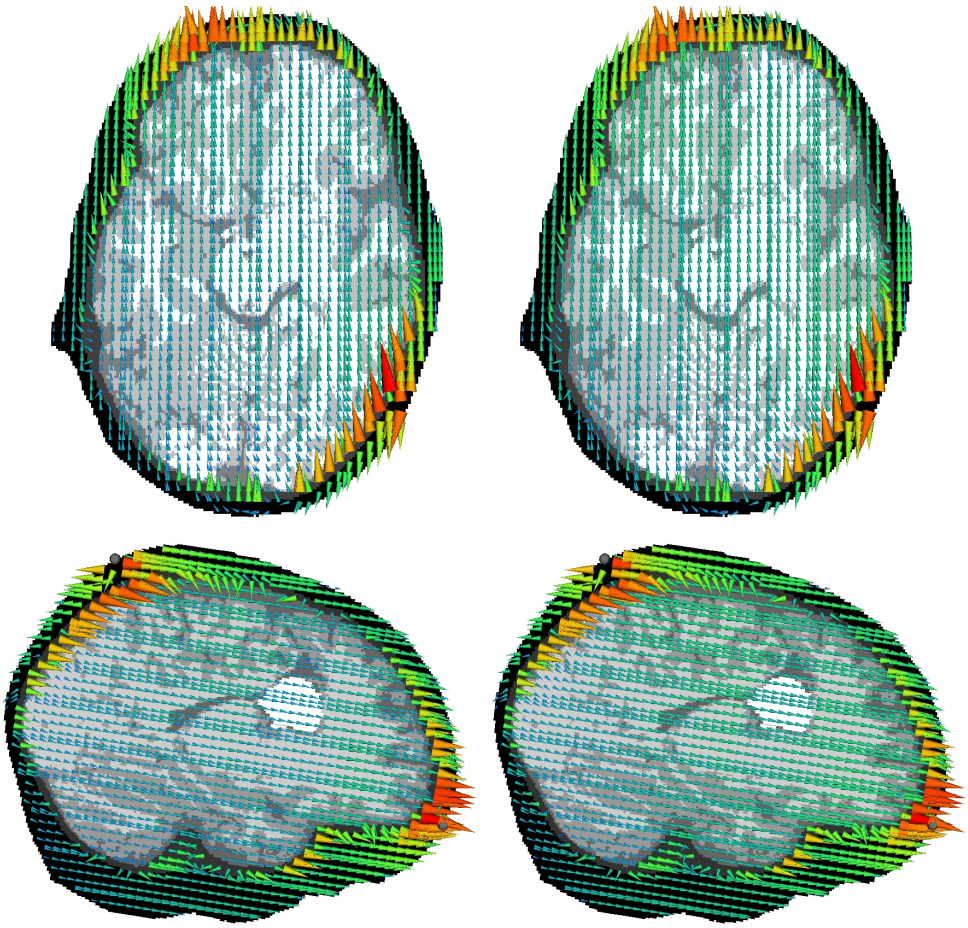

Figure 7.6: Orientation of vector field with (left) and without (right) CSF compartment

as possible. Another interesting point to investigate is the orientation of the vector field ∇w in both figures.

In Figure 7.5 the vector field ∇w is presented for the same EEG electrodes presented in Figure 7.3. If the CSF compartment is neglected, the orientation of the vector field ∇w differs in the CSF compartment. In that case, the vectors are flowing directly from the current source to the current sink. This is due to the fact, that the conductivity of the CSF compartment is set to 0.33 S/m which is exactly the conductivity of the gray matter compartment. The orientation of vectors located in the CSF compartment for the head model separating the CSF and gray matter compartment differs. They are flowing along the CSF due to a higher conductivity. In addition, the arrows of ∇w are slightly bigger,

Figure	WithCSF	WithOutCSF
Figure 7.3 top	0.0011 - 0.49	0.0054 - 0.8
Figure 7.3 bottom	0.0068 - 0.47	0.021 - 0.67
Figure 7.4 top	0.0017 - 0.31	0.0043 - 0.78
Figure 7.4 bottom	0.019 - 0.61	0.065 - 0.86

Table 7.2: Minimal and maximal L_2 sensitivity values for different leads

if the CSF compartment is neglected. This is in agreement with the L_2 sensitivity distribution presented above. The L_2 sensitivity is higher in the complete volume conductor Ω which leads to bigger arrows of the vector field ∇w.

Figure 7.6 presents the vector field ∇w for the same EEG electrodes as presented in Figure 7.4. Furthermore, the orientation of the vector field ∇w and the size of the vectors change. Neglecting the CSF compartment leads to bigger arrows and a slightly different orientation in the CSF compartment of the vector field ∇w. Again, vectors which are located in the skull compartment are radially oriented. This is exactly what we presented in Section 7.1.

Since the L_2 sensitivity distributions differ between the head model with CSF and the same head model without CSF, we want to show some detailed figures in areas, where the sensitivity distributions differ most. The figures show the same electrode positions as presented in Figure 7.1. The top figure shows the electrode, where the current is introduced and the bottom figure the reference electrode, where the current sink is located. We use a head model with CSF compartment on the left-hand side and the same head model without CSF on the right-hand side (Conductivity of the CSF is set to 0.33 S/m).

The orientation between the arrows on the left-hand side and the arrows on the right-hand side differs. The orientation of some vectors located in the brain compartments completely differs between both settings. For example the orientation of vectors located in the mid part of the top figures are completely different. Additionally, we can see that the vectors are pointing inwards at the EEG electrode and outwards at the reference electrode and neglecting the CSF compartment leads to bigger arrows of the vector field ∇w. The bottom figure shows another area, where the sensitivity distribution differs. Again, we have

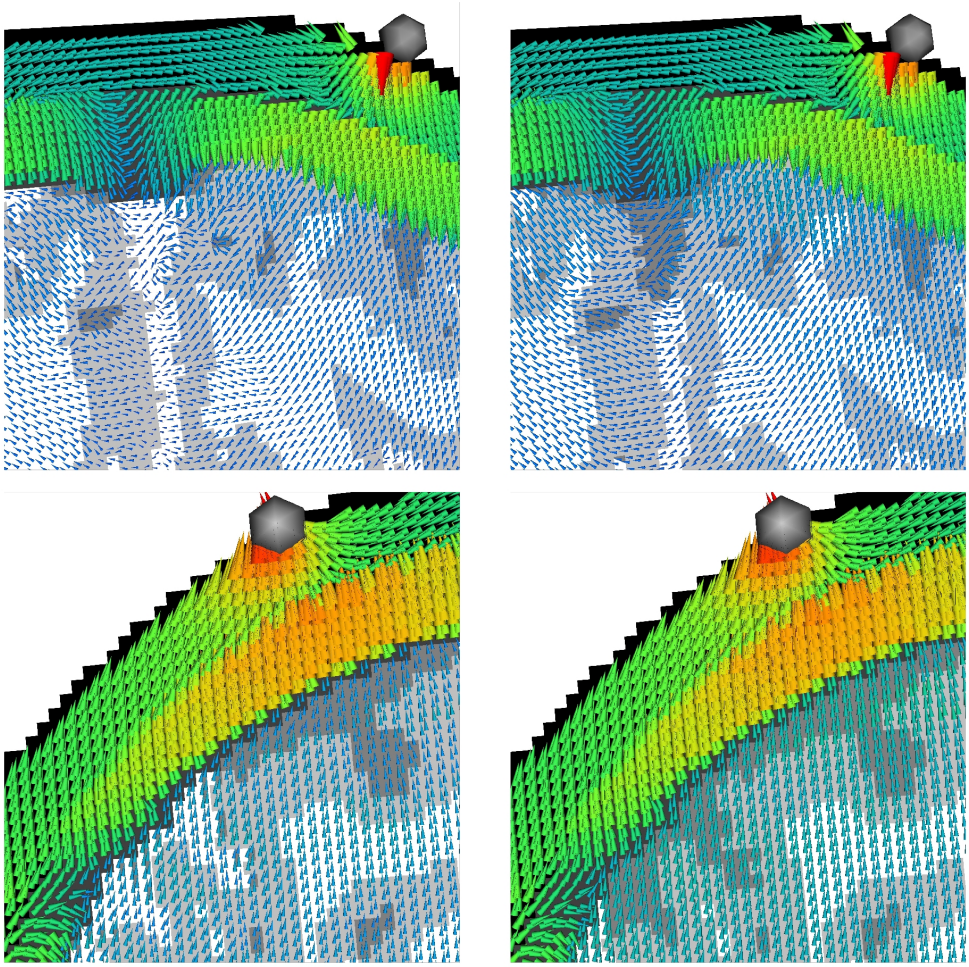

Figure 7.7: Zoom into Figure 7.1 with (left) and without (right) CSF compartment. The distance between each vector is 1mm.

a different orientation of some vectors located in the brain compartments and a higher magnitude of the arrows in the brain compartments.

8 Summary and conclusion

8.1 Summary

The main results of this thesis are:
We developed an algorithm for the adjoint approach. The calculation of the desired potential difference between each lead is divided into three subalgorithms. For more details we refer to Chapter 4.
The next step was the implementation of the adjoint approach into SimBio (see [44]) with linear finite element basis functions. We implemented the adjoint approach for tetrahedral and hexahedral finite element models. It is now possible to use regular cubes as well as geometry adapted hexahedral elements, see, for example, Wolters [53].
After the implementation, the adjoint approach is validated for three tetrahedral and two hexahedreal finite element models in a 4-layer sphere model. In the hexahedral case a regular hexahedral grid and a geometry adapted hexahedral grid are used. The RDM and MAG of the adjoint approach were compared to the RDM and MAG of the partial integration approach.
Since both approaches lead to exactly the same results, we compared the arithmetic operations of both approaches. To do so another approach to calculate the right-hand side vector b for the partial integration approach was implemented. In the old implementation the right-hand side vector b was calculated using the FEM Software library COLSAMM (see Wolters [54]). We used Fortran routines implemented in SimBio to replace the calculation with COLSAMM. The partial integration approach is now working without COLSAMM.
We derived closed formulas for the potential computed by both approaches and showed that the formulas are identical.
Since the adjoint approach can be used to calculate the lead field, which is exactly the sensitivity distribution for a given lead, we calculated and visualized the L_2 sensitivity distribution for a given lead. The algorithms are developed and described in Chapter 7. Furthermore, we showed that the L_2 sensitivity increases in the complete brain, if a head model without CSF compartment is used and showed that the orientation of the lead field differs in that case.

8.2 Conclusion

Following the numerical simulation chapter we can see that the partial integration approach delivers exactly the same results with respect to RDM and MAG as the presented adjoint approach. For tetrahedral meshes the maximal difference measured by the RDM between both approaches is of magnitude 10^{-5} and the maximal difference measured by the MAG is of magnitude 10^{-5}. For hexahedral meshes the maximal difference measured by the RDM is of magnitude 10^{-6} and measured by the MAG of magnitude 10^{-7}. In the presented Figures 5.1 - 5.10 we can see that the tendency in the error curves for the RDM and MAG between both approaches is exactly the same. Additionally, we showed that both approaches require the same amount of arithmetic operations.

Vallaghe et al. stated in their work [46] that the adjoint approach keeps the original continuous space whereas the transfer matrix approach uses a discretized space. This statement is not correct. In the adjoint approach only the volume conductor and the sensor configuration are fixed. The source grid is not fixed. We are able to calculate for each possible point within the volume conductor the corresponding potential difference. But the same result holds for the transfer matrix approach. Only the volume conductor and the sensor configuration are fixed and not the source configuration.

We showed in this thesis that the adjoint approach does not have the advantage proposed in [46]. The partial integration approach with transfer matrices attains exactly the same results and needs exactly the same amount of arithmetic operations. Furthermore, we showed that both approaches use a continuous space and explained in Chapter 6 that both approaches analytically calculate the same.

However, the adjoint approach is a tool that can be used to investigate topics related to sensitivity distribution and EEG sensor sensitivity for a given dipole within the volume conductor, see Chapter 7. This might be of practical interest. We showed in Chapter 7 that the CSF compartment affects the measured potential at the scalp electrode.

9 Outlook

With regard to the adjoint approach, there are many interesting further topics to investigate:

We want to investigate second and third order shape functions due to the fact that we do not have a resolution in the element, which contains the dipole if we use linear shape functions. The derivative of second and third order shape functions is not constant, it is linear for second order and quadratic for third order shape functions. For the evaluation of $\nabla\phi$ at the dipole position, we have to implement a function, which determines the correct local dipole position within the element. In addition, a big advantage of higher order shape functions is that the shape of the head domain Ω can be approximated more accurately and appropriately. In SimBio, second and third order shape functions are implemented, we only have to adapt those implementations to our needs.

With regard to the work of Lew et al. [27], we want to compare the partial integration approach with the newly implemented second and third order shape functions to the full subtraction approach and the Venant approach, presented in [27]. We want to investigate the maximal RDM and the maximal MAG between those approaches. Hopefully, the oscillations with the new implementations are eliminated.

The adjoint approach gives us the possibility to investigate different topics related to the sensitivity distribution. After the measurement of a tactile stimuli, a dipole fit can be used to place a dipole in the volume conductor which describes the measured stimuli. The adjoint approach can be used to examine, which EEG electrodes are very sensitive for such a dipole. We select the electrodes with a very high sensitivity and investigate, if the location of the dipole changes, if we only use the selected electrodes for a completely new dipole fit. Another interesting case to investigate is how many electrodes are sensitive for dipoles which are located near the surface and for dipoles which are located in

the lower parts of the human brain.
This concept might be used to investigate and develop completely new electrode configurations, which are sensitive for dipoles in a certain region of interest.

With regard to the work of Haueisen et al. [23] we want to compare the L_2 sensitivity of a head model with isotropic white and gray matter compartments to the same head model with anisotropic white and gray matter compartments. Additionally, we want to the present the vector field ∇w to investigate, if the orientation of the arrows in the gray matter and white matter compartments differs between both settings. Haueisen et al. [23] showed that the magnitude of the potential is higher if anisotropic conductivities are used compared to isotropic ones.

In Chapter 7 we showed that the vectors in the skull compartment are radially oriented. With regard to the work of Dannhauer et al. [13] we want to investigate the orientation of the vector field ∇w for a head model with three-layered skull compartment and present different sensitivity distribution scenarios.

A Appendix

A.1 Mathematical background

Let us first start with a short introduction to functional analysis. It is necessary to introduce a *Banach space*, a *dual space* of a Banach space and a corresponding linear functional. Then, we present Riesz representation theorem.
To introduce a Banach space, we need some groundwork.

Definition 4. *(Vector space, see: [25], page 79) Let $x, y \in X$ and $\alpha, \beta \in \mathbb{R}$. Then X is called a vector space, if $\alpha x + \beta y \in X$*

We are able to define a *norm* in a vector space. It is a function, which allocates for each element in a vector space a non negative value. Furthermore, a norm fulfills other conditions like the triangle inequality.

Definition 5. *(Norm, see: [25], page 81) A function $||.|| : X \to \mathbb{R}$ is called norm on X if we have for all $x, y \in X$ and $\lambda \in \mathbb{R}$*

1. *$||x|| \geq 0$ and $||x|| = 0 \Leftrightarrow x = 0$*
2. *$||\lambda x|| = |\lambda| ||x||$*
3. *$||x + y|| \leq ||x|| + ||y||$*

In the next definition, we define a *normed space*, which is a vector space equipped with a norm.

Definition 6. *(Normed space, see: [25], page 84) Let X be a vector space with corresponding norm $||.|| : X \to \mathbb{R}$. The pair $(X, ||.||)$ is called normed space.*

We are now able to introduce a Banach space. It is a special form of a normed space which fulfills *Cauchy's condition*.

Definition 7. *(Cauchy's condition, Banach space, see: [25], page 89) Let (x_i) be a sequence in a normed space $(X, ||.||)$. The sequence (x_i) is called convergent, if there exists an element $x_0 \in X$ such that*

$$||x_i - x_0|| \to 0 \quad for\ i \to \infty.$$

The sequence (x_i) is called Cauchy sequence, if there exists for every $\epsilon > 0$ an index $N(\epsilon) \in \mathbb{N}$ such that

$$||x_n - x_m|| < \epsilon \; for \; n, m \geq N(\epsilon).$$

A normed space $(X, ||.||)$ is called Banach space, if every Cauchy sequence is convergent.

One of the major points of this section is the definition of a *Hilbert space H*. To do so, we first introduce an *inner product*.

Definition 8. *(Inner product, see: [50], page 201) Let X be a $\mathbb{R}$ vector space. A map $< .,. > : X \times X \rightarrow \mathbb{R}$ is called an inner product if we have for all $x, y, x_1, x_2 \in X$ and for all $\lambda \in \mathbb{R}$*

1. $< x_1 + x_2, y > = < x_1, y > + < x_2, y >$
2. $< \lambda x, y > = \lambda < x, y >$
3. $< x, y > = < y, x >$
4. $< x, x > \geq 0$
5. $< x, x > = 0 \Leftrightarrow x = 0$

We are now able to use the former discussed points to introduce a Hilbert space H.

Definition 9. *(Hilbert space, see: [50], page 202) A Hilbert space H is a Banach space X whose norm is generated by an inner product such that*

$$||x|| = \sqrt{< x, x >}.$$

For the adjoint approach presented in Section 3.3 we have to introduce a *linear functional*.

Definition 10. *(Linear functional, see: [50], page 45) Let X be a normed space. A linear functional A is a map $A : X \rightarrow \mathbb{R}$, which fulfills for all $x, y \in X$ and all $\lambda \in \mathbb{R}$*

$$A(x + y) = A(x) + A(y)$$
$$A(\lambda x) = \lambda A(x)$$

A linear functional maps from a normed space into a field, in our case into the field $\mathbb{R}$. If we want to introduce Riesz representation theorem, the *dual space* of a normed space is needed.

Definition 11. *(Dual space, see: [50], page 58) Let X be a normed space. The space X' of all continuous linear functionals on the normed space X is called the dual space of X.*

The next theorem gives us an impression under which condition the dual space is also a normed space.

Theorem 3. *(Dual space conditions, see: [50], page 59) Let A be a continuous linear functional and X be a normed space with corresponding dual space X'. With*

$$||A||_{X'} = \sup_{x \in X - \{0\}} \frac{|A(x)|}{||x||} = \sup_{x \in X, ||x|| \leq 1} |A(x)|$$

the dual space X' is also a normed space. If X is a Banach space than X' is also a Banach space. The same condition holds if X is a Hilbert space.

We want to present *Riesz representation theorem* invented by Riesz in the year 1907 [36].

Theorem 4. *(Riesz representation theorem, see: [50], page 226) Let H be a Hilbert space. For each linear functional A there exists an unique element $x \in H$ such that the following equation holds*

$$A(y) = < x, y > \qquad \forall\, y \ \in H$$

Proof. See: [50], page 226 Theorem V. 3.6 □

Riesz representation theorem is a very powerful tool. It can be used to calculate the lead field for a given measurement, which is explained in the following

Example 2. *(Vallaghe et al. [46]) The electric potential V in the partial differential equation for the EEG forward problem is linear with regard to the primary current $\boldsymbol{J}^p$. Since V is linear, we are able to set up a linear operator L, which describes the mapping of the primary current $\boldsymbol{J}^p$ on the EEG electrodes, L is the lead field. If we restrict the lead field L to a given sensor, we obtain a linear functional.*
We are then able to calculate the lead field L_{i0} for a lead positioned at $\boldsymbol{r}_i$ and $\boldsymbol{r}_0$ using Riesz representation theorem

$$V(\boldsymbol{r}_i) - V(\boldsymbol{r}_0) = \int_\Omega < L_{i0}(\boldsymbol{x}), \boldsymbol{J}^p(\boldsymbol{x}) > \ dx,$$

with the potential difference $V(\boldsymbol{r}_i) - V(\boldsymbol{r}_0)$ measured between the lead.

A.2 Sobolev theory and Lebesque theory

In this section, we develop the so called *Sobolev spaces* $W_p^k(\Omega)$. Sobolev spaces are important for the theory of partial differential equations and especially for the finite element method discussed in Chapter 4. To introduce Sobolev spaces, we first give a short overview of the so called *Lebesque integration theory.* Then, we introduce the concept of *weak derivative* of a function, which gives us the possibility to define Sobolev spaces.
This introduction follows the book *The Mathematical Theory of Finite Element Methods* by S. C. Brenner and L. R. Scott [8], where further details can be found.
We restrict ourselves in the following to an open or closed subsets of $\mathbb{R}^n$, with non empty interior, which is *Lebesque measurable.*

In the next definition, we want to introduce the so called *Lebesque norm.*

Definition 12 (Lebesque norm and Lebesque space)**.** *Let $1 \leq p < \infty$. The Lebesque norm is defined by*

$$||f||_p := ||f||_{L^p(\Omega)} := (\int_\Omega |f(x)|^p \, dr)^{\frac{1}{p}}.$$

In the case $p = \infty$, we define

$$||f||_\infty := ||f||_{L^\infty(\Omega)} := ess\ sup\{|f(x)| \mid x \in \Omega\}.$$

In both cases, we are able to define the Lebesque spaces by

$$L^p(\Omega) := \{f \in \mathbb{R} \mid ||f||_{L^p(\Omega)} < \infty\}. \tag{A.1}$$

One of the main results obtained in the Lebesque integration theory is shown in the following

Theorem 5. *$L^p(\Omega)$ is a Banach space for all $1 \leq p \leq \infty$.*

Proof. See: [8], page 25. □

The Lebesque space $L^2(\Omega)$ is under the following condition a Hilbert space.

Theorem 6 ($L^2(\Omega)$ Hilbert space, see [16], page 73, Korollar (4.18))**.** *The Lebesque space $L^2(\Omega)$ equipped with the inner product*

$$< u, v > = \int_\Omega u(x)v(x) \, dx$$

is a Hilbert space.

In the next part of this section, we introduce the concept of weak derivative. To do so, we have to introduce some special spaces. The first space we present is the space of all continuous functions with compact support

$$C_0^\infty(\Omega) := \{\phi \in C^\infty(\Omega) \mid supp(\phi) \subset \Omega \; is \; compact\}.$$

The support of the function ϕ is defined in the following fashion

$$supp(\phi) := \overline{\{x \in \Omega \mid \phi(x) \neq 0\}}.$$

The next set we introduce is the space of *locally integrable* functions. This set is needed for the definition of the weak derivative. It is defined by

$$L^1_{loc}(\Omega) := \{f \mid f \in L^1(K) \quad \forall K \in int(\Omega)\}.$$

Due to the fact, that we will investigate partial derivatives, we have to introduce the so called *multi-index* notation. It is defined by

$$\alpha = (\alpha_1, \cdots, \alpha_n) \quad \alpha_i \geq 0 \; \forall \; i$$

and the length of the multi-index α can be calculated via

$$|\alpha| \; := \; \sum_{i=1}^{n} \alpha_i.$$

For $\phi \in C^\infty$, we define the derivative of the *order* $|\alpha|$ by

$$D^\alpha \phi = (\frac{\partial}{\partial x_1})^{\alpha_1} \cdot (\frac{\partial}{\partial x_2})^{\alpha_2} \cdot \cdots \cdot (\frac{\partial}{\partial x_n})^{\alpha_n} \phi$$

and for a given vector $x = (x_1, \cdots, x_n)$, we define

$$x^\alpha := x_1^{\alpha_1} \cdot x_2^{\alpha_2} \cdots x_n^{\alpha_n}.$$

We are now able to define the weak derivative.

Definition 13 (Weak derivative)**.** *Let f be a given function in $L^1_{loc}(\Omega)$. Then f has a weak derivative $D^\alpha_w f$ if there exists a function $g \in L^1_{loc}(\Omega)$ such that*

$$\int_\Omega g(x)\phi(x) \; dr = (-1)^{|\alpha|} \int_\Omega f(x) D^\alpha \phi(x) \; dr \qquad \forall \; \phi \in C_0^\infty(\Omega)$$

If such a function g exists, we define the weak derivative by $D^\alpha_w f = g$.

The weak derivative can be seen as a generalization of the principle of the derivative of functions, not assumed to be differentiable. Following the given definition, those functions have to be only integrable. A generalization of weak

derivative can be found in distribution theory. But this is not part of this thesis. For more details about this topic, we refer to Schwartz [43].

With the former definitions and the notation of the weak derivation we are now able to generalize the Lebesque spaces and norms to Sobolev spaces and norms, which includes derivatives.

Definition 14 (Sobolev space and Sobolev norm)**.** *Let $k \in \mathbb{N}$ and let $f \in L^1_{loc}(\Omega)$. Assume that the weak derivatives $D^\alpha_w f$ exist for all $|\alpha| \leq k$. Then we define the Sobolev norm by*

$$||f||_{W^k_p(\Omega)} := (\sum_{|\alpha|\leq k} ||D^\alpha_w f||^p_{L^p(\Omega)})^{\frac{1}{p}},$$

for all $1 \leq p < \infty$. For $p = \infty$, we define

$$||f||_{W^k_\infty(\Omega)} := \max_{|\alpha|\leq k} ||D^\alpha_w f||_{L^\infty(\Omega)}.$$

We define in both cases the Sobolev space via

$$W^k_p(\Omega) := \{f \in L^1_{loc}(\Omega) \mid ||f||_{W^k_p(\Omega)} \ < \ \infty\}.$$

We can see, that $||.||_{W^k_p}$ is a norm and therefore, $W^k_p(\Omega)$ is a normed linear space. The next theorem shows us, that the Sobolev space $W^k_p(\Omega)$ is also complete.

Theorem 7. *The Sobolev space $W^k_p(\Omega)$ is complete and thus a Banach space.*

Proof. See: [8] page 30, (1.3.2) Theorem. □

Bibliography

[1] E. Adrian and B. Matthews *The Berger rhythm: Potential changes from the occipital lobes in man* Oxford Journals Brain 133(1), volume 133, 3-6, 2010

[2] S. Baillet, J. C. Mosher and R. M. Leahy *Electromagnetic brain mapping* IEEE Signal Processing Magazine 18(6), volume 18, 14 - 30, 2001

[3] S. B. Baumann, D. R. Wozny, S. K. Kelly and F. M. Meno *The Electrical Conductivity of Human Cerebrospinal Fluid at Body Temperature* IEEE Trans Biomed. ENG. 44(3), volume 44, 220-223, 1997

[4] H. Berger *Über das Elektroenkephalogramm des Menschen* Archif für Psychiatrie und Nervenkrankheiten, volume 87, 527-570, 1929

[5] D. Braess *Finite Elemente, Theorie, schnelle Löser und Anwendungen in der Elastizitätstheorie* Cambridge University Press, 2007

[6] M. A. B. Brazier *A study of the electric field at the surface of the head* Electroenc. Clin. Neurophysiol. 2, volume 2, 38-52, 1949

[7] S. Brandt and H. D. Dahmen *Elektrodynamik: Eine Einführung in Experiment und Theorie* Springer Lehrbuch, 2005

[8] S. C. Brenner and L. R Scott *The Mathematical Theory of Finite Element Methods* Springer Verlag, 2008

[9] H. C. Burger and J. B. van Millan *Heart Vector and Leads* Br Heart J. 8(3), volume 8, 157-161, 1947

[10] M. Burger *Numerik partieller Differentialgleichungen* Lecture Notes, University of Münster, 2006

[11] R. W. Clough *The finite element method in plane stress analysis* Proceedings, 2nd Conference on Electronic Computation, A.S.C.E. Structural Division. Pittsburgh, Pennsylvania, Sept, 1960

[12] C. Michel *128-Channel EEG Source Imaging in Epilepsy: Clinical Yield and Localization Precision* Journal of Clinical Neurophysiology 21(2), volume 21, 71-83, 2004

[13] M. Dannhauer, B. Lanfer, C.H. Wolters and T. Knösche *Modeling of the Human Skull in EEG Source Analysis* Human Brain Mapping 32(9), volume 32, 1383-1399, 2010

[14] J. de Munck, B. van Dijk and H. Spekreijse *Mathematical dipoles are adequate to describe realistic generators of human brain activity* IEEE Transactions on Biomedical Engineering, 35(11), volume 35, 960-966, 1988

[15] F. Drechsler, C. H. Wolters, T. Dierkes, H. Si and L. Grasedyck *A full subtraction approach for finite element method based source analysis using constrained Delaunay tetrahedralisation* Neuroimage 46(4), volume 46, 1055-1069, 2009

[16] M. Dobrowolski *Angewandte Funktionalanalysis Funktionalanalysis, Sobolev-Räume und elliptische Differentialgleichungen* Springer-Lehrbuch Masterclass, 2010

[17] O. Faugeras *The inverse EEG and MEG problems: The adjoint state approach I: The continuous case* Inria version 1, 1999, hal.inria.fr/docs/00/07/71/12/PDF/RR-3673.pdf

[18] O. Forster *Analysis 3. Integralrechnung im $\mathbb{R}^n$ mit Anwendungen* Vieweg-Verlag, 1996

[19] L. Haas *Hans Berger(1873-1941), Richard Caton(1842-1926) and electroencephalography* Journal Neurol Neurosurg Psychiatry 74(1), volume 74, 9, 2003

[20] W. Hackbusch *Elliptic Differential Equations. Theory and Numerical Treatment* Springer-Verlag, 1992

[21] H. Hallez *Review on solving the forward problem in EEG source analysis.* Journal of NeuroEngineering and Rehabilitation 4(46), volume 4, 1-59, 2007

[22] M. Hämäläinen *Magnetoencephalography theory, instrumentation, and applications to noninvasive studies of the working human brain* The American Physical Society 65, volume 65, 413-497, 1993

[23] J. Haueisen, D. S. Tuch, C. Ramon, P. H. Schimpf, V. J. Wedeen, J. S. George and J. W. Belliveau *The influence of brain tissue anisotropy on human EEG and MEG* Neuroimage 15(1), volume 15, 159-166, 2002

[24] H. Helmholtz *Ueber einige Gesetze der Vertheilung elektrischer Stroeme in koerperlichen Leitern mit Anwendung auf die thierisch - elektrischen Versuche* Ann Phys Chem 89, volume 89, 211-233,353-377, 1853

[25] S. Hildebrandt *Analysis 1* Springer-Lehrbuch, 2006

[26] P. Kauppinen, J. Hyttinen and J. Malmivuo *Sensitivity distribution visualizations of impedance tomography measurement strategies* Int. J. Bioelectromagnetism 8(1), volume 8, VII/1 - VII/9, 2006

[27] S. Lew *Accuracy and run-time comparison for different potential approaches and iterative solvers in finite element method based EEG source analysis* Appl Numer Math. 59(8), volume 59, 1970-1988, 2009

[28] R. McFee and F. D. Johnston *Electrocardiographic leads I. Introduction* American Heart Association, Inc. Circulation 8, volume 8, 554-568, 1953

[29] J. Malmivuo and R. Plonsey *Bioelectromagnetism - Principles and Applications of Bioelectric and Biomagnetic Fields* Oxford University Press, New York, 1995, http://www.bem.fi/book/index.htm

[30] J. C. Maxwell *Dynamical Theory of the Electromagnetic Field* Philosophical Transactions of the Royal Society of London 155, volume 155, 459-512, 1865

[31] M. Mohr *Simulation of Bioelectric Fields: The Forward and Inverse Problem of Electro-encephalographic Source Analysis* Dissertation Universität Erlangen-Nürnberg, Institut Informatik, 2004

[32] E. Niedermeyer and F. L. da Silva *Electroencephalography: Basic Principles, Clinical Applications, and Related Fields* Lippincott Williams and Wilkins, 4th Edition, 1999

[33] P. L. Nunez *Localization of brain activity with electroencephalography* In S. Sato Advances in Neurology, Magnetoencephalography 54, volume 54, 39-65, 1990

[34] Y. Okada *Neurogenesis of evoked magnetic fields* In S. N. Erne, H. D. Hahlbohm, and H. Lübbig, editors, Biomagnetism, 399-408, 1981

[35] C. Ramon, P. Schimpf, J. Haueisen, M. Holmes and A. Ishimaru *Role of Soft Bone, CSF and Gray Matter in EEG Simulations* Brain Topography 16(4), volume 16, 245-248, 2004

[36] F. Riesz *Sur une espece de geometrie analytique des systemes de fonctions sommables* C. R. Acad. Sci. Paris, volume 144, 1409-1411, 1907

[37] W. Ritz *Über eine neue Methode zur Lösung gewisser Variationsprobleme der mathematischen Physik* Journal für die reine und angewandte Mathematik 135, volume 135, 1-61, 1909

[38] S. Rush and D. Driscoll *EEG Electrode Sensitivity - An Application of Reciprocity* IEEE Transactions on Biomedical Engineering 16(1), volume 16, 15-22, 1969

[39] M. Rullmann, A. Anwander, M. Dannhauer, S. Warfield, F.H. Duffy and C.H. Wolters *EEG source analysis of epileptiform activity using a 1mm anisotropic hexahedral finite element head model* NeuroImage 44(2), volume 44, 399-410, 2009

[40] K. Saladin *Anatomy and Physiology: The Unity of Form and Function* McGraw-Hill Science/Engineering/Math, 4th Edition, 2007

[41] J. Sarvas *Basic mathematical and electromagnetic concepts of the biomagnetic inverse problem* Phys. Med. Biol 32(1), volume 32, 11-22, 1987

[42] K. Schellbach *Probleme der Variationsrechnung* Journal für die reine und angewandte Mathematik 41(4), volume 4, 293-363, 1852

[43] L. Schwartz *Theorie des distributions* Hermann, 1951

[44] Wiki *Wiki System of the SimBio software package* https://www.mrt.uni-jena.de/simbio/index.php/Main_page

[45] B. Vanrumste *EEG dipole source analysis in a realistic head model* PhD thesis, Faculteit Toegepaste Wetenschappen, Universiteit Gent, 2001, http://homes.esat.kuleuven.be/ bvanrums/doct.pdf

[46] S. Vallaghe, T. Papadopoulo and M. Clerc *The adjoint method for general EEG and MEG sensor-based lead field equations* Physics in medicine and biology, Phys.Med.Biol. 54, volume 54, 135-147, 2009

[47] S. Vallaghe *EEG and MEG forward modeling : computation and calibration* PhD thesis, University of Nice - Sophia Antipolis, 2008

[48] J. Vorwerk *Comparison of Numerical Approaches to the EEG Forward Problem* Diploma Thesis, University of Münster, 2011

[49] D. Weinstein, L. Zhukov and C. Johnson *Lead-field Bases for Electroencephalography Source Imaging* Annals of Biomedical Engineering 28(9), volume 28, 1059-1065, 2000

[50] D.Werner *Funktionalanalysis* Springer-Lehrbuch, 2007

[51] C. H. Wolters, L. Grasedyck and W. Hackbusch *Efficient computation of lead field bases and influence matrix for the FEM-based EEG and MEG inverse problem* Inverse Problems 20(4), volume 20, 1099-1116, 2004

[52] C. H. Wolters *Influence of Tissue Conductivity Inhomogeneity and Anisotropy on EEG/MEG based Source Localization in the Human Brain*

MPI Series in Cognitive Neuroscienece, No. 39, Leipzig: MPI of Cognitive Neuroscience, also: Dissertation, University of Leipzig, http://nbn-resolving.de/urn:nbn:de:bsz:15-qucosa-37549, 2003

[53] C. H. Wolters, A. Anwander, G. Berti and U. Hartmann *Geometry-adapted hexahedral meshes improve accuracy of finite element method based EEG source analysis* IEEE Trans.Biomed.Eng 54(8), volume 54, 1446-1453, 2007

[54] C. H. Wolters, H. Köstler, C. Möller, J. Härdtlein, and A. Anwander *Numerical approaches for dipole modeling in finite element method based source analysis* International Congress Series 1300, volume 1300, 189â192, 2007

[55] C. H. Wolters, H. Köstler, C. Möller, J. Härtlein, L. Grasedyck and W. Hackbusch *Numerical mathematics of the subtraction method for the modeling of a current dipole in EEG source reconstruction using finite element head models* SIAM J. on Scientific Computing 30(1), volume 30, 24-45, 2007

Erklärung der Eigenständigkeit

Hiermit versichere ich, Sven Wagner, dass ich die vorliegende Arbeit selbstständig verfasst und keine anderen als die angegebenen Hilfsmittel verwendet habe.
Gedanklich, inhaltlich oder wörtlich Übernommenes habe ich durch Angabe von Herkunft und Text oder Anmerkung belegt bzw. kenntlich gemacht. Dies gilt in gleicher Weise für Bilder, Tabellen und Skizzen, die nicht von mir selbst erstellt wurden.
Diese Arbeit wurde in gleicher oder ähnlicher Form noch keiner Prüfungsbehörde vorgelegt.

Münster, den 6. Oktober, 2011